

TABLE OF CONTENTS

	Page
1 The Standard Model of Particle Physics	1
1.1 Particles and Forces	2
1.2 The Electroweak Theory	6
1.3 The Higgs Mechanism and Electroweak Symmetry Breaking	9
1.4 The Complete Standard Model, Successes and Shortcomings	13
2 Experimental Setup	14
2.1 The Large Hadron Collider	15
2.1.1 Machine Design and Layout	16
2.1.2 Injection Chain and Bunch Structure	19
2.1.3 The Concept of Luminosity	22
2.1.4 Operation of the Large Hadron Collider	23
2.2 The ATLAS Detector	25
2.2.1 The ATLAS Coordinate System	25
2.2.2 The Inner Detector	27
2.2.3 Calorimeter Systems	31
2.2.4 The Muon Spectrometer	35
2.2.5 Trigger and Data Acquisition	40
3 Physics Building Blocks and their Reconstruction	43
3.1 Charged-Particle Tracks and Primary Vertices	44
3.2 Electrons and Muons	46
3.2.1 Electrons	46
3.2.2 Muons	51
3.3 Jets	54
3.3.1 Jet Reconstruction	55
3.3.2 Jet Calibration	58
3.3.3 Flavor Tagging of Jets	63
3.4 The Missing Transverse Momentum	69
Bibliography	71

Chapter 1

The Standard Model of Particle Physics

If you wish to make an apple pie from scratch, you must first invent the universe.

—Carl Sagan, *Cosmos: A Personal Voyage*

As it stands, what has become known as the ‘Standard Model (SM) of Particle Physics’ is nothing less than one of the greatest achievements of mankind, due to both the magnitude by which it has changed our perception of the underlying nature of the universe and to the clever methods and tinkering by which this nature was unveiled by many clever physicists whose history has become veritable lore. In terms of imagination and insight, it is second only to the special and general theories of relativity – though the fields are nevertheless intricately intertwined.

Not considering the scientific progress made in the 18th and 19th centuries, and ignoring the ancient Greeks despite their fabled invention of atomic theory, the physical insights and major work that led to the current picture of elementary particle physics described by the SM began with the *annus mirabilis* papers of Albert Einstein in the year 1905 [1, 2, 3]. In these papers, Einstein was able to shed light on the quantization of electromagnetic radiation (building off of the seminal work of Max Planck [4]) and introduce the special theory of relativity. These works laid the conceptual and philosophical groundwork for the major breakthroughs in fundamental physics of 20th century physics: from the ‘old quantum theory’ of Bohr and Sommerfeld in the early 1900’s to the equivalent wavefunction and matrix-mechanics formulations of Schrödinger and Heisenberg that coalesced into ‘modern’ quantum mechanics in the mid-1920’s. The modern approach, non-relativistic at its heart, provided a sufficient mathematical and interpretable framework in which to work and match predictions to observed phenomena, old and new. It has for the most part remained unchanged and is the quantum mechanics that is taught to students at both the undergraduate and graduate level to this very day. It is the theory that has since revolutionised all aspects of the physical sciences and technologies that dictate our everyday-lives. In the mid-1920’s, however, despite large efforts put forth by the forbears of modern quantum mechanics, the quantum-mechanical world had yet to be made consistent with Einstein’s theory of relativity — a requirement that must be

met for all consistent physical theories of nature. It was the insight of Paul Dirac who was finally able to successfully marry the theory of the quantum with that of relativity when he introduced his relativistic quantum-mechanical treatment of the electron in 1927 and 1928 [5, 6].¹ This work provided the starting point for a decades-long search of a consistent quantum-mechanical and relativistic treatment of electrodynamics, known as *quantum electrodynamics* (QED). The search for QED ended at the end of the 1940’s with the groundbreaking work of Dyson, Feynman, Schwinger, and Tomanaga [9, 10, 11, 12, 13, 14, 15, 16] that introduced the covariant and gauge invariant formulation of QED — the first such relativistic quantum field theory (QFT). QED allowed the physicists to make predictions that agreed with observation at unprecedented levels of accuracy and has since led to the adoption of its language and mathematical toolkit as the foundational framework in which to construct models that accurately describe nature.² The SM is no less than an ultimate conclusion of these works: a consistent set of relativistic quantum field theories, using the language developed by Feynman et al., that describes essentially all aspects of the known particles and forces that make up the observed universe.

1.1 Particles and Forces

There are four known fundamental forces at work in the universe: electromagnetism, the weak interaction, the strong interaction, and gravity. Our understanding of the existence of each of these forces has essentially been arrived at empirically, with physicists following experimental clues, and their basic behaviors deduced after long trials of effort. The SM encompasses all of these forces except for gravity, which currently is only described by the classical (i.e. not quantum) theory of geometrodynamics, or general relativity. The gravitational interaction is incredibly weak in comparison to the others, however, and is not relevant to the types of particle interactions that we are currently sensitive to in particle physics experiments. Electromagnetism is by far the most familiar, as it is the force most commonly experienced and is what is at work in our everyday life (reaction forces between objects on tables and chairs, friction, wall-plugs, batteries, DNA structure, etc...) and is typically what students are first presented with in their physics studies. The weak force is responsible for things like radioactive decay, which makes possible the process of nuclear β -decay and the nuclear fission process that fuels the sun, for example. The strong force is what binds protons and neutrons together, and thus is responsible for holding together most of the (ordinary) matter in the universe.³

The forces mediate the interactions between the matter particles, which we use to deduce their presence. The SM predicts fundamental, point-like particles that appear in two general classes depending on whether they have integral spin ($S \in [0, 1, 2, \dots]$) or half-integral spin ($S \in [1/2, 3/2, \dots]$); the former are referred to as *bosons* and the latter as *fermions*. In the SM, the

¹ A complete history of the people and ideas involved in the development of the modern theory of Quantum Mechanics can be found in references [7, 8], and the references therein.

² For a complete discussion of the developments leading up to QED, see the fabulous book by S. Schweber [17].

³ ‘Ordinary’ to distinguish from dark matter, for example.

particles that are responsible for making up matter are all spin-1/2 fermions and are either *leptons* or *quarks*; within each class there are three generations (or families) that are essentially copies of the first. The forces in the SM are interpreted as being mediated by spin-1 bosons, referred to as the *gauge bosons*. The leptons and quarks all experience the weak force, but only the quarks experience the strong interaction. All electrically charged particles interact with the electromagnetic interaction.

The particles of the SM are described as quantum fields whose dynamics are described by the SM Lagrangian from which the equations of motions can be derived. The particles, and by extension the SM Lagrangian that describes them, are found to be invariant under transformations of spacetime (space translations, rotations, Lorentz boosts) and three internal transformations described by unitary transformations: $\mathcal{P} \times \mathcal{SU}(3)_C \times \mathcal{SU}(2)_L \times \mathcal{U}(1)_Y$. This is illustrated in Figure 1.1. The strong force is described by a local $\mathcal{SU}(3)$ symmetry that acts only on the particles that have *color charge*. The term “color” arises from the fact that the color charge is found to exist in three varieties which have been labelled as red (r), blue (b), or green (g), and due to the fact that “colorless” states are formed when all three are combined (r+g+b), just like with visible light that humans are familiar with, or when states are formed of color-anti-color pairs (r+r̄). For this reason, the QFT describing the strong force is called Quantum *Chromodynamics* (QCD), and is mediated by eight *gluons* (G). The particles subject to the weak force are invariant under weak-isospin $\mathcal{SU}(2)$ transformations, mediated by the three W bosons (W_1, W_2, W_3). The $\mathcal{U}(1)$ transformations, mediated by the B boson, preserve weak-hypercharge, Y . The $\mathcal{SU}(2)$ symmetry is respected only by the left-handed chiral particles (leptons or quarks), with the right-handed chiral particles not participating. There is additionally a single scalar (i.e. spin-0) field, the Higgs field, that is an $\mathcal{SU}(2)$ doublet, about which more will be described shortly. The particle content thus described is presented in detail in Table 1.1. The $\mathcal{SU}(2)$ left-handed chiral fields appear as doublets and are grouped in and “up-down” pair (e.g. (u_L, d_L) or $(e_L, \nu_{e,L})$) whereas the right-handed chiral fields, living in the singlet representation of $\mathcal{SU}(2)$, do not (e.g. u_R). Note that the SM does not allow for right-handed neutrinos (a term like ν_R does not appear).

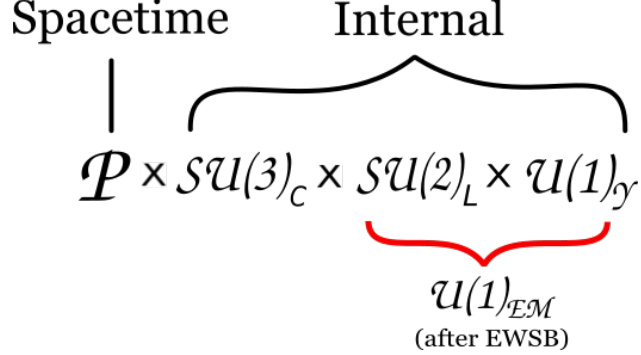


Figure 1.1: The spacetime and internal gauge structure of the SM. \mathcal{P} refers to the Poincaré symmetry group. $SU(3)_c$ refers to the $SU(3)$ symmetry of the color sector of QCD and $SU(2)_L \times U(1)_Y$ refers to the left-handed chiral symmetry of the electroweak interaction. After spontaneous symmetry breaking due to the Higgs mechanism, the $SU(2)_L \times U(1)_Y$ symmetry reduces to the $U(1)_{EM}$ symmetry of electromagnetism.

The SM Lagrangian is shown in Eqn. 1.1 and describes the complete content of the SM: encompassing all interactions between the known particles and the symmetries that they obey.

$$\mathcal{L}_{SM} = -\frac{1}{4} \sum_{\text{gauge}} F_{\mu\nu}^i F^{i\mu\nu} - \sum_f \bar{f} \gamma^\mu D_\mu f + (D_\mu \phi)^\dagger (D^\mu \phi) - \mu^2 \phi^\dagger \phi - \lambda (\phi^\dagger \phi)^2 \quad (1.1)$$

The first term of Eqn. 1.1 is a sum over the three internal gauge groups, and $F_{\mu\nu}^a = \partial_\mu A_\nu^a - \partial_\nu A_\mu^a + g f^{abc} A_\mu^b A_\nu^c$, where A_μ is one of the three gauge fields, g is the associated gauge coupling parameter, and a sum over i is implied. The f^{abc} are the so-called *structure constants* of the gauge group. For Abelian groups like $U(1)$, $f^{abc} = 0$. For non-Abelian gauge groups like $SU(2)$ and $SU(3)$, $f^{abc} \neq 0$. For example, for $SU(2)$ the structure constants are nothing more than the Levi-Civita totally anti-symmetric tensor, ε_{ijk} , giving for the weak gauge force:

$$\mathbf{W}_{\mu\nu} = \partial_\mu \mathbf{W}_\nu - \partial_\nu \mathbf{W}_\mu - g_2 \mathbf{W}_\mu \times \mathbf{W}_\nu \quad (1.2)$$

where \mathbf{W}_μ is the vector of the three weak gauge fields (W_1 , W_2 , and W_3) and g_2 is their associated gauge coupling. The non-zero f^{abc} of non-Abelian gauge groups means that the gauge bosons of the weak and strong interactions can interact with themselves due to terms appearing in Eqn. 1.1 that contain only the gauge bosons. **add Feynman diagram? – showing what the squared term of $W_{\mu\nu}$ representing triple and quartic couplings**

The second term of Eqn. 1.1 describes the lepton and quark kinetic energies and their interactions with the gauge fields. The f refer to the fermion fields (quarks and leptons) and the corresponding sum is over all species of fermion. D_μ is the gauge covariant derivative, and for the SM is given by:

$$D_\mu = \partial_\mu - ig_1 \frac{Y}{2} \mathcal{B}_\mu - ig_2 \frac{\tau^i}{2} \mathcal{W}_\mu^i - ig_3 \frac{\lambda^a}{2} G_\mu^a \quad (1.3)$$

where g_1 , g_2 , and g_3 are the gauge coupling constants for $\mathcal{U}(1)_Y$, $\mathcal{SU}(2)_L$, and $\mathcal{SU}(3)_C$, respectively, that give the overall strength of the associated coupling. Summation over repeated indices is implied and the τ^i (λ^a) are the three (eight) generators of the $\mathcal{SU}(2)$ ($\mathcal{SU}(3)$) gauge group, with $i \in [1, 2, 3]$ ($a \in [1, \dots, 8]$), and are typically represented by the Pauli (Gell-Mann) matrices. Note that the form of Eqn. 1.3 is strictly mandated by the requirement that the theory be *gauge invariant*, i.e. that transformations of the fields under the internal symmetries of Fig. 1.1 leave the action of \mathcal{L}_{SM} unchanged. This is described in detail in [Appendix XXX](#).

The last three terms in Eqn. 1.1 are all terms including the Higgs field, ϕ , and will be discussed in detail in Section 1.3.

Inspection of Eqn. 1.1 will reveal two things. The first thing that one may notice is that it does not appear to describe electromagnetism as it does not have a term representing the photon, the familiar mediator of the electromagnetic interaction. The second, and perhaps more immediately obvious, thing is that no mass terms appear in \mathcal{L}_{SM} : all fields appear to have zero mass! Both of these facts are counter to our everyday experience: we know electromagnetism is real and that matter, at the very least, is massive. In the next few sections we will see how these apparent issues are resolved.

Table 1.1: **Fix quantum numbers** The particle content of the SM and their transformation properties under the SM gauge groups, prior to electroweak symmetry breaking. The representations of each of the gauge groups are shown in the three-right columns. The $\mathcal{U}(1)$ symmetry of weak-hypercharge transformations is one-dimensional and the column gives the weak-hypercharge \mathcal{Y} associated with each field. For $\mathcal{SU}(3)$ and $\mathcal{SU}(2)$, **1** refers to the field belonging to the associated singlet representation, **2** to the doublet representation, **3** to the triplet representation, and **8** to the octet representation.

	Field Label	Content	Spin	$\mathcal{U}(1)$ ($= \mathcal{Y}$)	$\mathcal{SU}(2)$	$\mathcal{SU}(3)$
Leptons Quarks	Q_i	$(u_L, d_L), (c_L, s_L), (t_L, b_L)$	1/2	1/6	2	3
	$u_{R,i}$	u_R	1/2	2/3	1	3
	$d_{R,i}$	d_R	1/2	-1/3	1	3
	L_i	$(e_L, \nu_{e,L}), (\mu_L, \nu_{\mu,L}), (\tau_L, \nu_{\tau,L})$	1/2	1/2	2	1
	$e_{R,i}$	e_R, μ_R, τ_R	1/2	-1	1	1
Gauge Fields	B	B	1	0	1	1
	W	(W_1, W_2, W_3)	1	0	3	1
	G	$G_a, a \in [1, \dots, 8]$	1	0	1	8
Higgs Field	ϕ	(ϕ^+, ϕ^0)	0	1/2	2	1

1.2 The Electroweak Theory

It was the work of Glashow, Weinberg, and Salam (GWS) that ultimately put forth a consistent picture of the chiral weak force and its unification with electromagnetism [18, 19, 20]. As a result, the theory of particles and fields that respect the $SU(2)_L \times U(1)_Y$ gauge invariance of the SM is sometimes referred to as ‘GWS theory’, but is more typically known as the electroweak theory. Since all matter particles are subject to the electroweak interaction, but only a subset of the particles that have color charge (the quarks) are subject to the strong interaction described by QCD, the study of the SM can essentially be partitioned into two parts: the part that deals with the dynamics and interactions of colored objects (the ‘QCD part’, \mathcal{L}_{QCD}) and the part that deals with electroweak interactions, including the Higgs (the ‘Electroweak part’, $\mathcal{L}_{\text{Electroweak}}$). Given the broad reach of the electroweak interaction, in the early days GWS theory was considered the heart of the SM and why GWS were awarded the Nobel prize in 1979.⁴ In this section we will focus on the $SU(2)_L \times U(1)_Y$ portion of \mathcal{L}_{SM} .

The first thing to remember is that the electroweak theory is *chiral*, i.e., it distinguishes between left- and right-chiral fermion fields. For conceptual clarity, it can be useful to take the massless (relativistic) limit of fermions to get an idea of what chirality represents. For a massless fermion field, the chirality is equivalent to the perhaps more-familiar *helicity*, defined as the projection of its spin onto its momentum (direction of motion). The helicity of left-handed (right-handed) massless fermions is positive (negative), meaning that their spin is parallel (anti-parallel) to its momentum. Fermion fields, then, are commonly defined inclusive of their handedness, with the left- and right-handed components projected out using the P_L and P_R projection operators,

$$f_L = P_L f = \frac{1}{2}(1 - \gamma_5)f \quad \text{and} \quad f_R = P_R f = \frac{1}{2}(1 + \gamma_5)f. \quad (1.4)$$

Focusing only on the first generation of the leptons (the discussion holds equally well for the second and third generations, as well as for the quarks), we can gather the $U(1)$ terms of Eqn. 1.1,

$$\begin{aligned} -\mathcal{L}_{\text{ferm}}(U(1), \text{leptons}) &= \bar{L}i\gamma^\mu(i g_1 \frac{Y_L}{2} B_\mu)L + \bar{e}_R i\gamma^\mu(i g_1 \frac{Y_R}{2} B_\mu)e_R \\ &= \frac{g_1}{2}[Y_L(\bar{\nu}_L \gamma^\mu \nu_L + \bar{e}_L \gamma^\mu e_L) + Y_R \bar{e}_R \gamma^\mu e_R]B_\mu, \end{aligned} \quad (1.5)$$

where $L = (\nu_L, e_L)$ is used in going from the first to second line. Likewise, gathering the associated $SU(2)$ terms and noting that $\tau^i W^i$ is a 2×2 matrix since the τ^i are $SU(2)$ generators (e.g. the Pauli matrices) gives,

$$\begin{aligned} -\mathcal{L}_{\text{ferm}}(SU(2), \text{leptons}) &= \bar{L}i\gamma^\mu[i g_2 \frac{\tau^i}{2} W_\mu^i]L \\ &= -\frac{g_2}{2}\left[\bar{\nu}_L \gamma^\mu \nu_L W_\mu^0 - \sqrt{2}\bar{\nu}_L \gamma^\mu e_L W_\mu^+ - \sqrt{2}\bar{e}_L \gamma^\mu \nu_L W_\mu^- - \bar{e}_L \gamma^\mu e_L W_\mu^0\right], \end{aligned} \quad (1.6)$$

⁴Actually, the acceptance of the GWS theory as the de-facto SM of the time was not widely held until some years after its publication, when t’Hooft proved that it was renormalizable [21, 22]. Such a complete understanding in the QCD sector would not come until almost a decade later, in the late 1970’s Wojciec etc CITE.

where we have used the following re-definitions of the $SU(2)$ gauge fields,

$$W_\mu^+ = \frac{1}{\sqrt{2}} (-W_\mu^1 + iW_\mu^2) \quad W_\mu^- = \frac{1}{\sqrt{2}} (-W_\mu^1 - iW_\mu^2) \quad W_\mu^0 = W_\mu^3. \quad (1.7)$$

In principle, Equations 1.5 and 1.6 describe completely all electroweak interactions between matter and the gauge fields of $SU(2)_L \times U(1)_Y$. We would like to make the correspondence between these equations and what we know to empirically exist: the electromagnetic interaction and the presence of a massive, charged mediator of the weak nuclear force responsible for nuclear β -decay, for example. From the theory of QED, it is a-priori known what the form of the interaction of the neutral photon and the electron should look like. Inspecting all charge-preserving (i.e. neutral) terms of Eqn. 1.5 and 1.6, it can be seen that the B_μ and W_μ^0 fields have this expected fermion coupling, suggesting a re-definition as follows,

$$\begin{pmatrix} A_\mu \\ Z_\mu \end{pmatrix} = \begin{pmatrix} \cos \theta_W & \sin \theta_W \\ -\sin \theta_W & \cos \theta_W \end{pmatrix} \begin{pmatrix} B_\mu \\ W_\mu^0 \end{pmatrix}, \quad (1.8)$$

where we have used $Y_L = -1$ and define the relations between the $SU(2)$ and $U(1)$ couplings as,

$$\sin \theta_W = \frac{g_1}{\sqrt{g_1^2 + g_2^2}} \quad \cos \theta_W = \frac{g_2}{\sqrt{g_1^2 + g_2^2}} \quad e = \frac{g_1 g_2}{\sqrt{g_1^2 + g_2^2}}. \quad (1.9)$$

The angle θ_W is known as the *Weinberg angle*. It quantifies the amount of *gauge mixing* that occurs between the neutral $SU(2)_L \times U(1)_Y$ gauge fields, B_μ and W_μ^0 .

The above algebra allows to re-write the electroweak Lagrangian, now describing interactions between the fermions and the newly defined A_μ , Z , and W^\pm , as,

$$\begin{aligned} \mathcal{L}_{\text{ferm, first-gen.}} = & \underbrace{\sum_{f \in \nu_e, e, u, d} e Q_f (\bar{f} \gamma^\mu f) A_\mu}_{\text{Neutral, } \sim \text{EM}} \\ & + \underbrace{\frac{g_2}{\cos \theta_W} \sum_{f \in \nu_e, e, u, d} [\bar{f}_L \gamma^\mu f_L (T_f^3 - Q_f \sin^2 \theta_W) + \bar{f}_R \gamma^\mu f_R (-Q_f \sin^2 \theta_W)] Z_\mu}_{\text{Neutral weak interaction}} \\ & + \underbrace{\frac{g_2}{\sqrt{2}} [(\bar{u}_L \gamma^\mu d_L + \bar{\nu}_{e,L} \gamma^\mu e_L) W_\mu^+ + h.c.]}_{\text{Charged weak interaction}} \end{aligned} \quad (1.10)$$

The first term of Eqn. 1.10 has the expected form expected from QED, describing the interaction between a neutral gauge boson and fermions and allows us to interpret the parameter e , introduced in Eqn. 1.9, as the coupling of electromagnetism (electric charge) with Q_f as the fermion's electric charge quantum number (in units of e). The A_μ arrived at via the gauge mixing of Eqn. 1.8 then must correspond to the photon of electromagnetism. The second term of Eqn. 1.10 predicts the existence of an additional neutral gauge boson, the Z boson, with its couplings to the left- and right-handed fermions dictated by the $SU(2)_L \times U(1)_Y$ gauge mixing. The quantity T_f^3 is the

fermion field's quantum number associated with the third component of weak-isospin ($\mathcal{SU}(2)$). The third term of Eqn. 1.10 involves charged weak-interactions involving the W^\pm_μ gauge bosons that transform the up- and down-type fields of the left-handed $\mathcal{SU}(2)$ doublet fields into each other.

The terms involving W^\pm_μ in Eqn. 1.10 are of the form $\bar{\nu}_L \gamma^\mu e_L$ which, using the chiral projection operators (Eqn. 1.4), can be written as follows,

$$\bar{\nu}_L \gamma^\mu e_L = \frac{1}{2} \bar{\nu} \gamma^\mu (1 - \gamma_5) e, \quad (1.11)$$

showing that the charged weak interactions involving W^\pm_μ are the coherent sum of vector (γ^μ) and axial-vector ($\gamma^\mu \gamma_5$) bilinear covariants; this is the famous $V-A$ charged-current interaction of Fermi's nuclear β -decay. It is this $V-A$ form that results in the charged interactions of the weak force not being invariant under chiral transformations ($f_R \leftrightarrow f_L$): they involve only the left-chiral fermion fields. For this reason, *parity* is said to be maximally violated by the weak interaction.⁵ This result, as presented in the above, is due to our having injected it into our assumption on the field content in the first place out of hindsight. There is no first-principles reason why the weak interactions should be this way, however, and historically it was arrived at empirically.

What we have principally shown in this section is that, in order for the $\mathcal{SU}(2)_L \times \mathcal{U}(1)_Y$ content of the SM Lagrangian to correspond to what is found experimentally, it is expected that the gauge fields of the underlying symmetries mix. Specifically, the neutral $\mathcal{SU}(2)$ gauge field (W^0_μ) mixes with that of the $\mathcal{U}(1)$ gauge symmetry (B_μ) by an amount dictated by the Weinberg angle, θ_W , resulting in descriptions of interactions consistent with the experimentally observed photon and a prediction of a neutral Z -boson. The fermion electric charge is seen to be dependent on this mixing and can be related to the underlying $\mathcal{SU}(2)$ and $\mathcal{U}(1)$ gauge symmetries by the Gell-Mann-Nishijima relation,

$$Q_f = T_f^3 + \frac{1}{2} Y, \quad (1.12)$$

This relation summarises well the result of the $\mathcal{SU}(2)_L \times \mathcal{U}(1)_Y$ gauge mixing and allows one to infer that the electromagnetism of common experience is related to the weak interaction and is in fact just one aspect of a unified electroweak interaction. Later on, we will see that (gauge) unification such as this plays a large role in our current understanding of the universe.

We have thus shown that the SM predicts the existence of the familiar electromagnetic force and potentially provides an additional mediator (the W^\pm_μ) for the charged weak interaction that, prior to the formulation of GWS, was lacking a consistent physical description. However, it is still not evident how the SM can support the experimental fact that fermions have mass and that the predicted mediator of the charged weak-nuclear force (the W^\pm_μ) *must* be massive given the very short range of the interaction. In order for such mass terms to be allowed in \mathcal{L}_{SM} , we need the Higgs mechanism.

⁵A parity transformation refers to inverting a field's space coordinates as $\vec{x} \rightarrow -\vec{x}$.

1.3 The Higgs Mechanism and Electroweak Symmetry Breaking

The missing mass-terms for the fields in \mathcal{L}_{SM} are provided by the Brout-Englert-Higgs (BEH) mechanism [23, 24, 25]. Before describing the specifics of the BEH mechanism, we should first describe the problem of why \mathcal{L}_{SM} doesn't support general mass terms for any of the fields in the first place. That is, for example, why can't a fermion term like $m\bar{f}f$ exist in \mathcal{L}_{SM} ?

Adding mass terms to \mathcal{L}_{SM} for the fermions explicitly breaks the underlying $SU(2)$ gauge symmetry. This can be understood if we recognize the experimentally supported fact that the left-handed fermions appear as $SU(2)$ doublets and that the right-handed fermions as singlets,

$$\begin{aligned} m\bar{f}f &= m\bar{f}(P_L + P_R)f \\ &= m\bar{f}P_L P_L f + m\bar{f}P_R P_R f \\ &= m(\bar{f}_R f_L + \bar{f}_L f_R), \end{aligned} \tag{1.13}$$

where we have used identity relations of the projection operators P_L and P_R and the fact that $\bar{f}P_L = \bar{f}_R$ (and vice-versa). The last line of Eqn. 1.13 involve terms mixing $SU(2)$ doublets with $SU(2)$ singlets. Such a term is therefore not allowed if we wish to keep the $SU(2)$ gauge symmetry intact.

Mass terms for the gauge bosons, of the form $mB_\mu B^\mu$, also do not work. For the Abelian $U(1)$ symmetry, for example, gauge invariance implies invariance of \mathcal{L}_{SM} under transformations of the form $B'_\mu \rightarrow B_\mu - \partial_\mu \chi/g$. Such a mass term for the gauge bosons is clearly not invariant under such a transformation. Even forgoing this fact, adding such a term would quickly lead to non-renormalisable divergences appearing in the theory, due to the longitudinal field components that appear in massive field propagators, rendering \mathcal{L}_{SM} meaningless.

The BEH mechanism provides a way out of this problem. It refers to the introduction of a spin-0 field, the Higgs field (Table 1.1), to the SM along with its corresponding interaction terms to \mathcal{L}_{SM} : the last three terms of Eqn. 1.1. The final two terms make up what is referred to as the Higgs potential and can be expressed as,

$$V(\phi) = -\mu^2\phi^2 - \lambda\phi^4 \tag{1.14}$$

The Higgs field is an $SU(2)$ doublet and it can be seen that the interactions described by Eqn. 1.14 respect $SU(2)$ gauge symmetry. If $\mu^2 > 0$, nothing all too interesting occurs and Eqn. 1.14 describes a self-interacting, complex scalar field. If we take $\mu^2 < 0$, however, then the classical potential described by Eqn. 1.14 has non-zero minima located at $\phi = \pm v$ with $v = \sqrt{-\mu^2/\lambda}$. This is illustrated in Fig. 1.2. We see that the stable equilibrium point ϕ_0 of the Higgs potential, the *Higgs vacuum expectation value* (vev), is not at $\phi = 0$ but at v ,

$$\phi_0 = \frac{1}{\sqrt{2}} \begin{pmatrix} 0 \\ v \end{pmatrix} \tag{1.15}$$

The choice of Eqn. 1.15 to represent the Higgs vacuum is motivated by the requirement that the vacuum not be electrically charged — a fact motivated very much by experiment and everyday experience — so the up-type $SU(2)$ component of the Higgs field, ϕ^+ (Table 1.1), is chosen to be zero for ϕ_0 . The choice of an electrically neutral vacuum sets the rest of the $SU(2)_L \times U(1)_Y$ structure of the complex Higgs field since, by the Gell-Mann-Nishijima relation (Eqn. 1.12) and charge conservation, a neutral $SU(2)_L \times U(1)_Y$ field should have down-type $SU(2)$ quantum numbers and $U(1)$ hypercharge $Y = 1$,

$$Q = T_3 + \frac{1}{2}Y \rightarrow Q_{\phi_0} = -\frac{1}{2} + \frac{1}{2} \times 1 = 0. \quad (1.16)$$

Note that Eqn. 1.15 states that only one component of the Higgs $SU(2)$ doublet attains a non-zero vev. This clearly means that the $SU(2)$ gauge symmetry is not respected by the choice of $\mu^2 < 0$ and that the electroweak $SU(2)_L \times U(1)_Y$ symmetry is *spontaneously broken*.⁶ The Higgs field acquiring a non-zero vev is then referred to as the *electroweak symmetry breaking* (EWSB) of the SM.

To further examine the physical consequences of EWSB, we perturb the Higgs field about its minimum value,

$$\phi(x) \propto \begin{pmatrix} 0 \\ \frac{1}{2}(v + h(x)) \end{pmatrix}, \quad (1.17)$$

where $h(x)$ correspond to excitations of the Higgs field that represent the physically observable Higgs boson. Inserting Eqn. 1.17 into the $D_\mu \phi$ terms of Eqn. 1.1, one eventually works through the algebra and obtains,

$$|D_\mu \phi(x)|^2 = \frac{1}{8}v^2 g_2^2 \left[(W_\mu^1)^2 + (W_\mu^2)^2 \right] + \frac{1}{8}v^2 (g_1 B_\mu - g_2 W_\mu^3)^2. \quad (1.18)$$

Using the field re-definitions for the W_μ , A_μ and Z_μ introduced in Section 1.2, we see that this can be re-written as (modulo factors of 2),

$$|D_\mu \phi(x)|^2 \propto \left(\frac{1}{2}vg_2 \right)^2 W_\mu^+ W^{-\mu} + \left(\frac{1}{2}v\sqrt{g_1^2 + g_2^2} \right)^2 Z_\mu Z^\mu + (0)^2 A_\mu A^\mu, \quad (1.19)$$

which provide, clearly, mass terms for the electroweak gauge bosons:

$$M_W = \frac{1}{2}vg_2, \quad M_Z = \frac{1}{2}v\sqrt{g_1^2 + g_2^2}, \quad M_A = 0. \quad (1.20)$$

The expression for the masses acquired by the W^\pm and Z gauge bosons in Eqn. 1.20 is expected by Goldstone's theorem [26] which states that for every broken continuous symmetry one expects

⁶A symmetry of a Lagrangian is said to be ‘spontaneously’ broken if the Lagrangian of the underlying theory respects the symmetry but it gets broken through dynamical means or if the lowest-energy state (vacuum) does not respect the symmetry.

an associated massless scalar field (a ‘Goldstone boson’) to appear in the theory. The fact that the W^\pm and Z acquire mass after EWSB is then interpreted as these fields having acquired longitudinal field components by ‘eating’ the Goldstone boson degrees of freedom associated with the breaking of $SU(2)_L$. The BEH mechanism refers specifically to this means of the gauge bosons acquiring mass via ‘eating’ the Goldstone bosons.

The fact that the Higgs vev respects charge conservation (Eqn. 1.16) means that \mathcal{L}_{SM} , after EWSB, still respects a local $\mathcal{U}(1)$ gauge symmetry; although now this is the $\mathcal{U}(1)$ gauge symmetry associated with electromagnetism, $\mathcal{U}(1)_{EM}$, as opposed to that of weak-hypercharge, $\mathcal{U}(1)_Y$. This indicated in Fig. 1.1.

There are also additional terms involving the now-massive W^\pm and Z bosons and $h(x)$ in the expansion of $|D_\mu \phi(x)|^2$ of Eqn. 1.18 (not shown) that describe the gauge bosons’ interactions with the observable Higgs boson, involving terms of the form hVV and $hhVV$ ($V \in (W, Z)$) whose coupling strengths depend on the gauge boson masses (Eqn. 1.20) [feynman diagrams?](#):

$$\mathcal{L}_{h-VV} \propto \frac{M_V^2}{v} \quad \mathcal{L}_{hh-VV} \propto \frac{M_V^2}{v^2}. \quad (1.21)$$

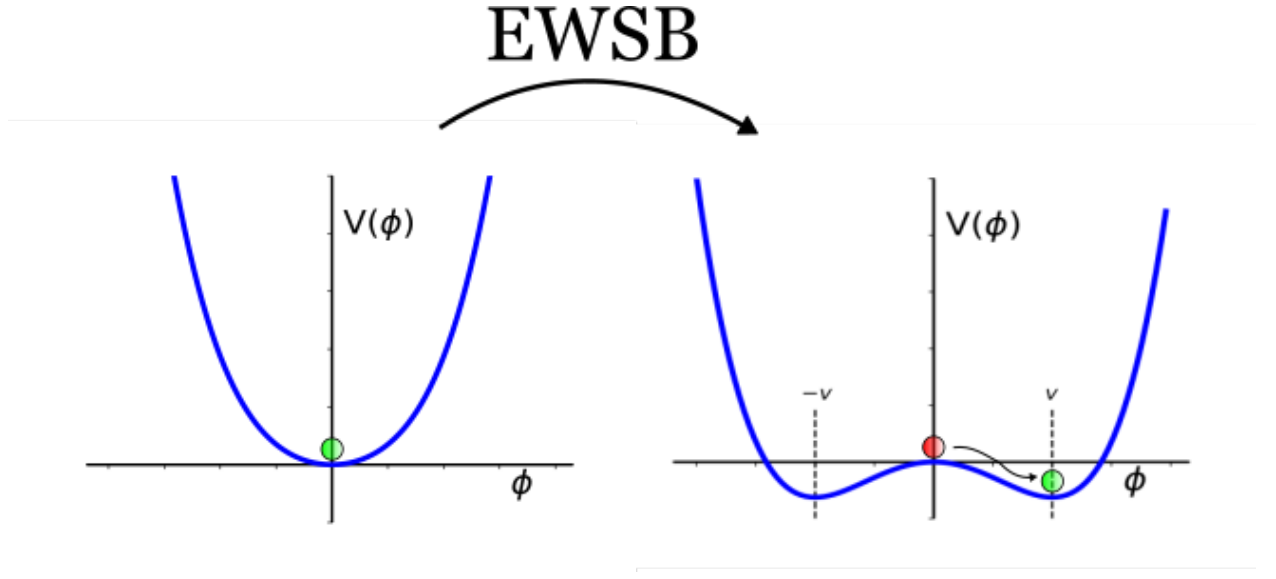


Figure 1.2: Illustration of electroweak symmetry breaking (EWSB). *Left:* Higgs potential with $\mu^2 > 0$ with stable equilibrium at $\phi = 0$. *Right:* With $\mu^2 < 0$, $\phi = 0$ is no longer a stable equilibrium and the Higgs attains a non-zero vacuum expectation value at $\pm v$ — breaking the $SU(2)_L \times \mathcal{U}(1)_Y$ gauge symmetry of the electroweak sector of the SM.

As opposed to ‘eating’ gauge degrees of freedom as in the case of the W^\pm and Z bosons, the fermion masses are obtained by adding additional interaction terms to \mathcal{L}_{SM} between the fermions

and Higgs fields,

$$\mathcal{L}_{f-h} = y_f \left(\bar{L} \phi e_R^- + \phi^\dagger \bar{e}^-_R L \right). \quad (1.22)$$

Since both L and ϕ are $SU(2)$ doublets, adding the right-handed $SU(2)$ singlet terms do not spoil the $SU(2)$ symmetry. When the Higgs field acquires a non-zero vev after EWSB, we can insert Eqn. 1.17 into Eqn. 1.22 to obtain expressions for the fermions masses,

$$m_f = y_f \frac{v}{\sqrt{2}}, \quad (1.23)$$

where the y_f are referred to as the fermion *Yukawa couplings*, and are free parameters of the SM that need to be measured. Additional interactions arise between the fermions and $h(x)$ whose couplings are related to the fermion masses as,

$$\mathcal{L}_{f-h} \propto \frac{m_f}{v} \bar{f} f h. \quad (1.24)$$

The general form Eqn. 1.22 implies that the y_f are matrices representing the Higgs-fermion Yukawa couplings. They can be diagonalized by performing the proper unitary transformations between the weak- and mass-bases of the fermion fields. In the case of the leptons, this rotation is the identity: the lepton's weak eigenbasis is the same as their mass eigenbasis. This is mainly due to the extraordinarily large mass difference between the charged and neutral leptons within each lepton generation [27]. Within the quark-sector, however, the mass- and weak-basis fermion fields differ. This implies that the diagonalization procedure results in mixing among the weak eigenstates of the quark fields to produce the observed mass eigenstates; i.e. the quark mass-eigenstates (d, s, b) are coherent mixtures of the weak eigenstates (d', s', b').⁷ This allows for the flavor-changing processes that are present in charged weak interactions, allowing for interaction terms involving the decay of a quark of one family into that of another family. The amount of mixing in the quark sector is dictated by a 3×3 unitary matrix known as the *Cabibbo-Kobayashi-Maskawa* (CKM) matrix [28] \mathcal{V}_{CKM} , the general form of which has four free parameters: three mixing angles and a complex phase, δ . The off-diagonal terms of the CKM matrix and the value of the mixing angles dictate the amount of flavor mixing in the quark sector. The complex phase δ allows for charge-parity (CP) symmetry violating effects to occur. In fact, this term is the *only* term of the SM that allows for CP-violation — an effect important for providing interactions that are asymmetric between matter and anti-matter fields.⁸

The remaining terms of $V(\phi)$ (Eqn. 1.14) involve only the Higgs field. After EWSB and the

⁷The mixing can be parametrised as either occurring between the up-type, down-type, or a mixture of up- and down-type fields of each $SU(2)$ doublet. Without loss of generality and for simplicity, it is usually given with respect to the down-type quark fields as shown here.

⁸Charge Parity (CP) symmetry refers to the invariance of a theory with respect to swapping particles with their corresponding anti-particles and, additionally, inverting a field's spatial coordinates, $\psi(\vec{x}) \rightarrow \psi(-\vec{x})$. The former is the 'C' symmetry and the latter is the 'P' symmetry.

Higgs field acquiring vev we obtain,

$$V(\phi) \rightarrow V(\phi)_{\text{EWSB}} = -\lambda\nu^2 h^2 - \lambda\nu h^3 - \frac{1}{4}\lambda h^4 + \text{const.} \quad (1.25)$$

where we have ignored the terms already discussed above. The first term of Eqn. 1.25 is the Higgs boson mass term, the second and third are the triple and quartic Higgs self-couplings,

$$\underbrace{m_h = \sqrt{-2\mu^2} = \sqrt{2\lambda v^2}}_{\text{Higgs boson mass}} \quad \underbrace{\mathcal{L}_{hhh} \propto \frac{m_h^2}{v}}_{\text{Triple and quartic Higgs self-couplings}} \quad \underbrace{\mathcal{L}_{hhhh} \propto \frac{m_h^2}{v^2}}_{\text{Triple and quartic Higgs self-couplings}}. \quad (1.26)$$

1.4 The Complete Standard Model, Successes and Shortcomings

Table 1.2: The particle content of the SM after the process of electroweak symmetry breaking.

	Physical Field	Q	Coupling	Mass [GeV]
Leptons	u, c, t	2/3	$(y_i =) 1 \times 10^{-5}, 7 \times 10^{-3}, 1$	$2 \times 10^{-3}, 1.27, 173$
	d, s, b	-1/3	$(y_i =) 3 \times 10^{-5}, 5 \times 10^{-4}, 0.02$	$4 \times 10^{-4}, 0.10, 4.18$
Quarks	e, μ, τ	-1	$(y_i =) 3 \times 10^{-7}, 6 \times 10^{-4}, 0.01$	$5 \times 10^{-4}, 0.106, 1.777$
	ν_e, ν_μ, ν_τ	0	—	—
Bosons	γ	0	$\alpha_{\text{EM}} \simeq 1/137$	0
	Z	0	$\sin \theta_W \simeq 0.5$	91.2
	(W^+, W^-)	(+1, -1)	\mathcal{V}_{CKM}	80.4
	G	0	$\alpha_s \simeq 0.1$	0
Higgs	h	0	λ, μ	125.09

Chapter 2

Experimental Setup

I know of no more encouraging fact than the unquestionable ability of man to elevate his life by a conscious endeavour. It is something to be able to paint a particular picture, or to carve a statue, and so to make a few objects beautiful; but it is far more glorious to carve and paint the very atmosphere and medium through which we look, which morally we can do.

—Henry David Thoreau, *Walden*

The work to be described in the present thesis was done at CERN¹, the particle physics laboratory located along the French-Swiss border just outside of Geneva, Switzerland. CERN is comprised of almost 18,000 personnel, of which over 13,000 are researchers in the field of experimental particle physics. It is a truly international workplace, with the personnel comprised of representatives of over 110 nationalities and who are either working directly for CERN² or for their respective home institutions — universities or national labs — located across more than 70 countries worldwide [29]. These researchers will generally work at any of the independent experiments located along the various beamlines that network throughout the CERN campus (see Fig. 2.1).

At the time of writing, there are four large experiments³ taking place currently at CERN, all located along the Large Hadron Collider (LHC): ALICE [30], LHCb [31], CMS [32], and ATLAS [33]. The CMS and ATLAS detectors are general purpose detectors, with broad research programs, whereas the ALICE and LHCb detectors are specialised for the study of heavy-ion collisions and b -hadron physics, respectively.

This chapter will present a brief introduction to the workings of the LHC in Section 2.1. In Section 2.2, given that the present author is a member of the ATLAS collaboration, a detailed

¹ The acronym CERN was historically derived from ‘Conseil européen pour la recherche nucléaire’. Nowadays, ‘CERN’ has become a standalone name for the lab itself and is currently referred to as the ‘Organisation européenne pour la recherche nucléaire’; or, in English: the ‘European Organisation for Nuclear Research.’

²Of the roughly 18,000 researchers in experimental particle physics, only about 5% are employed directly by CERN itself.

³For the most part, one can interchange the words ‘detector’ and ‘experiment’ when referencing large-scale, long-term particle physics experiments such as those that have taken place over the past few decades: the detectors tend to take on the role of representing the entire collaboration of physicists, engineers and associated personnel, as well as the entire scope of the associated research programs.

description of the various components that make up the ATLAS detector will be presented.

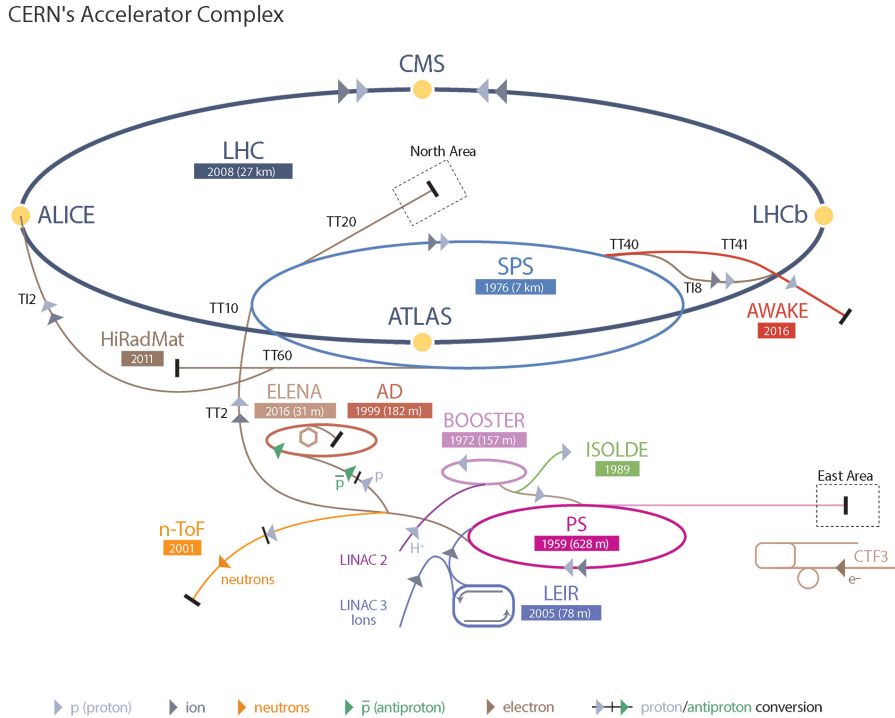


Figure 2.1: Illustration of the various beamlines, accelerator and storage rings, and experimental points that the CERN accelerator complex is home to. The protons that circulate through the LHC, and that are eventually made to collide inside the ATLAS detector, follow the path: Linac 2 → Booster → Proton Synchotron (PS) → Super Proton Synchotron (SPS) → LHC.

2.1 The Large Hadron Collider

The LHC [34] is a circular particle accelerator, with a 27 kilometer circumference, located at an average distance of 100 meters beneath the surface of the Earth. It is nominally used for proton-proton (pp) collisions, wherein two counter-rotating beams of protons are made to collide head-on at specific interaction points (IP) along the 27 kilometer ring, but can also be run in heavy-ion configurations wherein proton-lead ($p\text{-Pb}$) or lead-lead (Pb-Pb) collisions take place.⁴⁵ The pp collisions take priority over those of the heavy-ions, with the collisions each year consisting of only a few weeks in the winter for the heavy-ion configurations and typically six to seven months for the pp configuration. The LHC is designed to accelerate protons to a center-of-mass energy of $\sqrt{s} = 14 \text{ TeV}$.

⁴The specific lead (Pb) species used in collisions is $^{208}_{82}\text{Pb}$.

⁵ More rarely, the LHC can also be used to circulate gold (Au) ions. There are even plans to have proton-oxygen ($p\text{-O}$) runs in the future, which will allow for the LHC experiments to provide research that potentially complements dark matter research based on cosmic-ray air showers.

2.1.1 Machine Design and Layout

Machine Composition

The LHC was planned as the successor to the Large Electron Positron (LEP) collider [35, 36], which was in operation between the years of 1989 to 2000. LEP is still the most powerful lepton collider to date, having maximal electron-positron center-of-mass collision energies of 209 GeV. After LEP, the particle physics community knew that the next collider at CERN needed to have $\mathcal{O}(10)$ TeV collision energies; either to be able to probe from all angles any new physics discovered at LEP and/or the Tevatron [37], or to provide the necessary power to search for still-elusive hints of BSM physics. At the very least, given a non-discovery of the Higgs boson at LEP and the Tevatron, the community would need a discovery machine powerful enough to produce electroweak-scale Higgs bosons and an $\mathcal{O}(10)$ TeV hadron collider — as we now know — is sufficient for this job.

In order to increase center-of-mass collisions energies, collider designs can take two routes: they can either increase in size, that is, have larger circumferences (radii), or they can increase the strength of the magnetic fields used to keep the circulating charged particles in orbit. This can be seen by first considering the expression for the relativistic cyclotron frequency, ω , of a particle moving in a circular orbit,

$$\omega = \frac{qB}{\gamma m}, \quad (2.1)$$

where m is the particle's rest mass, B is the magnitude of the magnetic field experienced by the particle, q is the particle's electric charge, and γ is the relativistic Lorentz factor, $\gamma = \sqrt{1 - \beta^2} = \sqrt{1 - (v/c)^2}$, with v the particle's velocity and c the speed of light. Using Eqn. 2.1, it can be seen that a particle of higher energy confined to a fixed circular orbit necessarily has a higher angular velocity by relating the particle's angular velocity to its kinetic energy:

$$E_{\text{kin}} \propto mv^2 = m(\omega R)^2 = \frac{q^2 B^2 R^2}{m\gamma^2}. \quad (2.2)$$

In planning the construction of the LHC, the costs in civil engineering and real-estate works that would be required to construct a larger tunnel in which to house the LHC ring (increasing R) far outweighed the costs of research into and development of magnet systems strong enough to bend the multi-TeV particles along the beam orbit prescribed by the already-existing LEP tunnel (increasing B). The desired center-of-mass collision energy of $\mathcal{O}(10)$ TeV, the fact that the LHC would be a hadron (proton) collider, and the fact that the LHC would be using the existing LEP tunnel dictate the required magnetic field strength needed to keep the protons in stable orbits at the LHC. This is seen by using Eqn. 2.2, solving for B , and comparing the LHC and LEP design

parameters,

$$\begin{aligned}
\frac{B_{\text{LHC}}^2}{B_{\text{LEP}}^2} &= \frac{(E_{\text{LHC}} m_{\text{LHC}} \gamma_{\text{LHC}}^2) / (q_{\text{LHC}}^2 R_{\text{LHC}}^2)}{(E_{\text{LEP}} m_{\text{LEP}} \gamma_{\text{LEP}}^2) / (q_{\text{LEP}}^2 R_{\text{LEP}}^2)} \\
&= (E_{\text{LHC}} / E_{\text{LEP}}) \times (m_{\text{LHC}} / m_{\text{LEP}}) \times (\gamma_{\text{LHC}}^2 / \gamma_{\text{LEP}}^2) \times (q_{\text{LEP}}^2 / q_{\text{LHC}}^2) \times (R_{\text{LEP}}^2 / R_{\text{LHC}}^2) \\
&\approx (1 \text{ TeV} / 0.2 \text{ TeV}) \times (m_p / m_e) \times (1) \times (1) \times (1) \\
&\approx 10^4,
\end{aligned} \tag{2.3}$$

which shows that the strength of the LHC bending magnets must be on the order of $100\times$ the strength of those used at LEP. The magnetic fields experienced by the electron and positron beams at LEP were 0.22 Tesla. By Eqn. 2.3, the LHC bending magnets should achieve magnetic field strengths on the order of 10 Tesla in order to achieve the desired collision energies. The maximum achievable magnetic field of conventional ferrormagnets is about 2 Tesla. To meet the $\sqrt{s} \approx 10$ TeV design goal, the magnet system used by the LHC to confine the protons to their circular orbits must then be composed of *superconducting* electromagnets. The entire magnet system of LEP was therefore removed and replaced with superconducting niobium-titanium (Nb-Ti) alloy based electromagnets which are superconducting at temperatures below 10 K. To reach temperatures below this 10 K threshold, the LHC magnets are housed in cryostats that allow for the Nb-Ti elements to be fully submerged in a bath of superfluid Helium at a temperature of 1.9 K [38]. In total, the LHC contains more than 120 tonnes of superfluid Helium. It goes without saying that there is a significant amount of resources and person power at CERN devoted to the refrigeration and cryogenics systems that are required for the LHC to run.

Additionally, the fact that LEP was a *particle-antiparticle* collider meant that the counter-rotating beams could be made to occupy a single ring: the same magnetic field could produce counter-rotating beams of electrons and positrons within the same beam pipe.⁶ As a result, the LEP beam tunnel was constructed with only a single ring in mind and is relatively narrow: the LEP tunnel, and therefore LHC tunnel, is only ≈ 3.7 m wide on average. As the LHC is a *particle-particle* collider, it necessarily requires *two* magnetic fields of opposing polarity to circulate one of its beams in the clockwise direction and the other in the counter-clockwise direction. Given the limited space in the tunnel, however, it is not possible to house two separate rings of superconducting bending magnets with all of the services that they require *in addition* to the requisite minimal space needed for personnel and maintenance access. This forced the need of the so-called ‘2-in-1’ design of the main bending magnets of the LHC, wherein the two beam pipes are housed in the same cryostat in which the counter-rotating beams are held in their respective orbits by coupled magnetic fields. An illustration of this now-iconic design of the LHC bending (dipole) magnets and surrounding cryostat and containment structure is illustrated in Figure 2.3. Each of the 15 meter long superconducting dipole electromagnets of the LHC responsible for constraining the protons to their circular orbits

⁶The electrons and positrons at LEP were vertically separated within the beam pipe by electrostatic separators placed throughout the LEP ring. Turning off these separators is, to first approximation, how the LEP operators would get the electrically-attracting electrons and positrons to collide.

has currents of 11850 Amperes flowing through it and achieves magnetic field strengths of 8.33 Tesla.

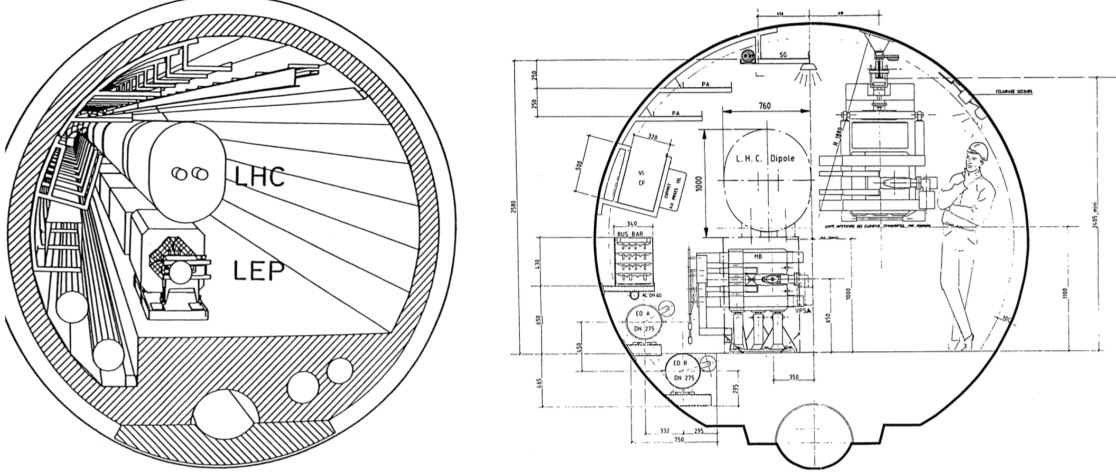


Figure 2.2: *Left:* Illustration comparing the size of a prototype ‘2-in-1’ LHC dipole configuration to the LEP dipole and how they fit inside of the LEP/LHC tunnel. Note that prior to LHC operation, the LEP magnets will have been removed: the two are shown side-by-side for comparison purposes only. *Right:* Cross-sectional view of the LEP/LHC tunnel with a comparison of the LHC ‘2-in-1’ dipole on top of the LEP dipole. An illustration of an average size person is shown for scale. Also shown is the service crane in use, to give an idea of the size required for potential maintenance access. Clearly, two single-bore, superconducting rings each similar in size to the LEP dipole would not fit comfortably in the tunnel. The LHC ‘2-in-1’ design fits in nearly the same area as the LEP dipoles while additionally being able to contain both particle beams. Figures are taken from Ref. [39].

Connecting the Dots

The LHC is essentially a chain of superconducting magnets of the type described in the previous paragraphs, where the the bending (dipole) magnets critical to the LHC design were introduced. The chain is laid in a double-octagonal structure, illustrated in Figure 2.4. There are eight octants, at the center of which the LHC ring is straight and does not curve. The LHC curvature occurs at the boundaries of each of the octants and is primarily made up of bending (dipole) magnets. The straight sections are where the interaction regions are located and are referred to as ‘Points’, numbered 1 to 8. Points 1, 2, 5, and 8 are where the four large LHC experiments are located. Points 1 and 5 are home to the services and underground areas of the general purpose experiments, ATLAS and CMS, respectively. The underground experimental caverns associated with Point 1 and 5 were not present for LEP and had to be constructed after LEP was retired in 2000. Figure 2.5 provides an illustration of how the surface and underground areas are situated at Point 1. Points 2 and 8 host the services and underground areas of the ALICE and LHCb experiments, respectively. At these Points, Points 1, 2, 5, and 8, the counter-rotating beams are made to collide. The remaining Points, Points 3, 4, 6, and 7, are host to various beam ‘services’ necessary for the operation of the

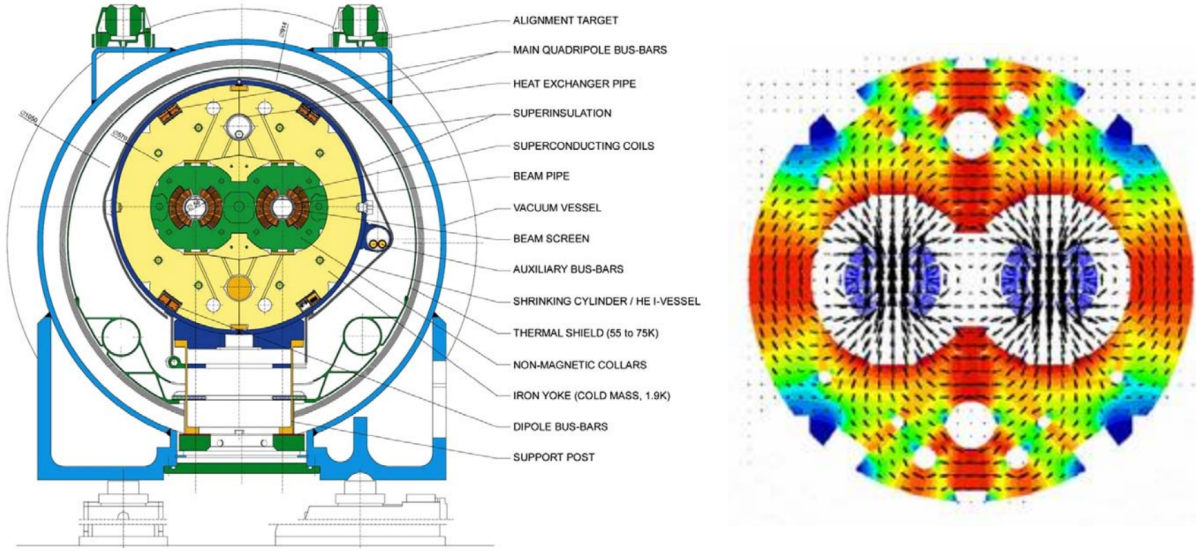


Figure 2.3: *Left:* Cross-sectional view of an LHC dipole bending magnet, with relevant parts indicated. The protons orbit inside of the beam pipes, each of which has a diameter of roughly 3 cm. It is interesting to note that the non-magnetic steel collars (in green) are of critical import to the success of the magnet systems. They are required to prevent the dipole structure from being deformed or torn apart due to the intense magnetic forces tending to push the two beam-pipes apart as a result of their counter-rotating electromagnetic currents. These forces amount to about 400 tonnes per meter of dipole when in full operation — almost equivalent in magnitude to the weight of a Boeing 747. *Right:* Magnetic field lines of the coupled dipole fields that bend the counter-rotating proton beams and keep them in their circular orbits around the LHC ring.

LHC. Point 3 and 7 host the beam betatron and momentum cleaning ('beam collimation') systems, respectively. Point 4 hosts the superconducting radio-frequency (RF) systems which accelerate the beams to their nominal collision energies. Point 6 is the location of the beam-abort system — the so-called 'beam dump' — where the LHC beams may be removed very quickly from the LHC ring by using *kicker* magnets [40] that divert the beams out of the LHC ring in a safe manner. The beams may be dumped if the LHC wishes to refill with protons (or heavy-ions) and needs to remove any remnants of the previous fill, in case of beam instabilities observed in the LHC ring, or if one of the experiments signals the need for a beam dump (in case of beam stability or detector issues observed at the associated IP).

2.1.2 Injection Chain and Bunch Structure

We now have an idea of how the proton beams relevant to the work in this thesis are made to circulate in the LHC ring. In this section we will briefly describe the initial source of the protons and how they are introduced into the LHC ring. The LHC relies on a series of pre-acceleration steps that bring the initial low-energy protons to energies sufficient enough to begin their journey through the LHC. The sum-total of these steps is referred to as the LHC *injection chain* [42]. The

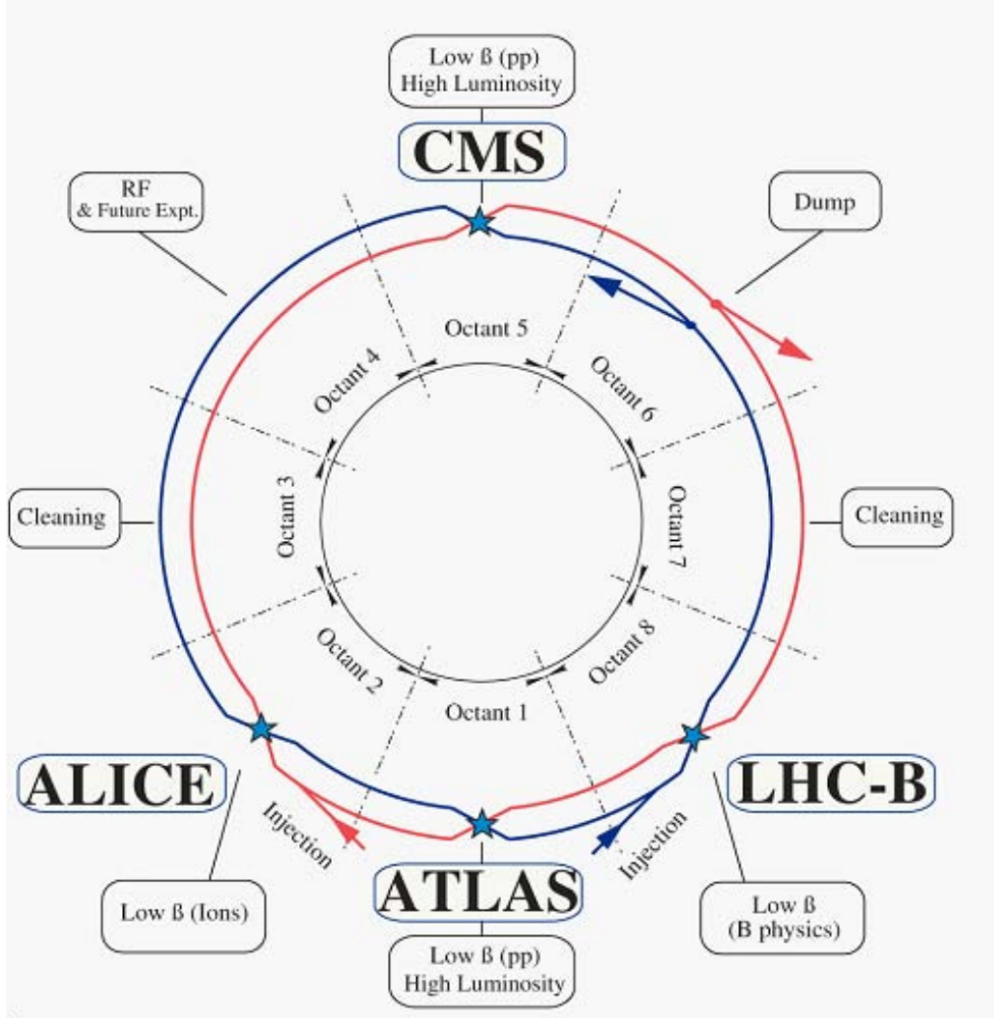


Figure 2.4: Layout of the LHC and its two counter-rotating beams. Beam 1 is in blue and rotates counter-clockwise. Beam 2 is in red and rotates clock-wise. At the center of each octant is a straight section which houses the experimental caverns or LHC beam facilities. At the boundaries of each octant are located the curved sections. Figure taken from Figure 2.1 of Ref. [34]. **Somewhere β should be described – betatron function**

components of the LHC injection chain form the heart of the CERN accelerator complex illustrated in Figure 2.1. For pp collisions in the LHC, the protons are initially sourced from Hydrogen atoms that are released at the start of Linac 2. The Hydrogen atoms are immediately stripped of their electrons after passing through the *duoplasmatron* ion source [43]. The protons are then passed through Linac 2, a linear accelerator, which accelerates the protons to 50 MeV. They then enter the Proton Synchotron Booster (PSB), a circular storage ring composed of four stacked rings, which accelerates the protons to 1.4 GeV. The PSB injects the protons into the Proton Synchotron (PS) which accelerates them to 25 GeV. The Super Proton Synchotron (SPS) receives the protons from the PS and accelerates them to 450 GeV. At this point the protons have sufficient energy

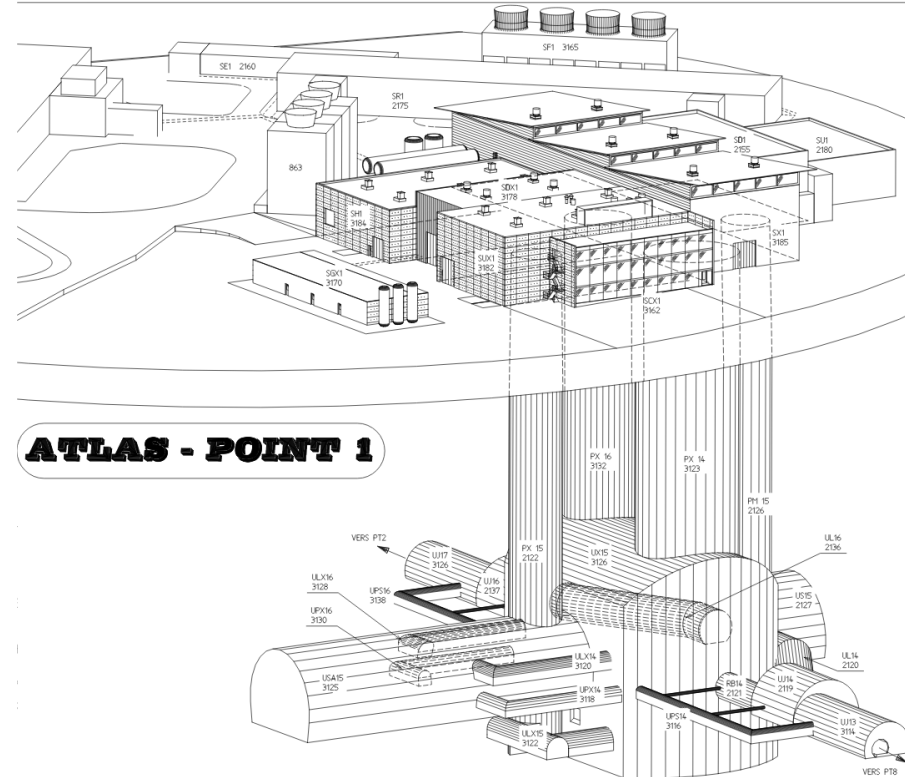


Figure 2.5: Diagram showing the surface buildings and services and underground areas of Point 1, where the ATLAS experiment is located. The LHC ring can be seen at the bottom, with its directions indicated by the ‘VERS PT8 (2)’ arrows pointing towards Point 8 (2). The experimental cavern in which the ATLAS detector sits is UX15. The control room for the ATLAS experiment, whereat operators can monitor and control the state of the ATLAS detector, is located 100 m above UX15 in the building SCX1. Figure taken from Figure 10.1 of Ref. [41].

to be injected into the LHC. There are two injection points into the LHC since, up until this stage, the protons are circulating in the same direction: one injection point sends protons into the counter-clockwise beamline of the LHC, and the other into the clockwise beamline. Until all of the protons from a single *fill* make their way into the LHC, they will circulate at the injection energy of 450 GeV. After the filling completes⁷, the superconducting RF cavities located at Point 4 will begin to accelerate the protons to their final collision energies.⁸ The acceleration is achieved by increasing the frequency of the RF oscillations; however, given that a 450 GeV proton is already ultra-relativistic, the adjustment of the frequency needed to get to the collision energies is not large but still has consequences for the design of the detector and measurement apparatus along the LHC ring [44].

The proton beams circulating the LHC are not a continuous stream of protons; rather, they are grouped into what are referred to as *bunches*. The protons arrive at the LHC in these bunches

⁷A standard LHC fill takes on the order of 4 minutes per ring.

⁸If all goes smoothly, this acceleration stage takes roughly 20 minutes.

which are initially prepared in the smaller machines that make up the LHC injection chain and then are kept in their final *bunch structure* by the RF cavities. The accelerating RF cavities provide an accelerating electromagnetic field that oscillates longitudinally. The bunches, each composed of roughly 10^{11} protons, are then made to oscillate longitudinally in so-called *synchotron oscillations* around the central node of the RF oscillation as they circulate through the LHC ring. The proton bunches are then effectively ‘shaped’ by the oscillating RF field: protons in a bunch lagging behind or that are ahead of those particles at the center of the bunches will be accelerated or decelerated accordingly so as to be pushed back into the center of the bunch. The LHC RF cavities have an oscillation frequency of 400 MHz which defines the boundaries in which proton bunches can lie. These boundaries are called *RF buckets* and, along with the circumference of the LHC, dictate the number of proton bunches that can potentially fit in the LHC. The relationship between the RF oscillations and the RF bucket and bunch structure is illustrated in Figure 2.6. In total, approximately 35640 RF buckets exist when the LHC is in operation. Not all buckets contain proton bunches, however. In fact, at the time of the writing of the present thesis, RF buckets filled with proton bunches have a minimal separation of 10 RF buckets, meaning that following an RF bucket containing a proton bunch there is at least 9 unfilled RF buckets. This corresponds to a minimal time between proton bunches — the *bunch spacing* — of 25 nanoseconds. At the time of the present thesis, the operating conditions of the LHC maximally allow for 2808 25 ns-spaced bunches.⁹ The bunch-spacing and overall bunch structure of an LHC fill is not only decided by the operators of the LHC but also by what the detectors at Points 1,2,5, and 8 can tolerate. This is because shorter bunch spacing means higher intensity and multiplicity of collisions occurring at each of these IP. A 25 nanosecond bunch spacing corresponds to a maximal pp collision rate of 40 MHz. The detectors at each of the IP have been designed with this collision rate in mind and anything higher may push them beyond their design limits.

2.1.3 The Concept of Luminosity

In designing a particle collider, the collision energy is not the only important parameter. Equally important is the value of the instantaneous *luminosity* that can be achieved by the collider. An expression for the instantaneous luminosity, \mathcal{L} , is given by,

$$\mathcal{L} = \frac{N^2 n_b f}{4\pi \sigma_x \sigma_y} \cdot S, \quad (2.4)$$

where N is the number of particles per bunch, n_b is the number of colliding bunches, f is the bunch revolution frequency, $\sigma_{x,y}$ are the transverse beam widths in the Gaussian approximation,

⁹ The number of allowed bunches is significantly lower than the 35640 RF buckets with 25 ns bunch-spacing potentially allow for. This is due, in part, to the non-trivial bunch-structure typically employed but also in large part to the fact that there is a $\approx 30 \mu s$ *abort gap* in the LHC ring where no filled RF buckets exist. The abort gap is a number of continuous unfilled RF buckets that allows the ramp up of the kicker magnets used for the beam dump to occur in the absence of filled buckets. In this way, the kicker magnet ramp up does not disturb the structure of the circulating proton beams. Only after this ramp up is finished should the kicker magnets disturb the beams.

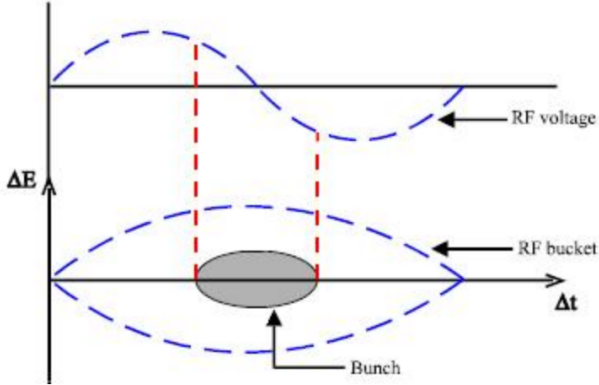


Figure 2.6: Illustration of the particle bunch structure in a particle collider such as the LHC. The particles are accelerated by radio-frequency (RF) oscillations whose amplitude is illustrated in the upper plot. The RF bucket’s boundary, illustrated in the lower plot, is defined by a full period of the RF oscillation and the particle bunch formation, depicted in grey, occurs at the central node of the oscillation. The area occupied by the particle bunch is related to the beam’s longitudinal *emittance*.

and S is a reduction factor that accounts for geometric factors such as the non-zero crossing-angle of the colliding beams [42, 45]. The instantaneous luminosity, \mathcal{L} , can be seen by Eqn. 2.4 to have units of $\text{cm}^{-2}\text{s}^{-1}$ and can be conceptually thought of as the outgoing flux of particles per unit area and time after a bunch crossing in which successful pp collisions occur. The LHC is designed to deliver collisions to the high luminosity IP (Fig. 2.4) at $\mathcal{L} = 10^{34} \text{ cm}^{-2}\text{s}^{-1}$. Accurate knowledge of \mathcal{L} is of the utmost importance for collider design and operation. Not only does it parametrise the potential collision rate once the collider beam and bunch structure are decided, but it allows for the accurate prediction of the number of collision events, N_{proc} , associated with a particular physics process with cross-section σ_{proc} ,

$$N_{\text{proc}} = \sigma_{\text{proc}} \int \mathcal{L} dt \equiv \sigma_{\text{proc}} \cdot L, \quad (2.5)$$

where L is referred to as the *integrated luminosity* and has units of cm^{-2} . A common unit for integrated luminosity is the *barn*, with symbol ‘b’: one barn is defined as 10^{-24} cm^{-2} . The datasets collected so far by the LHC experiments are such that the *femtobarn* (fb), 10^{-39} cm^{-2} , is relevant.

2.1.4 Operation of the Large Hadron Collider

The LHC has been in stable operation since 2009. It operates in so-called *runs*: multi-year periods of roughly continuous data-taking. As CERN shuts down during the winter months, each run is segmented each year with a several month long shutdown in the winter with a ramp-up period in the spring. During these shorter shutdowns, maintenance and upgrades may take place. In between a given run there is a multi-year break, a *long shutdown*, in which large(er)-scale maintenance and

upgrades of both the LHC and the experiments can take place. At the time of writing, there has so far been two runs of the LHC, Run-I and Run-II. Run-I took place during the years 2009–2012 and Run-II during 2015–2018. The integrated luminosities for each of the data taking years between Run-I and Run-II is shown in Fig. 2.7. The data relevant to the work presented in this thesis were collected in both Run-I and Run-II of the LHC, specifically that data collected in the years 2012–2018. The luminosities, instantaneous and integrated, as well as the center-of-mass collision energies, \sqrt{s} , for these data-taking periods are shown in Table 2.1. Also shown in Table 2.1 are the average values of the mean number of interactions per bunch crossing, $\langle\mu\rangle$, observed during each data-taking year. The quantity $\langle\mu\rangle$ is related to the amount of *pileup* observed during data-taking. Pileup is caused by overlapping pp interactions within the same (*in-time* pileup) or neighboring (*out-of-time* pileup) bunch-crossing(s) at the interaction point. The pileup scales with the instantaneous luminosity. Distributions of $\langle\mu\rangle$ are shown in Fig. 2.7 for the Run-II data-taking period.

	Run-I	Run-II			
	2012	2015	2016	2017	2018
Collision energy, \sqrt{s} [TeV]	8		13		
Peak Luminosity, \mathcal{L} [$\text{cm}^{-2}\text{s}^{-1}$] ($\times 10^{34}$)	0.77	0.5	1.4	2.1	2.1
Integrated Luminosity, L [fb^{-1}]	20.2	3.2	33.0	44.3	59.9
Mean number of interactions per bunch crossing, $\langle\mu\rangle$	20.7	13.4	25.1	37.8	36.1

Table 2.1: Summary parameters for the data-taking periods relevant to the work presented in this thesis. The integrated luminosity is that relevant to performing physics analysis and potentially differs with respect to the total integrated luminosity delivered to ATLAS by the LHC (Fig. 2.7) due to the application of strict quality criteria on the data prior to its use in physics analyses.

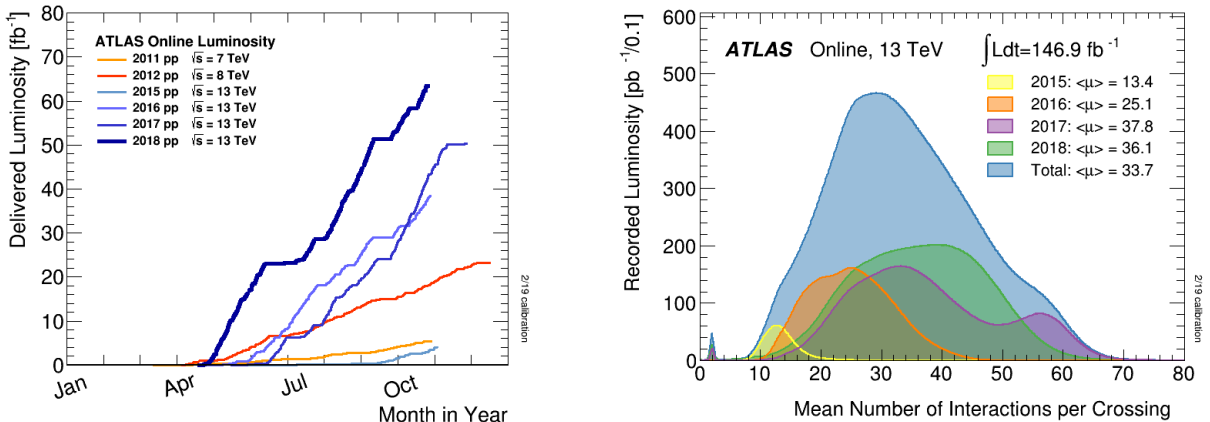


Figure 2.7: *Left:* The ATLAS integrated luminosity during the data-taking years 2011–2018. *Right:* The observed average number of pp interactions per bunch-crossing, $\langle\mu\rangle$, observed by ATLAS during the Run-II data-taking years, 2015–2018.

2.2 The ATLAS Detector

In this section we will extend our focus to the ATLAS detector, the general purpose particle detector located at Point 1 of the LHC ring (see Figure 2.5). Roughly cylindrical in shape, coaxial with the beam-pipe, the ATLAS detector is 44 m long and 25 m tall. It is by far the largest such detector ever built and, generally, is the largest and most complex device ever constructed. Being general purpose in scope, the ATLAS detector is hermetic and has nearly 4π radians of solid angle coverage around the pp collision point. Such detectors are commonly designed to have various subsystems — *subdetectors* — which are designed for the identification of specific types of particles and interactions. They tend to be layered about the interaction point and cylindrically symmetric since the pp interactions taking place within the detector have no preferred direction in the plane transverse to the direction in which the proton beams are travelling. A view of the ATLAS detector and its subdetectors is provided by Figure 2.9. In the following we will briefly describe each subsystem in turn, describing first the detectors located nearer to the pp collision and proceeding outwards.

2.2.1 The ATLAS Coordinate System

The ATLAS detector uses a right-handed coordinate system with the origin located at the geometric center of the detector. The x -axis points to the center of the LHC ring, the y -axis points upwards and away from the center of the Earth, and the z -axis is along the beam-pipe. The side associated with positive (negative) z is referred to as the ‘A’ (‘C’) side of the detector.¹⁰ Due to its cylindrical symmetry, ATLAS also uses the cylindrical coordinates, (r, ϕ, z) , with ϕ the azimuthal angle about the z -axis and having $\phi = 0$ along the positive x -axis. The spherical polar angle, θ , is defined with respect to the z -axis, having $\theta = 0$ parallel to the beam-pipe and $\theta = \pi/2$ in the xy -plane transverse to the beam-pipe. The pseudorapidity, η , is commonly used when describing systems of particles or locations within the detector and is defined as $\eta = -\ln [\tan(\theta/2)]$. The relationship between pseudorapidity and polar angle is illustrated in Figure 2.8. Large (small) values of η correspond to the *forward* (*central*) region of the detector. The rapidity, y , is related to η and is defined as $y = \frac{1}{2} \ln [(E + p_z)/(E - p_z)]$. The pseudorapidity of a particle traversing the detector is equal to its rapidity if the particle is massless or ultra-relativistic; otherwise, they are different. The comparison between a particle’s pseudorapidity and rapidity is illustrated in Figure 2.8. The coordinates used to describe systems of particles are typically described by their four-momenta: (p_x, p_y, p_z) or, equivalently, (p_T, η, ϕ) . A distance metric commonly used to describe the distance between two systems of particles in the detector is $\Delta R = \sqrt{(\Delta\eta)^2 + (\Delta\phi)^2}$. The ΔR quantity using y instead of η is also sometimes used and will be indicated by ΔR_y .

¹⁰‘A’ for ‘airport’, since this is the side pointing towards Geneva International Airport, and ‘C’ for either ‘Crozet’ or ‘Charly’s’, depending on who you ask, since this is the side pointing towards the town of Crozet and/or Charly’s Pub in the town of Saint-Genis-Pouilly.

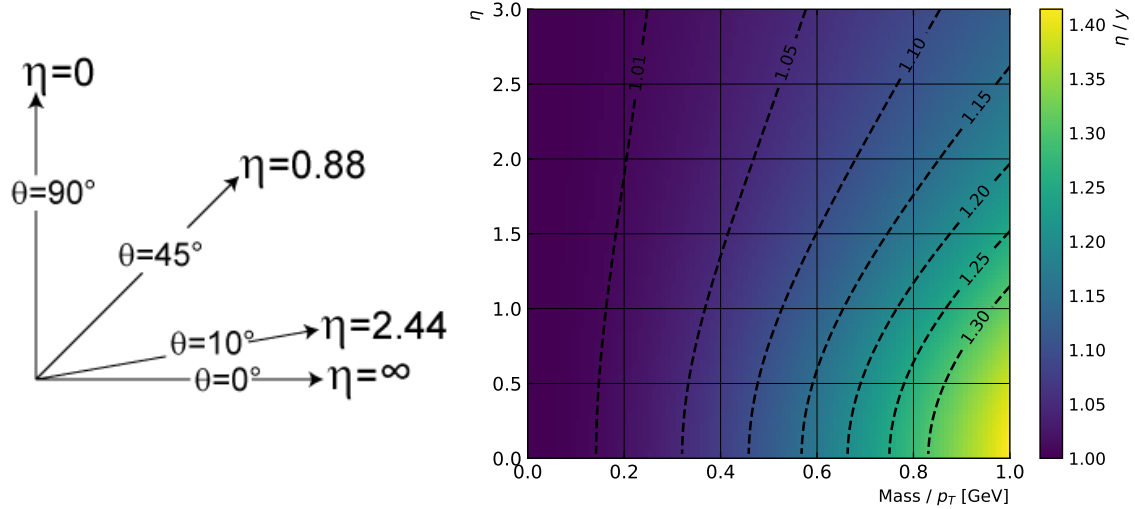


Figure 2.8: *Left*: Illustration of the relationship between the pseudorapidity, η , and polar angle, θ , defined as the angle with respect to the beam-axis (z -axis). *Right*: Distribution of the ratio of a particle's pseudorapidity to its rapidity, η/y , as a function of its pseudorapidity (y -axis) and the ratio of its mass to its transverse momentum, p_T (x -axis).

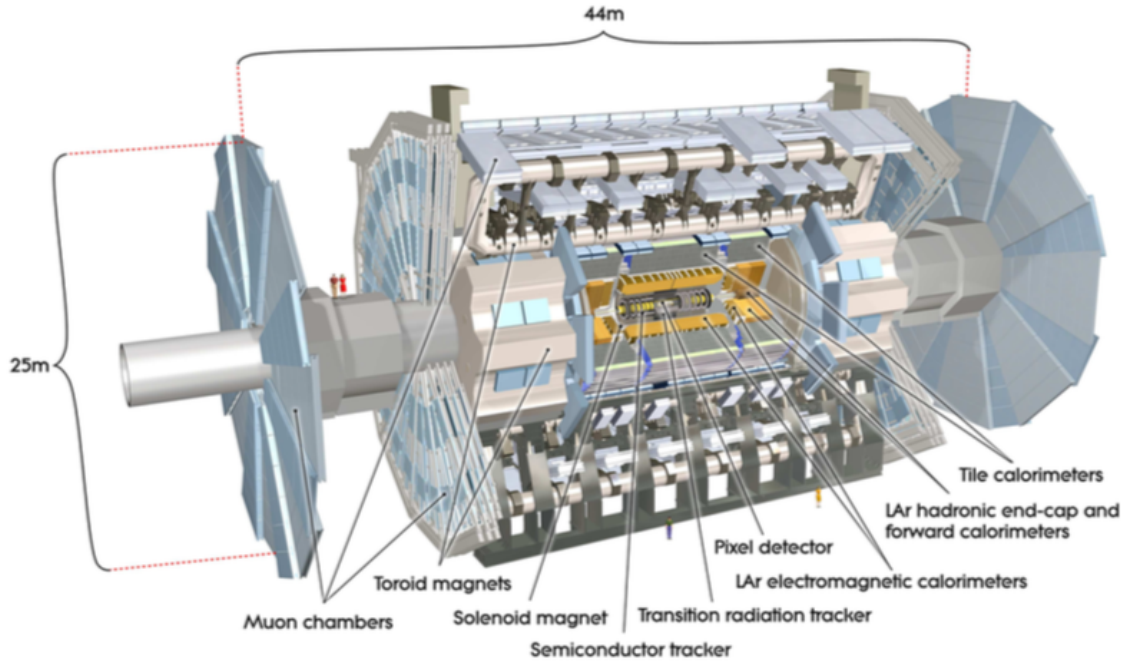


Figure 2.9: Cut-away view of the ATLAS detector with sub-systems indicated. Shown for comparison are figures of average-height humans standing at the feet of the detector and standing on the forward shielding between the big wheels of the forward muon system.

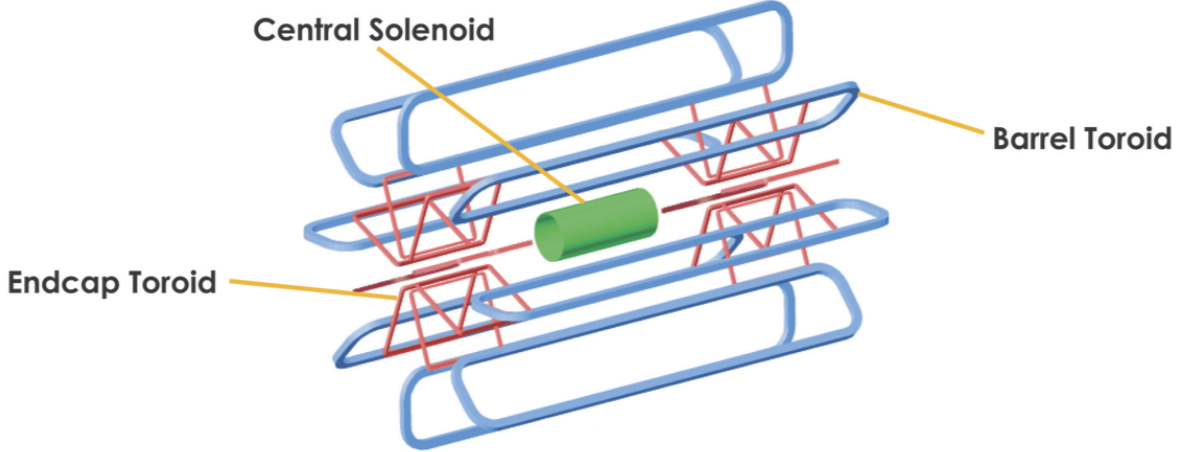


Figure 2.10: A view of the ATLAS magnet system. Shown are the 2 T solenoid magnet in green, the barrel toroid system in blue, and endcap toroid magnets in red.

2.2.2 The Inner Detector

The innermost subdetector of ATLAS is the Inner Detector (ID) [46]. The ID covers the region $|\eta| < 2.5$ and is composed, in order of increasing radial distance from the beam-pipe, of the silicon pixel detector, the silicon-strip semiconductor tracker (SCT), and the transition radiation tracker (TRT). These detectors enable the reconstruction of the tracks associated with the $\mathcal{O}(1000)$ charged particles emerging from each pp bunch collision occurring every 25 ns. An illustration of the ID and its subdetectors is shown in Figure 2.11. Additional, more detailed views of the barrel and endcap sections of the ID are shown in Figure 2.12. The ID is situated inside of the central solenoid, indicated in Figure 2.10, which provides an axial 2 T magnetic field and extends over a length of 5.3 m with a diameter of 2.5 m. The bending of charged particles in the xy -plane due to the presence of the solenoidal field allows for their momenta to be measured using the curvature of their reconstructed tracks.

The Pixel Detector and IBL

The pixel detector is the innermost subdetector of the ID, situated very near to and surrounding the beam-pipe. It is composed of three separate sections: a barrel section and two end-cap sections. The barrel section of the pixel detector has a cylindrical geometry and the end-cap sections are disks centered on the beam-pipe. The barrel section has four layers, each with increasing radius, and there are three disks in each of the end-caps. This ID geometry, shown in Figure 2.12, covers the region $|\eta| < 2.5$.

The pixel detector, being so near the pp collisions, is subject to the highest particle fluxes of any other subsystem. As a result, it is built to have very fine granularity: its sensing elements consist of $250 \mu\text{m}$ thick detectors housing pixels of reverse-biased n-type silicon semiconductor material, each having a nominal size of $50 \times 400 \mu\text{m}^2$. In total, there are roughly 80 million channels read

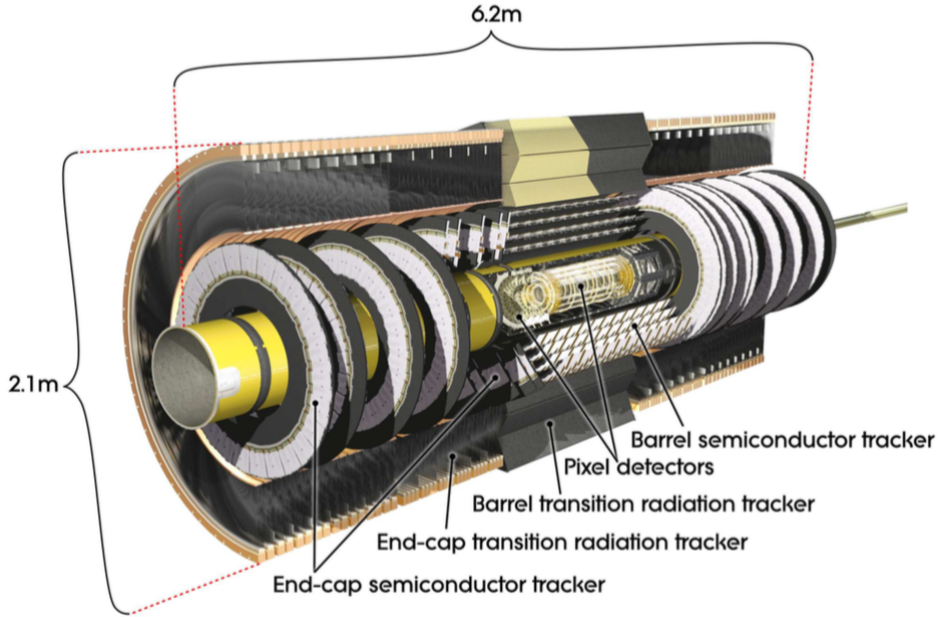


Figure 2.11: Cross-sectional view of the ATLAS inner detector. Shown are the barrel and end-cap portions of the pixel, SCT, and TRT detectors.

out from the pixel detector alone. This allows for the pixel detector's fine spatial hit resolution of $10\ \mu m$ in $(r - \phi)$ and $115\ \mu m$ along z .

The innermost layer of the pixel detector's barrel section is referred to as the *Insertable B-Layer* (IBL), and was installed at the beginning of the Run-II data-taking period [47]. It corresponds, essentially, to the instrumentation of the ATLAS beam-pipe, as seen in Figure 2.14, and is located at a radial distance of 3.3 cm. It alone accounts for 8 million readout channels of the pixel detector — resulting in an ultra precise spatial hit resolution of $8\ \mu m$ in $(r - \phi)$ and $40\ \mu m$ along z . Beyond improving the overall measurements and reconstruction of charged particle tracks, the IBL was installed in order to improve the performance of secondary vertex reconstruction — an essential ingredient to the algorithms associated with the reconstruction and identification of jets originating from the decays of b -hadrons whose decays occur at radial distances frequently beyond that of the IBL, as illustrated in Figure 3.16..

The Semiconductor Tracker

The semiconductor tracker (SCT), like the pixel detector, uses silicon semiconductor-based sensing elements. It surrounds the pixel detector, as illustrated in Figure 2.12, and has similar barrel and end-cap geometries. The barrel section of the SCT is composed of 4 cylindrical layers and the end-caps consist of 9 disks. The silicon sensing elements are in a strip-like geometry with $80\ \mu m$ strip pitch. The strips in the barrel section run parallel to the beam-pipe and those in the end-caps

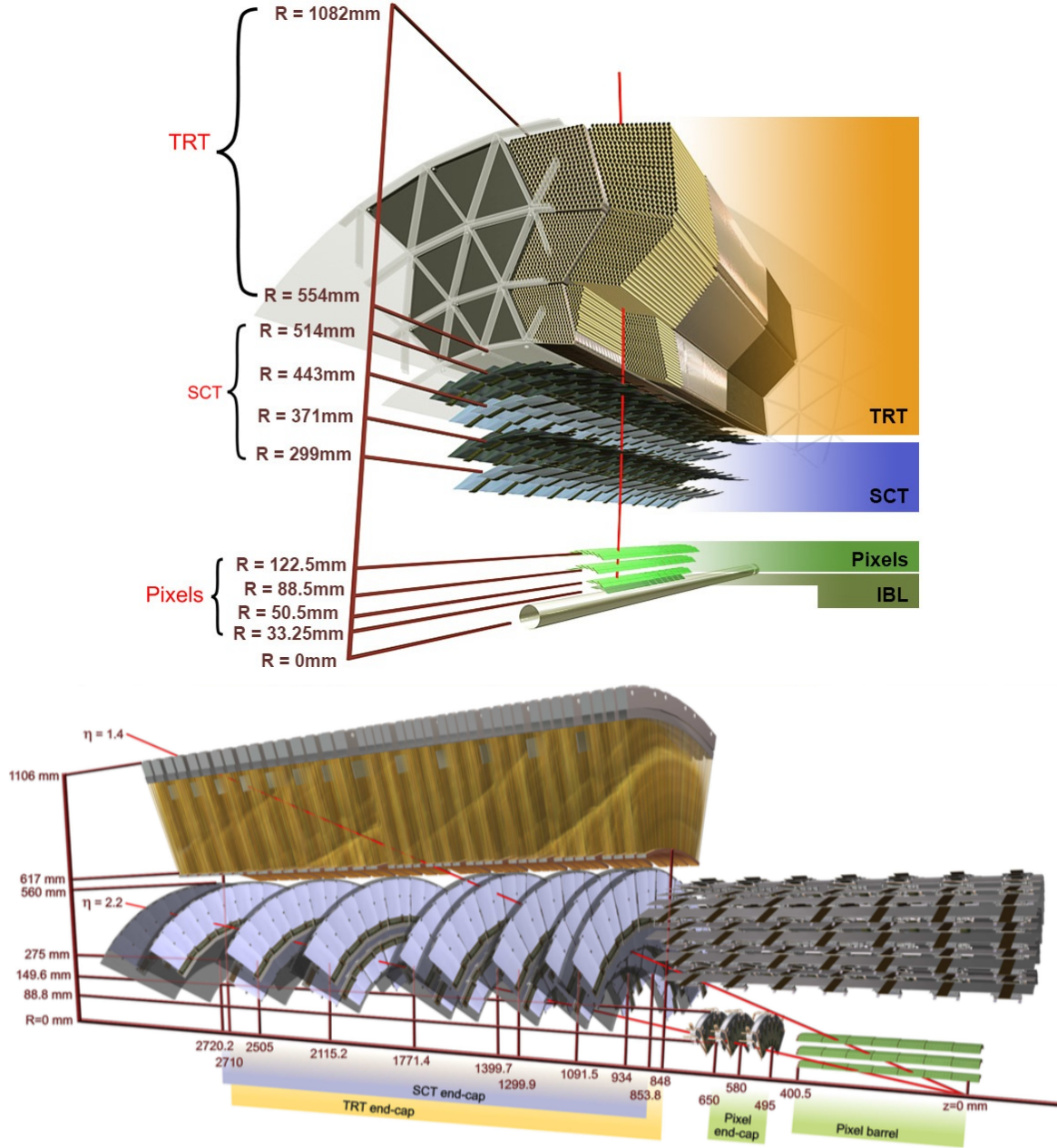


Figure 2.12: Cut-away views of the barrel (top) and end-cap (bottom) portions of the ATLAS inner detector, with each of the three subdetectors indicated along with their envelopes in r and in z .

are perpendicular, extending along the radial direction.¹¹ The spatial hit resolution of the SCT is

¹¹ The SCT layers in both the barrel and end-cap sections additionally contain small-angle (40 mrad) stereo strips to allow for measurement of both ($r - \phi$) and z information.

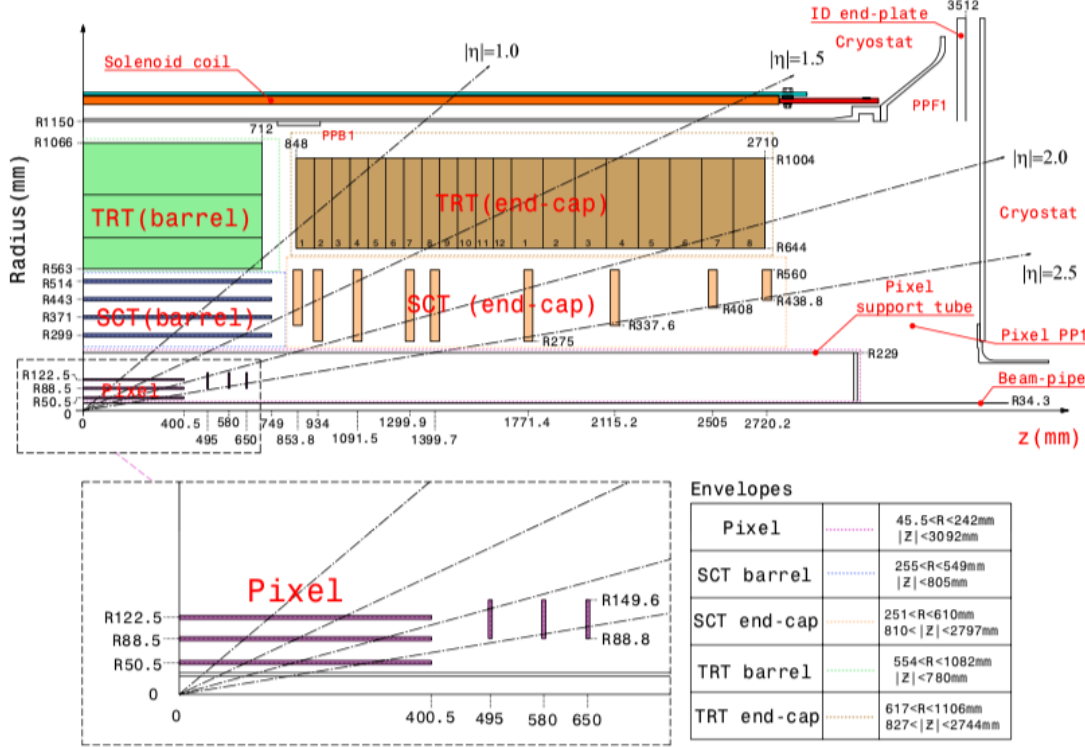


Figure 2.13: From Ref. [33].

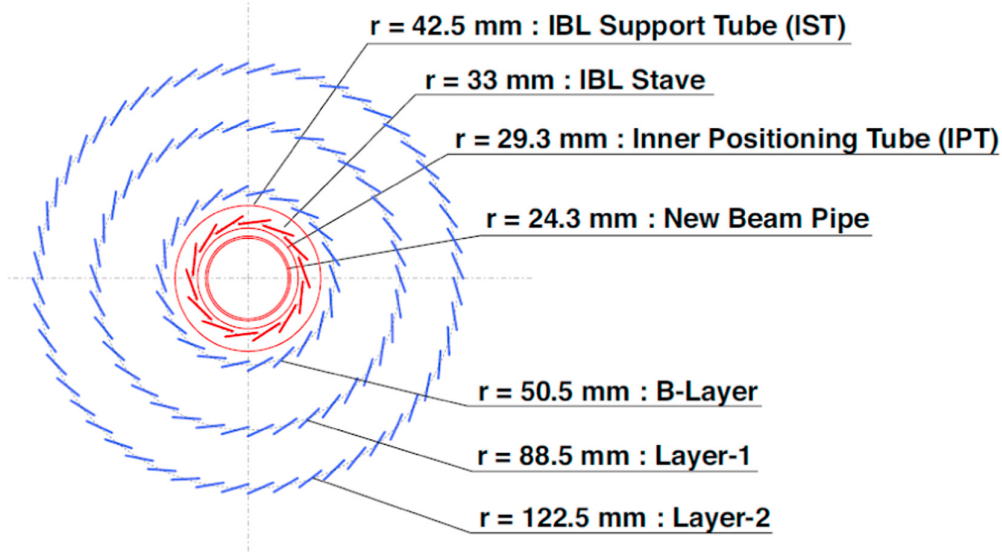


Figure 2.14: Transverse view of the barrel section of the pixel detector, showing the innermost layer, the Insertable B-Layer (IBL), and its support structure (red) as well as the three surrounding layers (blue). From Ref. [48].

$17\ \mu m$ in $(r - \phi)$ and $580\ \mu m$ along z .

The Transition Radiation Tracker

The outermost layer of the ATLAS ID, surrounding the SCT, is the transition radiation tracker (TRT). The TRT is a tracking volume designed around the proportional drift tube concept and is composed of polyimide drift tubes (straws) that are 4 mm in diameter. The barrel section of the TRT contains up to 73 layers of 144 cm-long straws aligned parallel to the beam-pipe while the end-cap section has 160 straw planes composed of 37 cm long straws arranged radially into wheels (see Figure 2.12). Each straw of the TRT has a $31\ \mu m$ -width gold-coated wire at its center which acts as anode and is grounded, while the inner walls of each straw are kept at a potential of approximately -1.5 kV . A track hit in a given straw is the result of the 70% Xe – 27% CO₂ – 3% O₂ gas mixture contained in the straw volume being ionised and the resulting electrons (ions) drifting to the center wire (inner wall) of the straw. The induced current from the drifting charge is converted to an electrical signal and read out.

On average, a single charged-particle track leaves 36 hits in the TRT. The TRT only provides $(r - \phi)$ information (no z information), for which it has a per-straw hit resolution of $130\ \mu m$. The relatively poor hit resolution, when compared to the silicon based tracking detectors, is compensated by the large number of hits per track which lead to very long measured track lengths as compared to the pixel and SCT detectors. Additionally, the straws are embedded in and individually separated by a polypropylene fiber which induces transition-radiation photons to be produced. The amount and pattern of transition radiation depends on the mass of the passing particle: the passage of an electron will produce significantly more transition radiation than heavier charged particles, such as the copiously-produced pion. Information provided by the TRT therefore provides additional discrimination power between electrons and pions and enhances the performance of ATLAS' electron identification algorithms that primarily depend on information coming from the calorimeter systems (Section 2.2.3).

2.2.3 Calorimeter Systems

The ATLAS calorimeter systems are situated outside of the ID and central solenoid and are tasked with the measurement and containment of showers from electrically charged and neutral particles. A view of the calorimeter systems is provided by Figure 2.15. Broadly speaking, there are two types of calorimeters based on their purpose: electromagnetic and hadronic calorimeters. The electromagnetic calorimeter system has η coverage that matches the inner-detector and is optimized for precision measurements of electrons and photons. The hadronic calorimeter system has readout cells that are generally of coarser granularity as compared to the electromagnetic calorimeter and is designed to meet the requirements for jet and missing transverse momentum measurements. Besides classification by physics purpose, the calorimeter system can also be broken into two classes based on detector technology: either based on gaps of cooled liquid-argon [49] or on scintillating tiles as the active media [50].

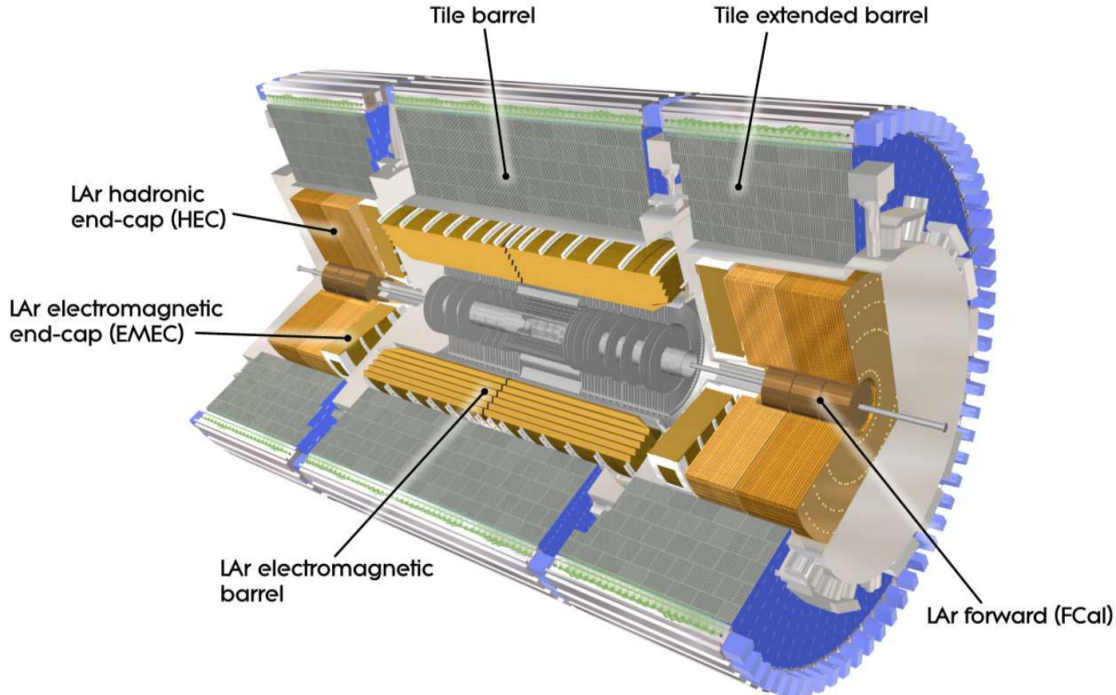


Figure 2.15: Cut-away view of the ATLAS calorimeter system, with liquid-argon and scintillating-tile subsystems indicated.

Electromagnetic Calorimeter

The electromagnetic (EM) calorimeter is a high-granularity lead/liquid-argon (LAr) sampling calorimeter situated outside of the ID and sharing the same cryostat as the the central solenoid. It consists of barrel and end-cap sections that cover the entire range within $|\eta| < 3.2$ and is illustrated in Figure 2.15. The structures of the electromagnetic barrel and end-cap calorimeters are shown in Figure 2.16. The EM calorimeter is designed in an accordian type structure to provide full coverage in ϕ . The cooled LAr fills the gaps between layers of the accordian structure. Passing particles from the interaction point undergo scattering and bremsstrahlung processes as they pass through the lead absorbers. The resulting electrons and photons ionise the LAr, producing drift electrons and ions whose signals are read out by the interleaved readout electrodes. The 2.1 mm drift gap has an operating voltage of $\approx 2\text{ kV}$. The electromagnetic calorimeter is > 22 radiation lengths (X_0), ensuring that the majority of electrons and photons are completely contained within the EM calorimeter. The majority of the EM energy, amounting to approximately $16 X_0$, is contained within the second sampling layer (see Figure 2.16). The fine granularity of the readout, indicated in Figure 2.16, was designed with the ability to distinguish individual photons arising from $\pi^0 \rightarrow \gamma\gamma$ decays. The ability to distinguish photons pairs so precisely is also important for the main Higgs boson decay channel used for its discovery, $h \rightarrow \gamma\gamma$.

In the region $|\eta| < 1.8$, a so-called *presampler* detector is used to correct for the energy lost by

electrons and photons due to material interactions occurring upstream of the EM calorimeter. It is a single LAr layer, with width 1.1 cm (0.5 cm) in the barrel (end-cap).

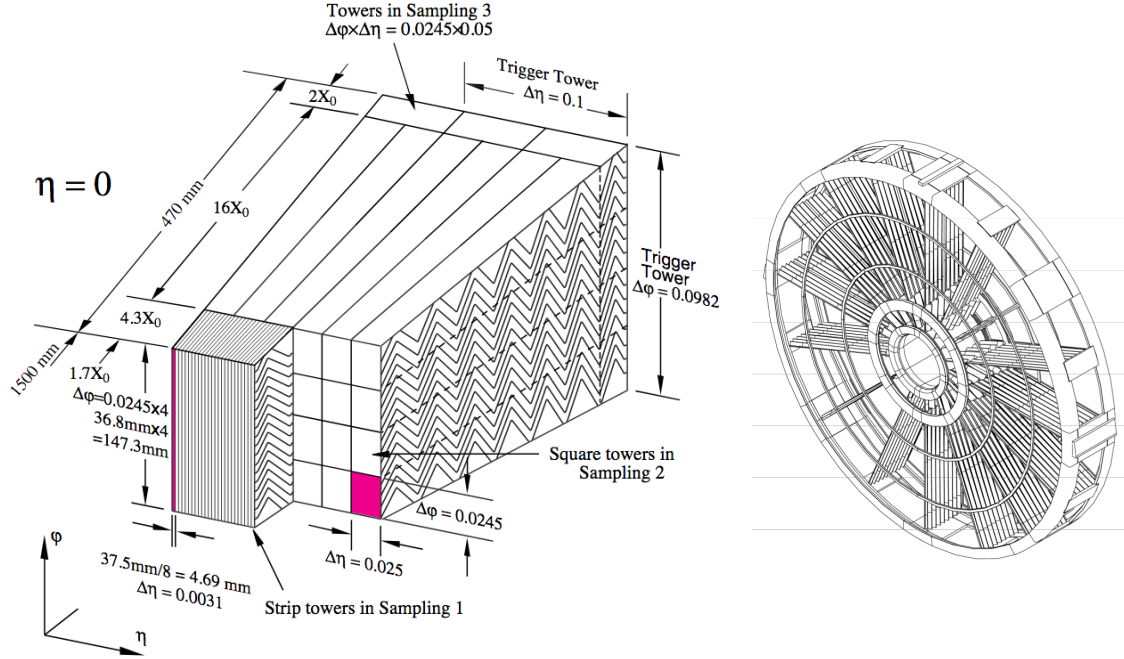


Figure 2.16: *Left:* Cut-away view of the barrel electromagnetic calorimeter and its accordian structure. Indicated are the geometry and absorption properties of the three sampling layers. Also indicated is the granularity of the electrode readout in $\Delta\phi \times \Delta\eta$ in each layer. *Right:* Diagram of the electromagnetic end-cap calorimeter accordian wheel structure (only a sub-set of the accordian structure is shown).

Hadronic Calorimeter

The barrel section of the hadronic calorimeter is composed of a lead/scintillating-tile type detector whereas the end-cap hadronic calorimeter is based on copper/LAr-based technology.

The lead/scintillating-tile calorimeter (the ‘tile calorimeter’) is located just beyond the EM calorimeter. It is composed of a barrel section, covering $|\eta| < 1.0$, and two extended barrels that cover $0.8 < |\eta| < 1.7$ (see Figure 2.15). It is a sampling calorimeter using steel as the passive absorber and scintillating plastic tiles as the active media. The tile calorimeter is composed of modules in which the scintillating tiles are situated in $(r - \phi)$ within the steel absorbers, as shown in Figure 2.17. The detector is segmented radially into three layers and the readout of the scintillation light, using wavelength-shifting fibers that are fed into photomultiplier tubes (PMT) situated along the outer radii, is organized in a projective geometry, also illustrated in Figure 2.17. In the barrel (extended barrel) section, most of the hadronic energy is captured by the first (last) two layers which account for ≈ 5.5 (6) hadronic interaction lengths (λ) of the ≈ 7 in total.

The hadronic end-cap (HEC) calorimeter consists of two wheels per end-cap, situated behind the electromagnetic end-cap calorimeter, and provides calorimetric coverage in the range $1.5 < |\eta| < 3.2$. A view of the HEC can be seen in Figures 2.15 and 2.18. The HEC calorimeter is built from layers of copper plates interleaved with 8.5 mm LAr gaps which provide the active medium for this sampling calorimeter. The readout structure is obtained by dividing the gaps into separate drift zones for which there are dedicated readout electrodes. This readout structure is arranged in a projective geometry.

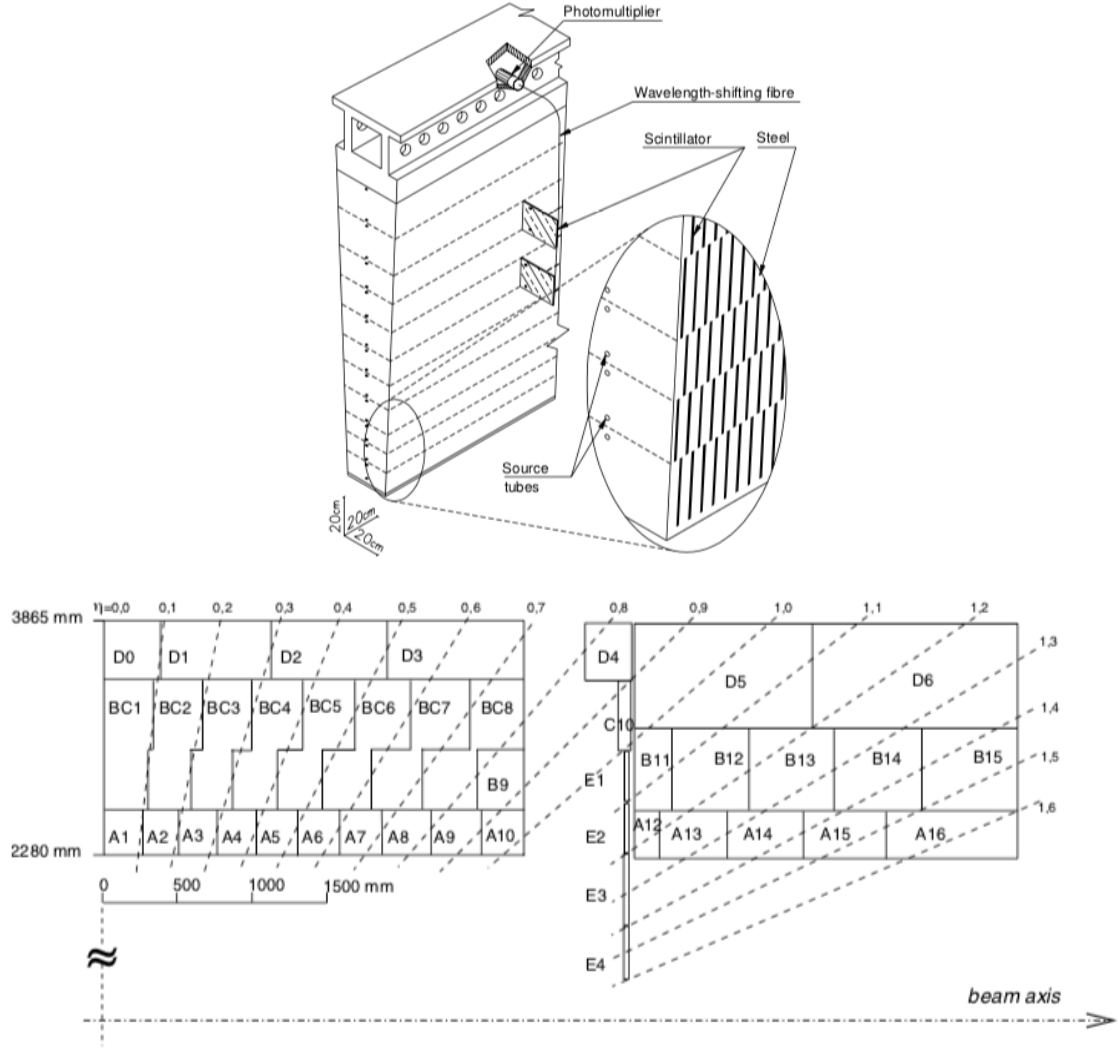


Figure 2.17: *Top:* A view of a tile calorimeter module with its interleaved steel absorbers and scintillating tiles and PMT readout. Also indicated are the source tubes through which radioactive Cesium (Cs) sources are passed for calibration purposes [51]. *Bottom:* Illustration of the segmentation of the projective readout of both the barrel and extended barrel tile calorimeter.

Forward Calorimeter

The forward calorimeter (FCal) system [52] provides calorimetric coverage to high $|\eta|$, between $3.1 < |\eta| < 4.9$, furthering the hermeticity of the detector. As indicated in Figure 2.18, FCal consists of three layers in the z direction: an electromagnetic layer (FCal 1) and two hadronic layers (FCal 2 and FCal 3). All three layers use LAr as the active medium but differ in their passive media. FCal 1 uses copper for its absorber, chosen for its heat removal properties, while FCal 2 and FCal 3 use tungsten, chosen to provide high containment and minimisation of the lateral spread of hadronic showers. The FCal modules consist of matrices of the passive material with regularly spaced readout tubes oriented parallel to the beam-pipe that are filled with the cooled LAr.

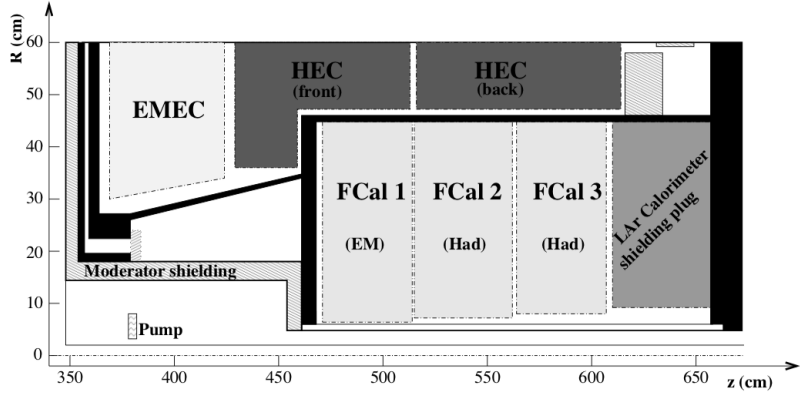


Figure 2.18: View of the forward calorimeter (FCal) system. Portions of the electromagnetic and hadronic end-cap systems are also shown.

2.2.4 The Muon Spectrometer

Surrounding the calorimeters is the muon spectrometer (MS) [53], responsible for the detection of high-momentum, minimum-ionizing muons originating from the pp interaction. The MS is based on the magnetic deflection of muon tracks, allowing for their momentum determination. The bending of the muon trajectories is provided by the large superconducting air-core toroid magnet system, illustrated in Figure 2.10, consisting of a large barrel toroid over the range $|\eta| < 1.4$ and end-cap toroid systems in the range $1.6 < |\eta| < 2.7$. The superconducting toroid magnet provides an average field of 4 T. The magnetic field bending strength is roughly constant in η , except in the region in which the transition between the barrel and end-cap toroids takes place ($1.4 < |\eta| < 1.6$). A view of the ATLAS detector is shown in Figure 2.19, where it can be seen that the volume enclosed by the MS takes up most of the available volume outside of the calorimeter systems in the underground experimental cavern at Point 1. It should be noted that the overall design of the superconducting toroid structure, dictated by the performance requirements of the MS, is what gives ATLAS its large size and essentially drove the original design of all subdetectors discussed in

the previous sections.

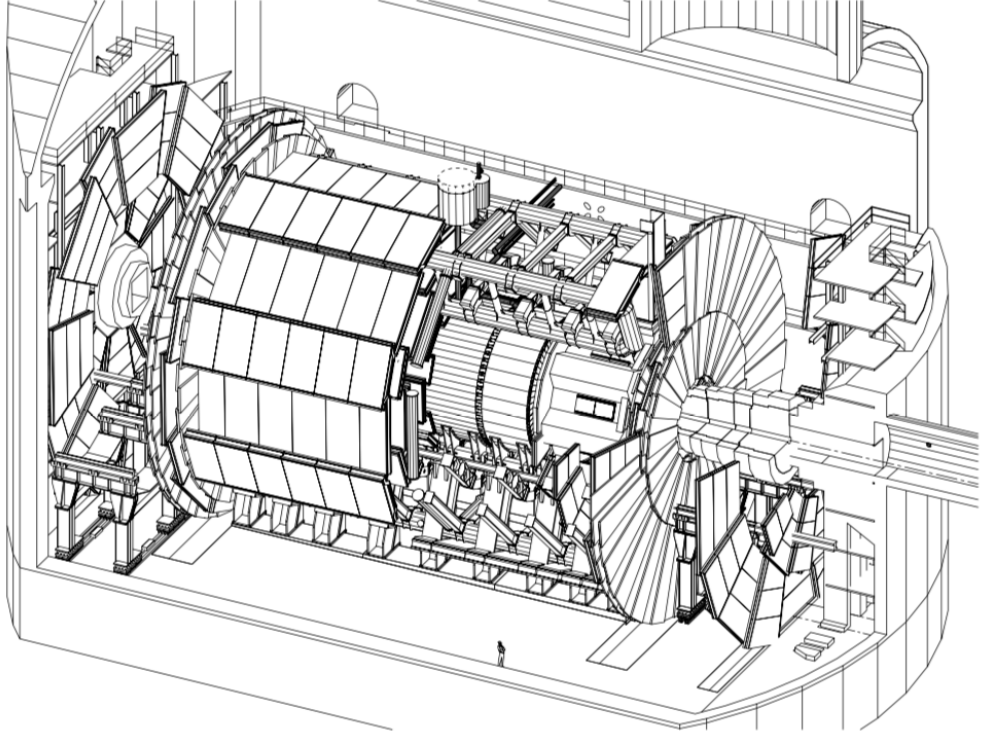


Figure 2.19: A view of the ATLAS detector inside the underground experimental area UX15. The cut-away view exposes the toroid structure and calorimeter system. Notice that the outermost muon stations in the forward regions are located at the extreme ends of the cavern.

There are four types of gaseous radiation detector used in the MS, and their chamber layout is based on the concept of projective towers. The chambers follow the structure of the toroid magnet structure and have a 16-fold segmentation in azimuth, shown in Figure 2.20. They are arranged in large and small sectors, with the large sectors covering the regions between the coils of the toroid and the small sectors the azimuthal range in which the coils sit. The detector types can be broken into two classes and are either *precision* or *trigger* chambers. The precision chambers are composed of Monitored Drift Tube (MDT) [54] and Cathode Strip Chamber (CSC) [55] detectors and allow for the precise measurement the muon tracks as they traverse the MS, specifically the precise measurement in the bending plane of these tracks so as to allow for accurate determination of the muon momenta through their curvature. The trigger chambers are composed of Resistive Plate Chamber (RPC) [56] and Thin Gap Chamber (TGC) [57] detectors and have fast signal formation and readout times, allowing for accurate assignment of a passing muon to a specific pp bunch crossing. Both types of detectors exist in the barrel and end-cap sections of the MS and there are typically at least three layers of precision-type chambers over the entire $|\eta|$ range of the MS in order to allow for the sagitta measurement of the muon tracks necessary for momentum determination. The number of precision chamber hits over the entire range in $\eta - \phi$ of the MS is

shown on the left side of Figure 2.21. In the regions $|\eta| \sim 0$ and $|\eta| \sim 1.2$ there are noticeable drops in chamber coverage in order to allow for ID and calorimeter services and in the transition region between the barrel and end-cap, respectively, as seen on the right side of Figure 2.21.

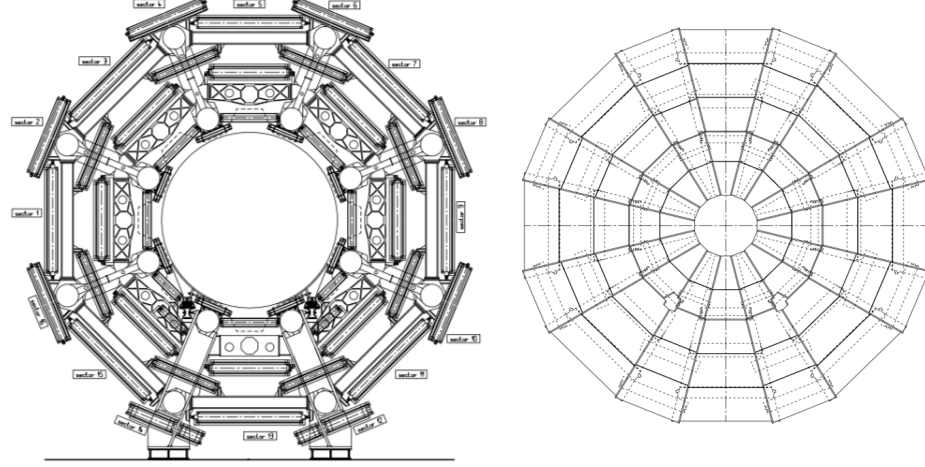


Figure 2.20: View of the 16-fold segmentation of the muon spectrometer in the barrel (*left*) and end-cap (*right*). Clearly seen in both is the arrangement of the detector chambers into large and small sectors, allowing for complete coverage in azimuth. The view of the end-cap is that only of the MDT chambers located at $z \approx 13$ m.

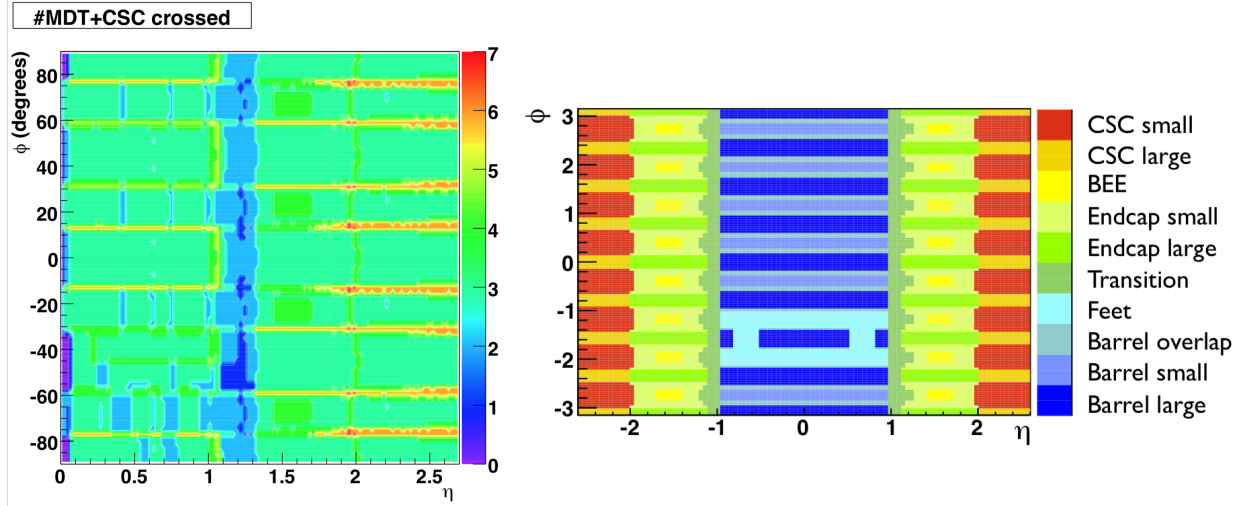


Figure 2.21: *Left:* Number of precision muon chambers (MDT and CSC) traversed by a muon passing through the muon spectrometer as a function of η and ϕ . The regions of high numbers of crossings (> 4) correspond to the regions of overlap between the large and small sectors. *Right:* Location in $\eta - \phi$ of several regions of the MS.

The layout of the muon chambers and the corresponding detector technologies in the barrel and end-cap sections is shown in Figure 2.22. Here we will briefly describe each, starting with those in

the barrel section.

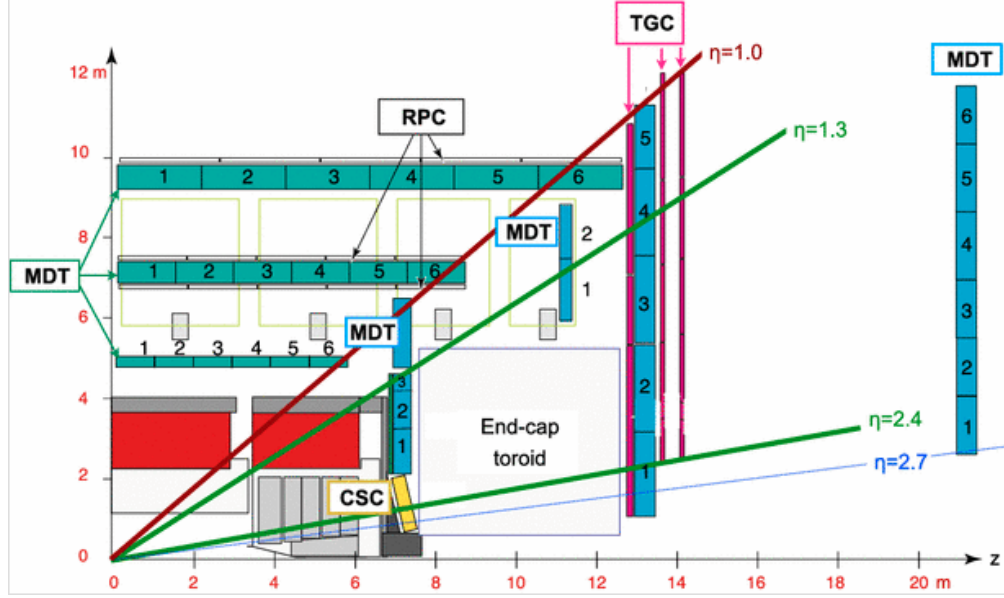


Figure 2.22: A view in the $r - z$ plane of a quadrant of the muon spectrometer (MS). Indicated by color are the four detector technologies used in the MS: MDT (blue), RPC (grey), TGC (red), and CSC (yellow). The light grey boxes at $6 < r < 9$ m indicate the location of the barrel toroid structures. Also shown are the envelopes in $|\eta|$ of the barrel, small wheel, and big wheel sections of the MS.

Muon Spectrometer: Barrel

The muon chambers in the barrel section of the MS are rectangular in shape and arranged in 3 cylindrical shells, concentric about and parallel to the beam-axis at radial distances of 5, 7.5, and 10.5 m (see Figure 2.20). The precision chambers in the barrel section are composed of MDT chambers with tubes perpendicular to the beam-axis and parallel to the toroidal magnetic field, allowing for precision measurement along η . The MDT tubes are 3 cm in diameter and contain a 93% Ar – 7% CO₂ gas mixture with a single tungsten-rhenium wire operated at 3 kV. Traversal of a minimum ionising particle (MIP) ionises the gas within the tube, and the signal of the resulting ionisation charge is read out. The typical spatial resolution of a single MDT tube is below 100 μm . The MDT chambers are built as multi-layers of many MDT tubes which allows for the improvement of the spatial resolution down to 50 μm when the information from the individual layers is combined. An MDT double multi-layer chamber is shown in Figure 2.23. Also illustrated in this figure is the principle by which the tube hits in a given MDT multi-layer are used to form tracklets which aid in the process of muon track-building.

The chambers responsible for constructing muon trigger primitives in the MS barrel are the RPC chambers, whose principle of operation is shown on the left of Figure 2.25. The RPC gap is 2 mm, filled with tetrafluorethane (C₂H₂F₄), and is lined with parallel plate electrodes operated at

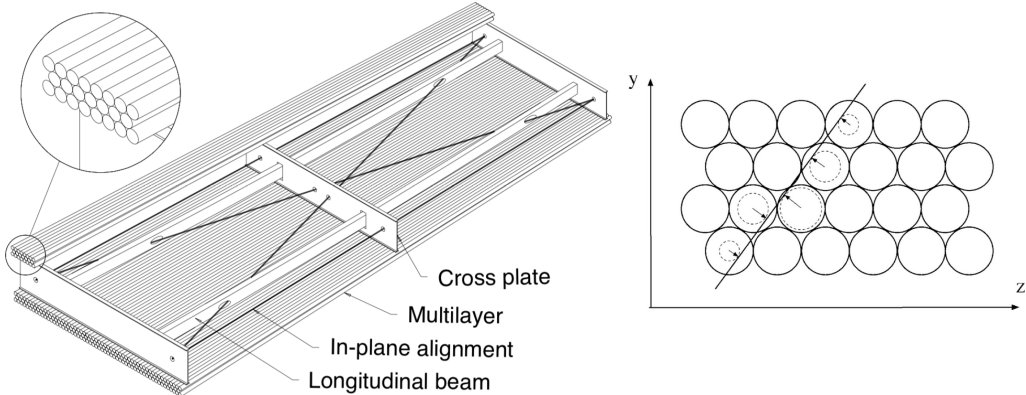


Figure 2.23: *Left*: Illustration of a double-multilayer MDT chamber with its internal alignment and support structure exposed. A zoom-in on the multilayer of MDT tubes is shown. *Right*: Illustration of the multilayer MDT tracklet-fitting algorithm [58].

a potential difference of 9.8 kV. This high operating potential and gas mixture allows for a timing resolution of 2 ns. Readout strips in x and y collect the induced charge from the ionisation events within the gap and provide additional spatial information for track and trigger-primitive building.

Muon Spectrometer: End-cap

The end-cap muon chambers, located in $1 < |\eta| < 2.7$, are arranged in 4 rings — *wheels* — extending radially and concentric with the beam axis at $z \approx 7.5, 10, 14, 22$ m from the pp interaction point. The wheel at $z \approx 7.5$ m, located on the IP-side of the end-cap toroid, is referred to as the ‘Small Wheel’ and those at $z > 10$ m are referred to as the ‘Big Wheels’. That at $z \approx 10$ m, situated above the end-cap toroid, is an intermediate muon station composed of MDT chambers and has generally lower coverage than the Small and Big Wheels.

As in the barrel section, the primary precision measurement in the end-caps is provided by MDT chambers which are located in all four wheels of the end-cap. The MDT tubes are oriented azimuthally in order to obtain precision measurement in η . At the region $2 < |\eta| < 2.7$, in the innermost muon station in the end-cap that experiences the highest background rates, the precision muon measurement is provided by the CSC chambers at low radii. The CSC detectors are multi-wire proportional chambers, illustrated in Figure 2.24, with cathode strips perpendicular to anode wires and operated with Ar/CO₂/CF₄ gas mixtures. Passing MIPs result in ionisation events whose signals along the strips and wires are subsequently readout. As compared to the MDT chambers, the CSC detectors can resolve spatial information in both η and ϕ and, due to their relatively high granularity readout structure, can sustain the higher background rates experienced in this very forward region of the detector. The CSC sectors are multi-layered (4-layers) and can achieve spatial hit resolutions on the order of 60 μ m.

The trigger chambers in the end-cap are composed of the TGC detectors. Like the CSC, the

TGC is a multi-wire proportional chamber with a gas mixture of CO_2 and n -pentane ($n\text{-C}_5\text{H}_{12}$). An illustration of the operating principles of a TGC detector is shown in Figure 2.25. The graphite cathodes and wires, with 1.4 mm separation, are held at a potential difference of 2.9 kV. This high potential difference and anode/cathode geometry allows for signals to be readout with a timing resolution of 4 ns. The signals from the drift electrons, collected along the wires, and the induced charge on the strips located behind the G-10 layer are read out and provide two-dimensional spatial information that can be used both in track and trigger-primitive building.

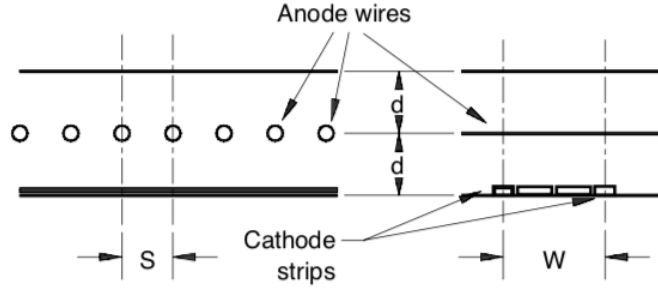


Figure 2.24: Diagram showing the main components of a cathode-strip chamber (CSC). On the left (right) is a view parallel (perpendicular) to the anode wires and perpendicular (parallel) to the cathode strips.

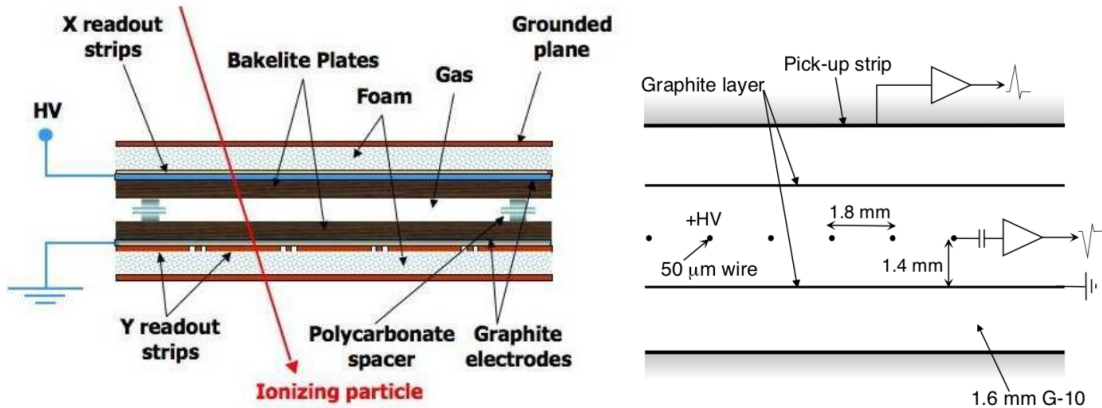


Figure 2.25: Muon trigger chambers. *Left:* Illustration of a resistive plate chamber (RPC) and its principle of operation. *Right:* Diagram showing the main components of a thin-gap chamber (TGC).

2.2.5 Trigger and Data Acquisition

During Run-II operation between 2015–2018, the LHC delivered pp collisions to ATLAS at instantaneous luminosities of $10^{34} \text{ cm}^{-2}\text{s}^{-1}$, at a bunch spacing of 25 ns, giving 33.7 pp interactions per

bunch crossing on average (see Figure 2.7). These values correspond to roughly 10^9 pp interactions per second. It is not possible for the ATLAS detector and data storage facilities to both respond to and record every one of these interactions. In fact, from a physics perspective it is not necessarily desirable to record every single interaction. The vast majority of such interactions arise from uninteresting, soft collision processes which are not likely to contain, for example, decays of Higgs bosons or of new particles not accounted for in the SM. For this reason, the ATLAS detector employs an *online*¹² selection strategy to select potentially interesting candidate events to be further processed and considered for permanent storage. This online selection strategy is referred to as the *trigger* system [59].

The ATLAS Run-II trigger system consists of two levels: a hardware-based low-level trigger, referred to as the *Level-1* (L1) trigger, and a second level software-based high-level trigger (HLT) [60]. The L1 trigger uses relatively coarse-grained measurements from the calorimeters and MS. It performs the first level of selection, reducing the initial input 40 MHz rate of events by accepting events at a maximal rate of 100 kHz. The L1 trigger performs searches for coarse proxies of interesting physics objects: leptons, photons, and jets. It triggers on electrons and photons based on energy deposits in the EM calorimeter, limited to $|\eta| < 2.5$. The hadronic calorimeter provides jet candidates to the L1 trigger system via calorimeter ‘towers’ made up of trigger elements constructed by a sliding window algorithm. Each trigger element is constructed by calculating energy sums of calorimeter cells in $\eta - \phi$. Muon-based L1 triggers are based on coincidences of hits along the layers of the MS that form projective towers, or *roads*, consistent with high- p_T muons.

The candidate events selected by the L1 trigger system are forwarded to the HLT. The HLT system is composed of a Level 2 (L2) trigger and the event filter (EF). The L2 system is similar to the L1 trigger, but performs more refined measurements on the objects and regions of the detector that resulted in the initial L1 trigger’s decision to accept the event. The EF is purely software based, using the ATLAS Athena reconstruction framework [61] to perform high level object reconstruction and identification using algorithms similar to those used in the offline environment ([Section XXX](#)). The HLT accept rate is roughly 1 kHz. The accepted events are sent to CERN’s permanent storage facilities and are made ready for the offline analysis. An overview of the trigger system is shown in Figure 2.26.

¹²The ‘online’ environment refers to that of the ATLAS detector during runtime. The ‘offline’ environment refers to anytime in which the data being inspected or analysed is not *at that time* being recorded by ATLAS but instead has already been stored to permanent storage and is readily accessible at any time.

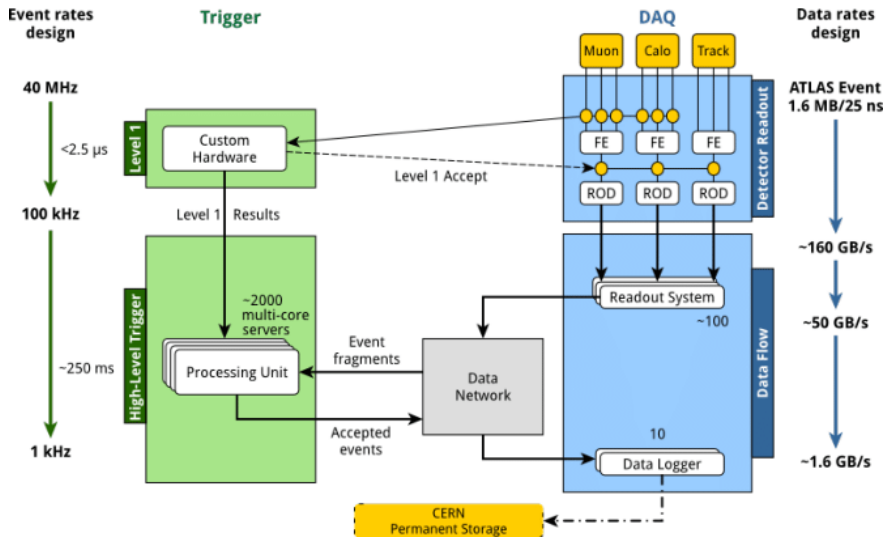


Figure 2.26: Overview of the ATLAS Run-II trigger and data-acquisition architecture. Data from the muon and calorimeter systems are used for the Level 1 (L1) trigger, reducing the input event rate from 40 MHz to 100 kHz. The data accepted by the L1 trigger are forwarded to the readout drivers (RODs) [59] which, among other things, re-shuffle the raw data into the standardized ATLAS event format [62]. The events selected by the HLT at a rate of 1 kHz are pulled from the RODs and then forwarded to the permanent storage. Figure taken from Ref. [60].

Chapter 3

Physics Building Blocks and their Reconstruction

If you can put your five fingers through it it is a gate, if not a door.

—Stephen Dedalus, in James Joyce’s *Ulysses*

In order to convert the multitude of electrical signals read out by the subdetectors of ATLAS as a result of a successful trigger (c.f. Section 2.2.5) into well-defined and meaningful representations of the underlying physics process that initiated them, at the level required for performing high-quality physics analysis, several steps of reconstruction and identification must take place. The physics analyses presented in the current work involve the use of leptons, jets, and the so-called missing transverse momentum, $\mathbf{p}_T^{\text{miss}}$. The methods used to deduce the presence of these objects within the ATLAS detector will be discussed in this chapter. Section 3.1 introduces the reconstruction of charged-particle tracks and pp interaction vertices within the ID, both of which are used as low-level seeds or inputs to the reconstruction of the high-level physics objects to be discussed in the subsequent sections. Section 3.2 goes on to discuss the reconstruction of the charged leptons relevant to the current work: electrons and muons. Sections 3.3 and 3.3.3 describe the reconstruction of jet objects and the identification of jets arising from the decay of heavy-flavor hadrons, respectively. Section 3.4 then goes on to describe the reconstruction of $\mathbf{p}_T^{\text{miss}}$, which relies on an accurate description of leptons and jets. The methods used for reconstructing the leptons and jets are not one hundred percent accurate: detector information arising due to an electron may leave signatures similar to those of a jet, for example, and thus spoil their unambiguous description. Where relevant, in the following we will discuss the methods by which the reconstruction and identification of the physics objects is made more precise and how high levels of confidence about their actual presence within the detector are achieved. Section ?? will also introduce the notion of high-level object ambiguity resolution through the use of so-called *overlap removal* procedures.

3.1 Charged-Particle Tracks and Primary Vertices

The reconstruction of charged-particle tracks (“tracking”) and primary interaction vertices (“vertexing”) is based on information provided by the ID, primarily by the pixel and SCT subdetectors [63, 64, 65, 66, 67]. Charged-particles produced in pp collisions will leave signals — *hits* — on the different layers of the ID. The aim of tracking is to translate these layer hits into *spacepoints* which are then combined to form a track following the particle’s traversal through the ID. Given its highly granular readout, the pixel detector provides three dimensional spacepoints from each layer hit while the back-to-back readout strips on each layer of the SCT must be combined, using the stereo-angle information from the second set of strips, to give three dimensional spacepoint information. The hit information provided by the TRT straws is two-dimensional in nature, providing only $r - \phi$ information in the barrel section and $\phi - z$ information in the end-caps.

Within the solenoidal magnetic field of the ID, charged-particle tracks follow helical trajectories in the plane transverse to the beam-pipe (xy -plane) and can be fully characterised by five *track (perigee) parameters*:

$$(d_0, z_0, \phi, \theta, q/p), \quad (3.1)$$

where d_0 (z_0) is the transverse (longitudinal) impact parameter, ϕ and θ are the azimuthal and polar coordinate, respectively, of the track at the point at which d_0 and z_0 are defined, q/p is the ratio of the particle charge to the magnitude of its momentum. The charge of a track is determined by its curvature within the magnetic field. The track parameters are defined with respect to their associated primary vertex, whose reconstruction will be described shortly. An illustration describing the track parameters is provided by Figure 3.1.

The primary track reconstruction algorithm used in ATLAS follows an *inside-out* pattern recognition procedure and first starts with information provided by track *seeds*, composed of a few spacepoints, in the silicon detectors which then are extended outwards into the TRT [63]. The inside-out approach accounts for the majority of tracks reconstructed in ATLAS but it is complemented by an *outside-in* approach that starts with the TRT hits and moves inwards [63]. This latter approach is useful in recovering those tracks with ambiguous or missing inner-layer pixel hits; for example, in the case of photon conversions or long-lived neutral particle decays.

The collection of reconstructed tracks is used as input to the primary vertex reconstruction. Primary vertex reconstruction follows a so-called *adaptive vertex fitting* (AVF) [65, 67] procedure and occurs in two steps: primary vertex finding, in which tracks are associated to a particular vertex candidate, and vertex fitting, which involves the reconstruction of the actual vertex position and its errors. After the vertex fitting stage, the tracks associated with a given vertex are refit with the constraint of the vertex position and its errors. The track refitting can update the track parameters (Eqn. 3.1) associated with the tracks. Only vertices with at least two charged particle tracks with $p_T > 400$ MeV are considered.

In the high luminosity collisions at the LHC there will generally be multiple primary vertices

associated with each pp bunch crossing. A physics *event* in ATLAS, then, is chosen as the set of processes originating from the pp interaction associated with the *hardest* primary vertex — the *primary hard-scatter vertex* — taken as that primary vertex with the highest sum of squared p_T of tracks originating from that vertex. The subsequent event reconstruction takes place around the primary hard-scatter vertex and only those objects originating from it are taken as relevant when reconstructing the physics objects in the event. Any additional primary vertices are considered as *pileup vertices*.

The presence of so-called *secondary*, *tertiary*, and so on..., vertices are also important and will be described in Section 3.3.3.

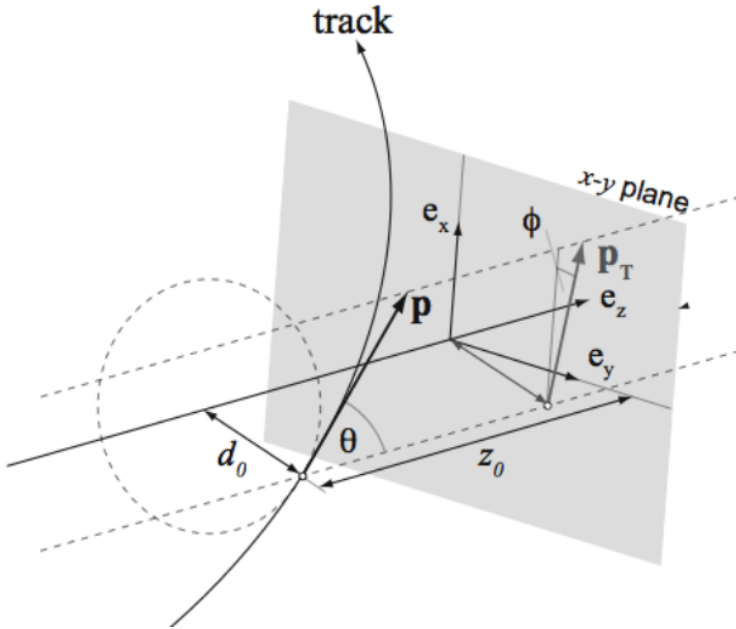


Figure 3.1: Illustration of the relationship between the track parameters and associated track. In this scenario, the hard scatter primary vertex is located at $(e_x, e_y, e_z) = (0, 0, 0)$, though this is not generally the case.

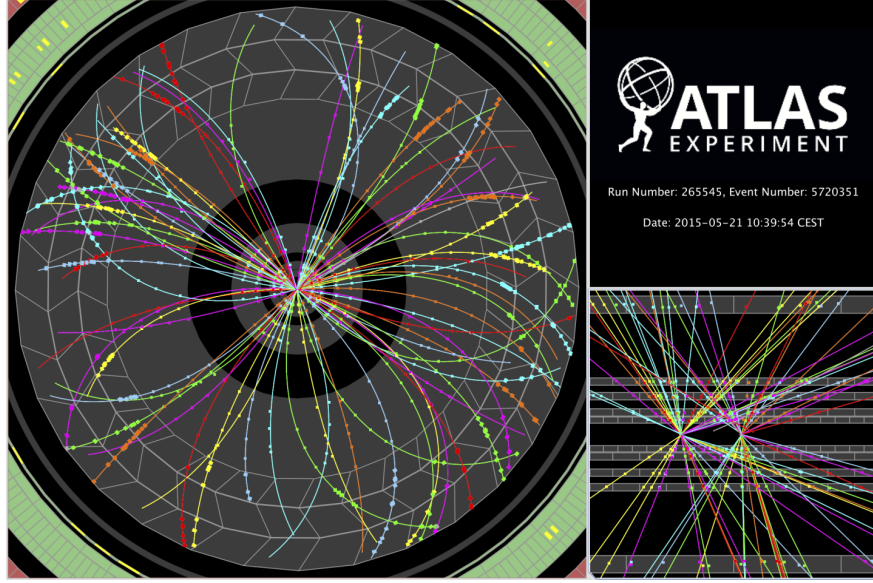


Figure 3.2: Event display of a low-pileup event recorded at the start of Run-II, in early 2015. *Left:* Transverse view of the ID. Seen in color are the reconstructed tracks traversing the inner layers of the pixel detector, SCT, and TRT. The colored dots are all reconstructed spacepoints used as input to the track fitting procedure. *Right, lower:* View in $r - z$ of the same pp bunch-crossing event as on the left. Two reconstructed primary vertices are clearly observed. On average, in Run-II there were roughly 30 primary vertices reconstructed per event, with up to ≈ 65 occurring at maximum.

3.2 Electrons and Muons

Electrons and muons, being charged particles, leave identifiable tracks within the ID. As a result, their reconstruction involves the use of the tracks and vertices described in the previous section, using them essentially as initial seeds for their complete reconstruction. Electron reconstruction, described in Section 3.2.1, complements the track information provided by the ID with calorimetric information provided by the EM calorimeter (Section 2.2.3) and with knowledge about the pattern of transition radiation expected to occur in the TRT as a result of passing electrons. Muon reconstruction, described in Section 3.2.2, revolves around stitching together the tracks reconstructed in the ID with those tracks independently reconstructed in the MS layers at large radii.

3.2.1 Electrons

Electron Reconstruction

After 2016 they replaced sliding window algorithm with supercluster-based reco

The reconstruction of electron candidates is based on three components which characterise the signature of electrons: localised clusters of energy deposits found within the EM calorimeter, charged-particle tracks identified in the ID, close-matching (in (η, ϕ)) of the tracks to the clusters that form the final electron candidates [68]. It is generally possible to match multiple tracks

to the same electromagnetic cluster, all originating from the same primary electron produced in the hard-scatter. This is due to the fact that electrons lose significant amounts of energy to bremsstrahlung photons as they interact with and traverse the ID. These radiated photons can then undergo conversion to electron-positron pairs, which, too, can undergo further bremsstrahlung. The positrons, electrons, and photons are usually emitted in a very collimated fashion and thus deposit most of their energy in a localised fashion within the calorimeter.

The search for localised energy deposits in the EM calorimeter is performed by following a sliding window algorithm over the individual cells whose dimensions are defined by the second sampling layer of the EM calorimeter (Figure 2.16). Electron candidates are seeded by localised energy deposits whose summed transverse energy, across all layers of the EM calorimeter, is greater than 2.5 GeV [68]. These clusters act as seeds for the matching of reconstructed ID tracks. The reconstructed tracks are refit using a Gaussian Sum Filter (GSF) method [69] that accurately accounts for the bremsstrahlung energy losses characteristic of electron traversal and are then matched to the localised clusters using the cluster barycenter as the point of reference to match in $\eta - \phi$. If there is no GSF-track candidate matching to the EM calorimeter cluster seed, then the cluster is marked as an unconverted photon. The cluster is marked as a converted photon if a matched GSF-track candidate exists but is not associated with the primary hard-scatter vertex.

Electron Identification

Once electron candidates are reconstructed, they are selected based on various levels of identification. A further set of identification criteria is required on top of the reconstruction so as to improve the selection of true electrons originating from the primary hard-scatter vertex — so-called *prompt* electrons — over *non-prompt* sources of reconstructed electrons such as those originating from photon conversions or the misidentification of charged pions that leave electron-like tracks in the ID. This identification criteria is based on the construction of a multivariate likelihood (LH) and is referred to as the *electron likelihood identification*. The inputs to the LH are listed in Table 3.1 and include measurements from the tracking system in the ID, calorimetric information, and quantities that combine the tracking and calorimetric information [68].

The electron LH is based on the products for the signal and background probability density functions (PDFs) associated with the set of inputs in Table 3.1:

$$L_{S(B)}(\mathbf{x}) = \prod_{i=1}^n P_{S(B),i}(x_i), \quad (3.2)$$

where \mathbf{x} is the vector of quantities listed in Table 3.1 and the $P_{S(B),i}(x_i)$ are the values of the PDF for quantity i at value x_i for the signal (S) and background (B). The likelihoods are built using simulation and the signal is composed of samples of prompt electrons and the background is built from a combination of jets that mimic the signature of prompt electrons, electrons from photon conversions, and non-prompt electrons from the decay of hadrons containing heavy-flavours [68].

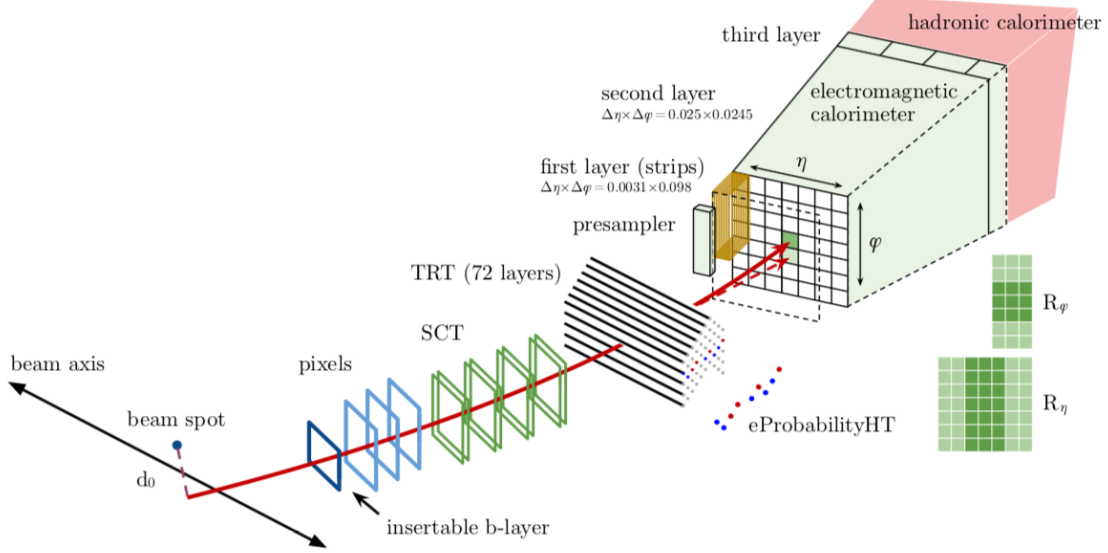


Figure 3.3

The final electron LH discriminant, shown in Figure 3.4, is based on a transformed version of the ratio,

$$d_L = \frac{L_S}{L_S + L_B}, \quad (3.3)$$

where the transformation acts to spread d_L to values not bounded by 0 and 1, motivated by the need to have well-defined working points based on selections on d_L .

There are four such fixed values of the final LH discriminant that are used to define four working points corresponding to increasing thresholds on the final LH discriminant: **VERYLOOSE**, **LOOSE**, **MEDIUM**, and **TIGHT**. The efficiencies to identify prompt electron candidates are measured using samples of $Z \rightarrow ee$ and $J/\psi \rightarrow ee$ following a tag-and-probe approach. They are found, for electron candidates with $E_T > 40$ GeV, to be 93%, 88%, and 80% for the **LOOSE**, **MEDIUM**, and **TIGHT** working points, respectively [68].

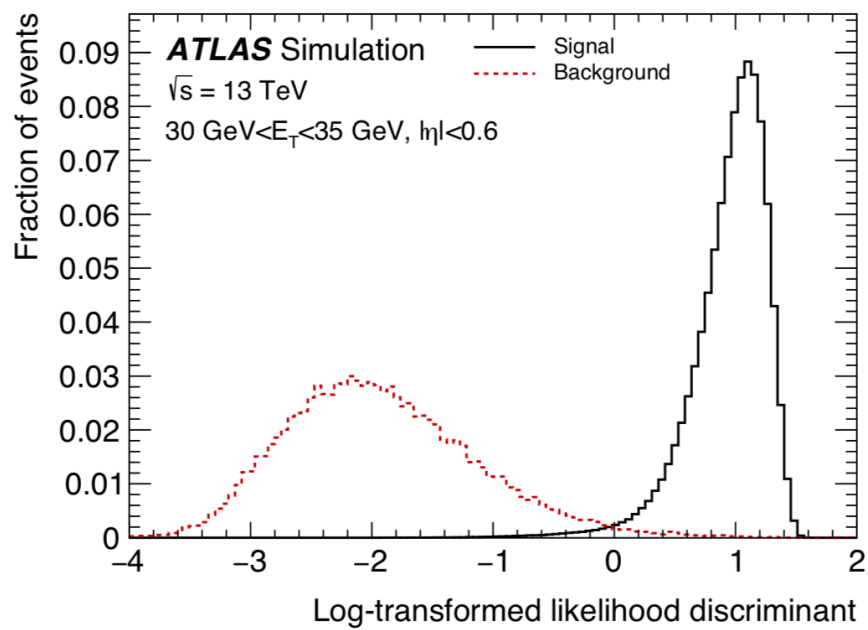


Figure 3.4: Transformed LH-based electron identification discriminant for electron candidates with $30 \text{ GeV} < E_T < 35 \text{ GeV}$ and $|\eta| < 0.6$. From Ref. [68].

Table 3.1: From Ref. [68].

Input Type	Name	Description
Hadronic Leakage	$R_{\text{had}1}$	Ratio of E_T in the first layer of the hadronic calorimeter to E_T of the EM cluster
	R_{had}	Ratio of E_T in the hadronic calorimeter to E_T of the EM cluster
Third layer of EM calorimeter	f_3	Ratio of the energy in the third layer to the total energy in the EM calorimeter. Only used for $E_T < 30 \text{ GeV}$ and $ \eta \leq 2.37$.
Second layer of EM calorimeter	$w_{\eta 2}$	Lateral shower width, $\sqrt{(\sum E_i \eta_i^2)/(\sum E_i) - ((\sum E_i \eta_i)/(\sum E_i))^2}$, where E_i is the energy and η_i is the pseudorapidity of cell i and the sum is calculated within a window of 3×5 cells centered at the electron cluster position.
	R_ϕ	Ratio of the energy in 3×3 cells over the energy in 3×7 cells centered at the electron cluster position.
	R_η	Ratio of the energy in 3×7 cells over the energy in 7×7 cells centered at the electron cluster position.
First layer of EM calorimeter	w_{stot}	Shower width, $\sqrt{(\sum E_i (i - i_{\max})^2)/(\sum E_i)}$, where i runs over all strips in a window of $\Delta\eta \times \Delta\phi \approx 0.0625 \times 0.2$, corresponding typically to 20 strips in η , and i_{\max} is the index of the highest-energy strip. Used only for $E_T > 150 \text{ GeV}$.
	E_{ratio}	Ratio of the energy difference between the maximum energy deposit and the energy deposit in a secondary maximum in the cluster to the sum of these energies.
	f_1	Ratio of the energy in the first layer to the total energy in the EM calorimeter.
Track conditions	n_{Blayer}	Number of hits in the innermost pixel layer.
	n_{Pixel}	Number of hits in the pixel detector.
	n_{Si}	Total number of hits in the pixel and SCT detectors.
	d_0	Transverse impact parameter relative to the beam-spot.
	$ d_0/\sigma(d_0) $	Significance of transverse impact parameter defined as the ratio of d_0 to its uncertainty.
	$\Delta p/p$	Momentum lost by the track between the perigee and the last measurement point divided by the momentum at perigee.
TRT	eProbabilityHT	Likelihood probability based on transition radiation in the TRT.
Track-cluster matching	$\Delta\eta_1$	$\Delta\eta$ between the cluster position in the first layer and the extrapolated track.
	$\Delta\phi_{\text{res}}$	$\Delta\phi$ between the cluster position in the second layer of the EM calorimeter and the momentum-rescaled track, extrapolated from the perigee, times the charge q .
	E/p	Ratio of the cluster energy to the track momentum. Used for $E_T > 150 \text{ GeV}$.

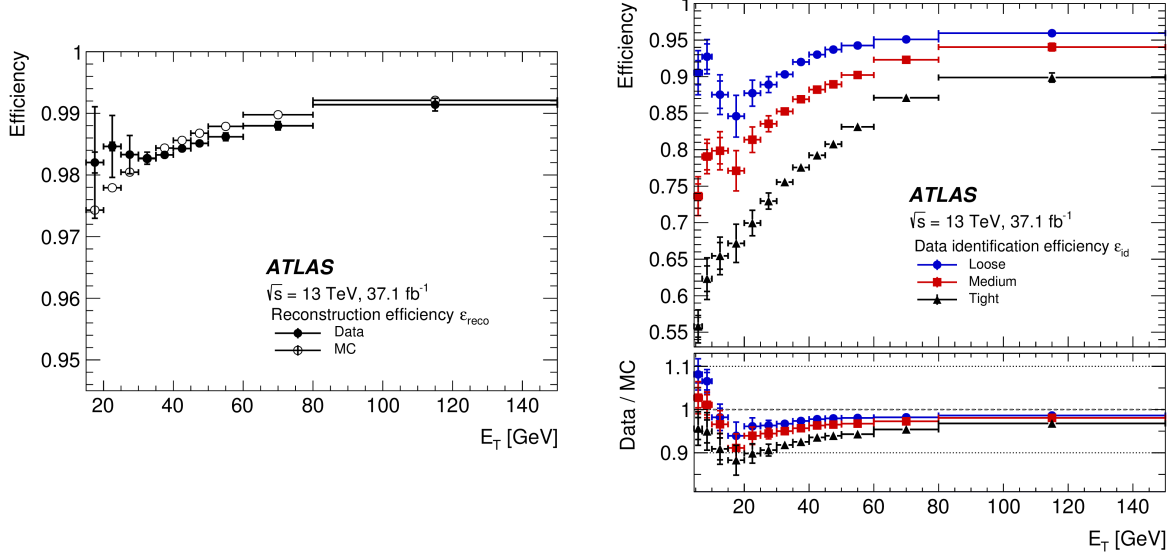


Figure 3.5: **2015-2016** *Left:* Electron candidate reconstruction efficiency, measured in simulation and in data, as a function of the candidate E_T . *Right:* Electron identification efficiency measured in data, as a function of electron E_T , for the three standard LH identification working points LOOSE (blue), MEDIUM (red), and TIGHT (black). The lower panel shows the ratio of the efficiency measured in data over that measured in simulation.

3.2.2 Muons

Muon Reconstruction

The reconstruction of muon candidates is performed by combining the tracking capabilities of the ID and the MS [70]. Muon reconstruction first starts with the independent reconstruction of charged-particle tracks within the ID and the MS. The independently formed tracks are subsequently combined to form a complete track representing the traversal of a muon through the full detector. The muon track in the ID is reconstructed like any other charged-particle track (Section 3.1).

Muon reconstruction within the MS starts with a pattern finding phase, looking for hit patterns each of the muon chambers to then form track segments. The track segments between different MS layers are then fit together to form muon track candidates. At least two matching track segments are required in order to build a muon track candidate, except in the transition region between the barrel and end-cap where single track-segment candidates can be used. Once a muon track candidate is formed from the combined segments, a global χ^2 fit is performed to improve the association of hits to each muon candidate. The χ^2 is repeated several times, removing outlying hits as necessary, until a threshold is met for all associated hits.

There are several algorithms used to combine the muon track candidates in the ID and MS, each using different sets of information related to the ID, MS, and calorimeters. At the time of the

current work, there are four standard combination algorithms used each based on the subdetectors used in their construction:

- **Combined Muon (CB)** This type of muon is formed with a global refit using all muon track candidate hits in the ID and the MS. Hits may be added or removed from the MS track candidate during the refit. Muons are reconstructed following an outside-in pattern recognition algorithm, in which the muon is first reconstructed in the MS and extrapolated inwards to the ID hits. A complementary, albeit non-standard, inside-out algorithm also exists.
- **Segment-tagged Muon (ST)** An ID track is classified as a muon if, once extrapolated to the MS, it is associated with at least one local track segment in the MDT or CSC chambers. Segment-tagged muons are used when a muon candidate crosses only one layer of the MS chambers, either because of their low p_T or because they fall into un-instrumented regions of the MS.
- **Calorimeter-tagged Muon (CT)** An ID track is classified as a muon if it is matched to an energy deposit in the calorimeter that is compatible with a minimum ionising particle. Calorimeter-tagged muons have the lowest purity, but recover acceptance in regions of the MS that are only partially instrumented to allow for cabling and services to the calorimeter and ID systems, particularly in the region $|\eta| < 0.1$.
- **Extrapolated Muon (ME)** This type of muon is based only on the track candidates formed in the MS and a loose requirement that the track candidate be pointing back towards the IP. Extrapolated muons are mainly used to extend the acceptance of muon reconstruction into the region $2.5 < |\eta| < 2.7$ that is not covered by the ID acceptance.

Muon Identification

Muon identification refers to the act of applying additional quality criteria on the reconstructed muon candidates in order to mainly suppress contamination from background sources that mimic muon signatures, such as pion and kaon decays, while ensuring high rates for the acceptance of prompt muons. There are three standard muon identification working points in ATLAS, each a subset of the previous one, and are referred to as the LOOSE, MEDIUM, and TIGHT muon identification working points. MEDIUM muons are the default in ATLAS analyses and can only be composed of CB and ME muons. As all muons used in the present thesis are MEDIUM muons, only this identification working point will be described in detail.

Reconstructed muon candidates originating from non-prompt sources such as in-flight decays of charged hadrons in the ID, are often characterised by the presence of a ‘kink’ in the reconstructed muon’s track. It is therefore expected that the independent momentum measurements made in the ID and MS may be incompatible for non-prompt sources of muon candidates. The muon identification criteria, then, make use of quantities that relate the ID and MS muon track candidates.

These quantities are described in Table 3.2. MEDIUM muons have a rather loose selection on the compatibility between the ID and MS momentum measurements and, with respect to those quantities in Table 3.2, are only required to have a q/p significance less than 7. On top of requirements on those quantities described in Table 3.2, the muon identification working points place additional requirements on the number and type of hits in the ID and MS. All identification working points require, in the ID, that there be at least 1 hit in the pixel subdetector, at least 5 hits in the SCT subdetector, less than 3 silicon holes,¹ and at least 10% of the TRT hits originally assigned to the muon track candidate exist after the combined reconstruction. MEDIUM muons further require that the CB muons have at least 3 hits in at least two MDT layers, except in $|\eta| < 0.1$ where tracks with at least one MDT layer but no more than one MDT hole are allowed. The ME Medium muons are required to have at least 3 MDT or CSC layer hits, and are employed only in $2.5 < |\eta| < 2.7$.
reference n MDT/CSC hits figure?

Quantity Name	Measurement	Description
q/p significance	$ (q/p)^{\text{ID}} - (q/p)^{\text{MS}} / \sqrt{\sigma_{p_T}^{\text{MS}} + \sigma_{p_T}^{\text{ID}}}$	Absolute value of the difference between the ratio of the charge and momentum of the muon candidates measured in the ID and MS, divided by the quadrature sum of the corresponding uncertainties.
ρ'	$ p_T^{\text{MS}} - p_T^{\text{ID}} / p_T^{\text{Combined}}$	Absolute value of the difference between the transverse momentum measurements in the ID and the MS, divided by that of the combined muon candidate.
χ^2_{norm}	—	Normalized χ^2 of the combined muon track fit

Table 3.2

¹A missing hit is considered a ‘hole’ only if it falls between hits successfully assigned to a given track.

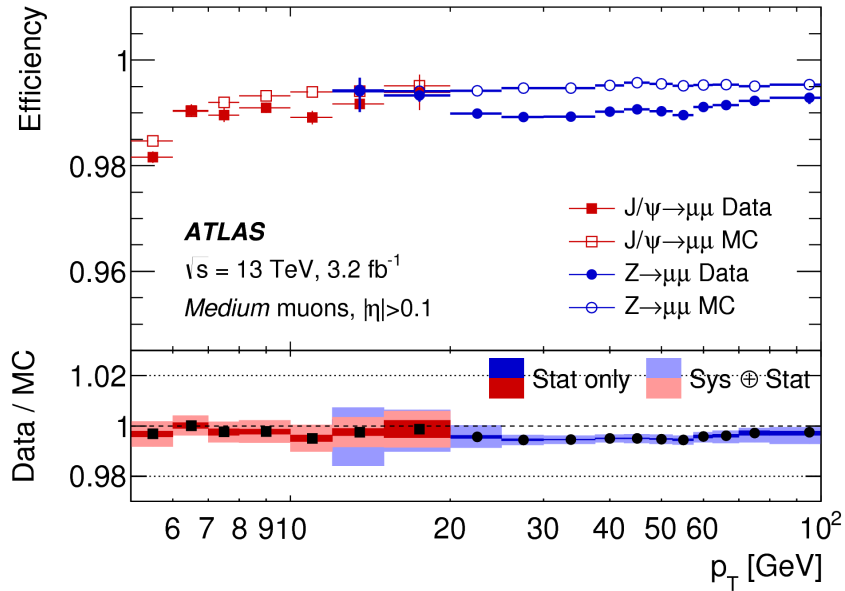


Figure 3.6: From Ref. [70].

3.3 Jets

Due to the confining nature of QCD, color-charged quarks and gluons produced in the initial pp interactions do not exist as free states for observably meaningful timescales and therefore do not leave unambiguous signatures in the detector. Instead, their production is characterised by the radiation of additional quarks and gluons roughly collinear with the initiating colored particles. The radiation pattern of these colored objects is dictated by the color field that binds them and eventually results in the production of color-neutral hadrons. The collimated spray of hadrons as a result of this *hadronisation* process leads to the phenomenology of *jets*, which are the macroscopically observable signature of produced quarks and gluons. The reconstruction of jets refers to any suitable, i.e. physically meaningful and stable, method for grouping together, or *clustering*, the end-products of the hadronisation process in such a way that the properties of the initiating quarks or gluons, such as their quantum numbers and/or kinematics, can be inferred from the resulting clustered object. The standard method for reconstructing jets in ATLAS will be introduced in Section 3.3.1. In Section 3.3.2, the steps taken to turn these reconstructed jets into accurate representations of the initiating quarks and/or gluons, so that they can be used meaningfully in physics analyses, will be discussed.

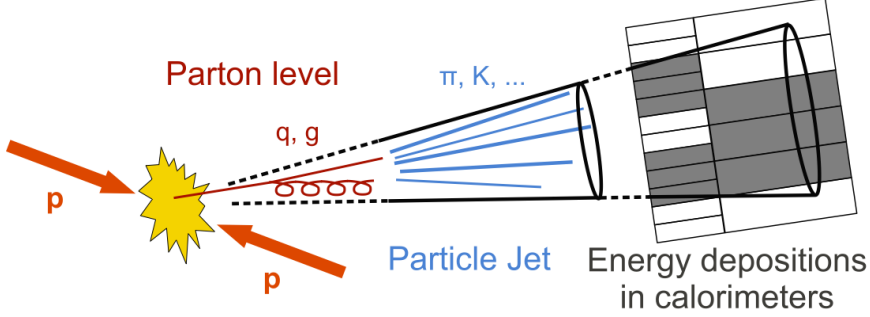


Figure 3.7: Illustration of the jet formation process, beginning with the initiating quark and/or gluons (partons) which hadronise to form particle jets discernible by the tracking detectors in the ID and calorimeter jets defined by energy depositions in the calorimeter systems.

3.3.1 Jet Reconstruction

Topological Cell Clustering

The process of jet reconstruction begins first with the clustering of the lowest level calorimeter elements, *calorimeter cells*, corresponding to the readout channels in the LAr and tile calorimeters. Figure 3.8 gives an idea of the calorimeter cell granularity across the calorimeter system. The clustering algorithm used by ATLAS is a three-dimensional *topological clustering* algorithm [71, 72]. The highly granular calorimeter system used in ATLAS, with its finely segmented lateral readout and longitudinal sampling layers, allows for the subsequent topological clusters ('topo-clusters') to capture in detail the energy-flow details of jets. Topo-cluster formation begins by first identifying so-called *seed cells* which have a rather high signal-to-noise ratio (S/N), $S/N > 4$. Here, the signal is defined as the absolute value of the calorimeter-cell energy measurement, $|E|$, and the noise is defined as the sum in quadrature of the RMS of the electronics and expected pileup noise contributions. Cells neighboring the seed cells satisfying $S/N > 2$ are then collected into the topo-cluster. A neighboring cell is defined in three-dimensions as either the calorimeter cells directly adjacent within the same calorimeter layer as the seed cell, or, if in adjacent layers or in different calorimeter sub-systems, cells having at least partial overlap in the (η, ϕ) plane with the seed. The final set of cells, the perimeter cells, satisfying $S/N \geq 0$ are then collected. This last threshold essentially collects all those cells surrounding already-collected cells within each layer. Figure 3.9 illustrates the concept of topological cell clustering as described here.

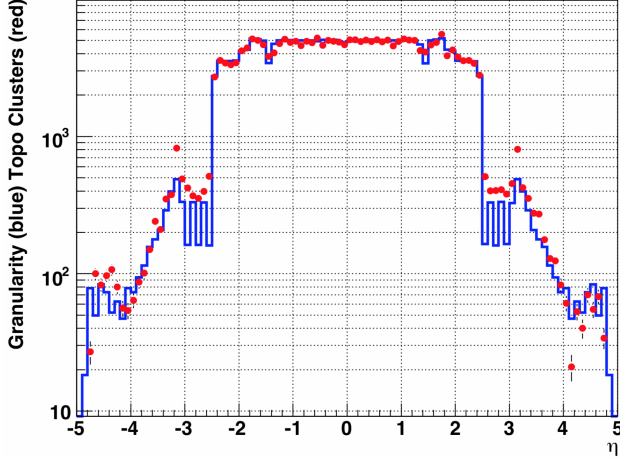


Figure 3.8: The blue histogram shows the average calorimeter cell granularity, i.e. number of calorimeter cells per $\Delta\eta = 0.1$, as a function of detector η . The red points show an approximation of the blue histogram based on calculations of the expected noise per calorimeter cell. From Ref. [71].

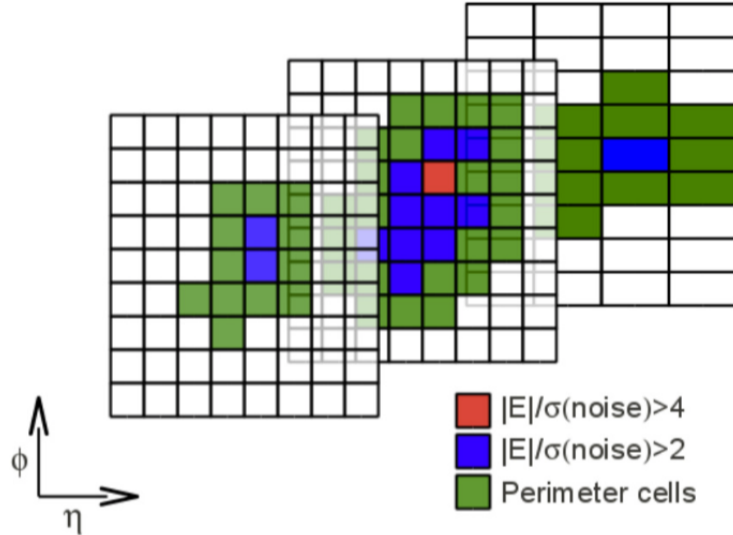


Figure 3.9: Illustration of calorimeter-cell topological clustering across the three layers of the hadronic calorimeter. Indicated are the cells satisfying the signal-to-noise requirements for the seed (red), neighbor (blue), and perimeter (green) cells that make up the final three-dimensional topo-cluster.

Jet Finding

Once the set of topo-clusters is formed, the process of jet finding begins. As there is no single unique way to define a jet, there is a wide variety of jet finding algorithms whose purpose is to associate jet constituents — here, the calorimeter-cell topo-clusters — to form the final object

representing the jet. The default jet finding algorithm used by ATLAS is the *anti- k_t* jet clustering algorithm [73]. The anti- k_t algorithm belongs to the more general class of sequential recombination algorithms and is favored for its infrared and collinear (IRC) safe properties as well as the fact that it tends to produce rather simple jets, geometrically, that are circular in the $\eta - \phi$ plane, as seen in Figure 3.10. IRC safety in jet finding algorithms refers to the property that neither additional collinear splitting of jet constituents (e.g. the initiating or radiated partons) nor soft emissions should change the clustered jet. IRC-safe jets are therefore robust against these divergent regimes of QCD, sensitive to arbitrary calculational choices made in perturbation theory, and makes them physically meaningful observable objects with which one can make predictions.

The anti- k_t algorithm takes as input constituents the topo-clusters described in Section 3.3.1 and computes the quantities,

$$d_{ij} = \min \left(\frac{1}{k_{T,i}^2}, \frac{1}{k_{T,j}^2} \right) \frac{\Delta R_{ij}^2}{R^2}, \quad (3.4)$$

$$d_{iB} = \frac{1}{k_{T,i}^2}, \quad (3.5)$$

with $\Delta R_{ij}^2 = (\eta_i - \eta_j)^2 + (\phi_i - \phi_j)^2$, **its rapidity, right?** R is a parameter whose value regulates the radial extent of the jet, and $k_{T,i}$ is the transverse momentum of the i^{th} constituent. The d_{ij} and d_{iB} quantities are ‘distance’ metrics used in the clustering of input topo-cluster constituents. The former represents the ‘distance’ between the i^{th} and j^{th} constituent while latter represents the ‘distance’ between the i^{th} constituent and the beam-line, introduced to distinguish between constituents originating from the primary hard-scatter vertex and those originating from soft proton interaction remnants. The work to be discussed in the present thesis sets $R = 0.4$, which is the standard used in ATLAS.

The anti- k_t algorithm proceeds by clustering those constituents whose inter-distance is smallest, thereby tending to cluster higher- p_T constituents together, which can be seen by inspection of Equation 3.4 and 3.5. If, of the set of input constituents, the smallest distance is a d_{ij} , the associated constituents indicated by i and j are recombined to form a single constituent in the list that replaces them both. If the smallest distance is a d_{iB} , then the constituent indicated by index i is removed from the set of constituents and is considered as a complete jet. This process repeats, starting with the now smaller (due to successful constituent recombination or removal) set of constituents, until no constituents are left. The result of this process is a set of recombined constituents that represent jets, as illustrated in Figure 3.10.

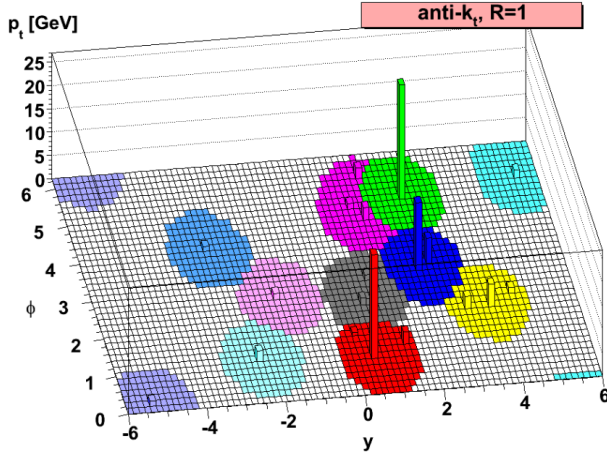


Figure 3.10: An illustration of jet constituents clustered by the anti- k_t algorithm. Seen are the energetic constituents. The filled and colored circles represent areas populated by soft jet constituents, and represent the jet *catchment area* [74] whose size is dictated by the R parameter in the anti- k_t algorithm (Equation 3.4). Figure taken from Ref. [73].

3.3.2 Jet Calibration

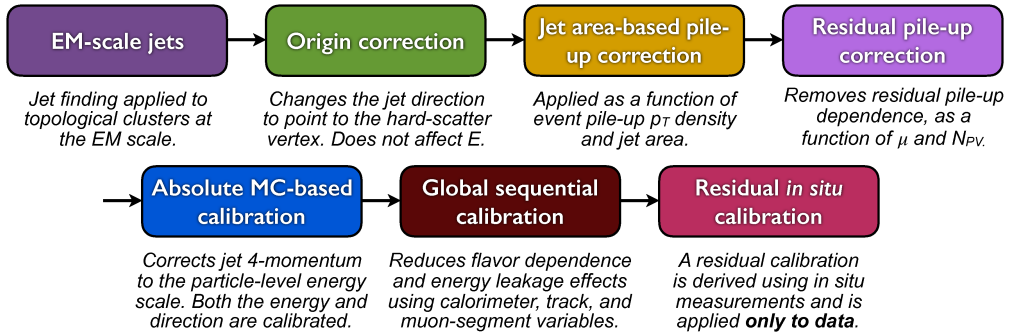


Figure 3.11: Flowchart representing the sequence of steps taken in the jet calibration. From Ref. [75].

The jets reconstructed following the steps described in Section 3.3.1 are objects clustered at the electromagnetic (EM) scale, which correctly measures the energy of electromagnetic showers but does not accurately account for energy depositions characteristic of hadronic particle decays and interactions. These jets are therefore referred to as ‘EM-scale’ jets. To correctly assign meaningful energy and momentum measurements to the reconstructed jets that correspond to the energies and momenta of the initiating, underlying particle-level jets, several *jet energy scale* (JES) calibration steps are taken [75]. The steps are detailed in the flowchart in Figure 3.11 and will be briefly described in the following text. The measurements made at each of these steps are subtle and account for many effects not present in the case of the reconstruction of electrons and muons, for example, due to the fact that jets are rather complicated collective phenomena whose measurements

rely primarily on a single subsystem (the calorimeters). Not only are electrons and muons generally simpler objects, seeded by comparatively unambiguous tracks within the ID, their energy and momentum measurements are the result of a combination of well-defined measurements made by two independent subsystems (ID measurements combined with EM calorimeter or the MS) that provide independent cross-checks on the validity of the measurements made by each. For the most part, this is not the case of the reconstruction of jets within ATLAS and as a result many of the choices made in the calibration of EM-scale jets have non-negligible impact in the analyses that will be discussed in this thesis, whereas the analogous choices for electrons and muons have minimal impact. For this reason the jet calibration procedure outlined in Figure 3.11 will be outlined briefly in the text that follows.

Jet Origin Correction

The reconstructed EM-scale jets are built with the assumption that they originate from the geometric center of the detector, as opposed to the primary hard-scatter vertex from which the initiating partons arise. The so-called jet origin correction, therefore, refers to recalculating the jet four-momentum vector by adjusting it in such a way that it points to the primary hard-scatter vertex. This correction acts primarily to improve the η resolution of jets. This procedure is only one hundred percent accurate, of course, under the assumption that all of the jet constituents going into the EM-scale jet reconstruction originated from the hard-scatter vertex, as opposed to some fraction having come from a pileup vertex, for example.

Pileup Corrections

Jets are extended object with relatively large *catchment areas* [74] that make them susceptible to pileup effects. Several corrections, therefore, to the jet energy are taken in order to account for contributions to the EM-scale jet reconstruction arising from both in-time and out-of-time pileup interactions.

The first pileup correction is an area-based correction which subtracts the per-event pileup contribution to the p_T of each jet based on the jet's area, where the jet area is defined as in Ref. [74]. This pileup contribution is taken as the median p_T density, ρ , of jets in the $\eta - \phi$ plane and can be thought of as a baseline ‘noise’ term distributed evenly through the calorimeter that contributes to a jet’s reconstructed energy.

After the area-based pileup correction is made, there still remains residual dependence of the reconstructed jet p_T on the number of reconstructed primary vertices and on the number of interactions, μ . These dependences are measured by performing linear fits of the jet p_T as a function of each quantity, binned as a function of the detector η , η_{det} .

The final, pileup-corrected jet p_T is given by Equation 3.6:

$$p_T^{\text{Corr}} = p_T^{\text{Reco}} - \underbrace{\rho \times A}_{\text{Area-based}} - \underbrace{\alpha \times (N_{\text{PV}} - 1) - \beta \times \mu}_{\text{Residual}}, \quad (3.6)$$

where A is the jet area, and the α and β terms are derived from the linear fits mentioned above and are $\alpha = \partial p_T / \partial N_{\text{PV}}$ and $\beta = \partial p_T / \partial \mu$, respectively. The former accounts for effects arising as a result of in-time pileup and the latter for those due to out-of-time pileup. The effect of the pileup corrections is shown in Figure 3.12, where it can be seen that the area-based correction is an overall offset, as expected, after which residual pileup dependencies of the jet p_T as a function of $|\eta_{\text{det}}|$ are still observed. This residual pileup dependence is greater in the forward regions of the detector where pileup and background activity is largest.

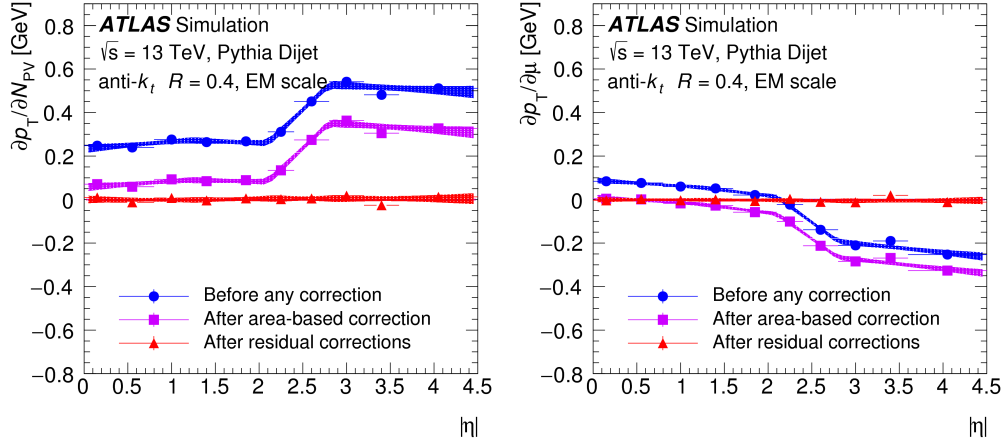


Figure 3.12: Dependence of the p_T of EM-scale reconstructed jets on N_{PV} (in-time pileup) (*left*) and on μ (out-of-time pileup) (*right*). The blue curves show the dependence prior to any pileup corrections, the purple curves are after the area-based correction, and the red curves are the final dependence after the full pileup correction described in Equation 3.6 is taken into account. Figures taken from Ref. [75].

Absolute Jet Energy Scale and η Correction

This correction corrects the EM-scale reconstructed jet to the true energy scale based on particle-level jets and is therefore purely MC-based. Particle-level jets are jets clustered using the anti- k_t algorithm using the generator-level particles at the end of the hadronisation step as the input constituents, and therefore represent the reconstructed jet prior to its interaction with the calorimeter (see Figure 3.7). The correction accounts for mismodelling of the inactive material within the detector, radiation not accounted for in the reconstructed calorimeter-based jet due to the clustering algorithm not accepting it ('out-of-cone radiation'), non-compensation of the hadronic calorimeters², and for effects related to detector geometry or transitions between calorimeter technologies.

The correction is derived by matching the EM-scale reconstructed jets, in simulation, to the particle-level jets and deriving the average energy response, $E^{\text{Reco}}/E^{\text{Truth}}$, where E^{Truth} is the energy of the particle-level jet. The inverse of this energy response is taken as a correction to the

² Compensating...

EM-scale reconstructed calorimeter jets in simulation. An additional correction accounts for biases observed in the EM-scale reconstructed jet η , which is largest in regions wherein a jet is likely to encompass two calorimeter regions or technologies which result in different energy responses. The η correction is derived as the difference between the reconstructed and particle-level jet η values and applied to the EM-scale reconstructed calorimeter jets as in the case of the energy-response correction. The average energy response, as a function of EM-scale jet p_T , and the η correction is shown in Figure 3.13. After this correction stage, jets are referred to as being at the EM+JES scale.

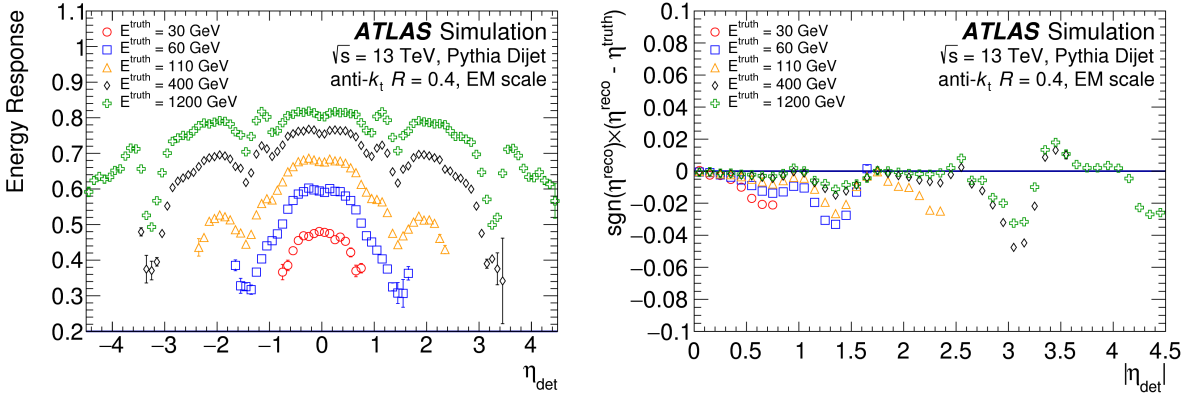


Figure 3.13: *Left:* Average energy response as a function of jet detector η , η_{det} . The colors correspond to different energy regimes for the particle-level jet to which the EM-scale reconstructed jet is matched. The inverse of the response is the final correction and can be seen to be largest for lower- p_T jets. *Right:* Difference in η for the EM-scale reconstructed jet and the particle-level jet to which it is matched. The bias is clearly seen, with values typically negative, and it being largest for $|\eta_{\text{det}}| \sim 1.4$ (~ 3.1), corresponding to the barrel-endcap (endcap-forward) transition regions.

Global Sequential Calibration

The so-called Global Sequential Calibration (GSC) is a catch-all correction to account for remaining dependencies of the EM+JES-scale jets on the jet shower shapes as well as fluctuations in the jet flavor composition and inter-jet energy distribution. This correction improves the handling of fluctuations in the composition of the particles that initiate the jet; for example, correcting for the differences expected between quark- and gluon-initiated jets. The former (quark-initiated) jets are typically more collimated with fewer, but higher- p_T , hadronic constituents. The latter (gluon-initiated) jets typically contain many more, softer- p_T , particles and have wider transverse profiles (and therefore do not traverse as far into the calorimeter). The GSC has five stages, each following a numerical inversion of a corresponding jet response as in the case(s) described in Section 3.3.2, but are based on observables sensitive to the jet shower profile and growth within the calorimeter as well as on the number and type of tracks associated with the reconstructed jet. The use of tracking information from muons in this correction additionally helps with correcting the energy response

of jets that are not fully contained in the calorimeter but leak into the MS, so-called *punch-through jets*. Figure 3.14 illustrates the concept of jet punch-through.

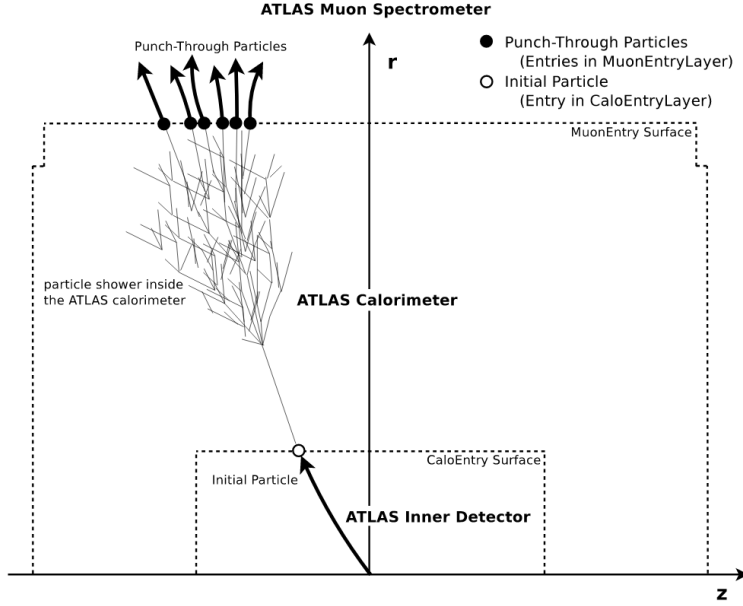


Figure 3.14: Illustration of jet punch-through. High momentum particles produced in the shower of an energetic jet within the hadronic calorimeter escape into the muon spectrometer, leaving detectable signatures in the muon chambers. It can be seen that energy and/or momentum may be left unaccounted for in the final event reconstruction or be assigned to separate muon objects as opposed to the initiating jet from which the punch-through particles arise. Such effects disrupt the proper assignment of energy-momentum to the jet and can spoil the overall momentum balance in the event.

In-situ Corrections

The last stage of the jet calibration accounts for remaining differences in the EM+JES jet response between data and simulation and is primarily derived using events from data, as opposed to MC simulation.³ There are two classes of correction, the first being the so-called η -intercalibration step which corrects the average response of forward jets ($0.8 < |\eta| < 4.5$) to that of well-measured central jets using dijet events in which the two jets (the one in the forward region and the other in the central region) are back-to-back in ϕ . The second class of corrections is based on the method of balancing an EM+JES scale jet against a well-measured reference object. The balance methods use only central jets ($|\eta| < 0.8$) and the choice of the reference object provides the p_T scale to which the response correction applies. Balance methods using well-measured photons and Z boson decays to leptons ($Z \rightarrow ee$ and $Z \rightarrow \mu\mu$) as the reference objects are used to derive the response corrections for jets with p_T up to 950 GeV. Response corrections for jets covering p_T ranges up to

³In this case, the term ‘in-situ’ means that the corresponding corrections are derived using data, as opposed to using events from Monte-Carlo simulation.

2 TeV are derived using a multijet balance method in which a high- p_T central jet is balanced against a reference system of lower- p_T jets. The final response correction as a function of jet p_T derived using these in-situ methods is shown in Figure 3.15.

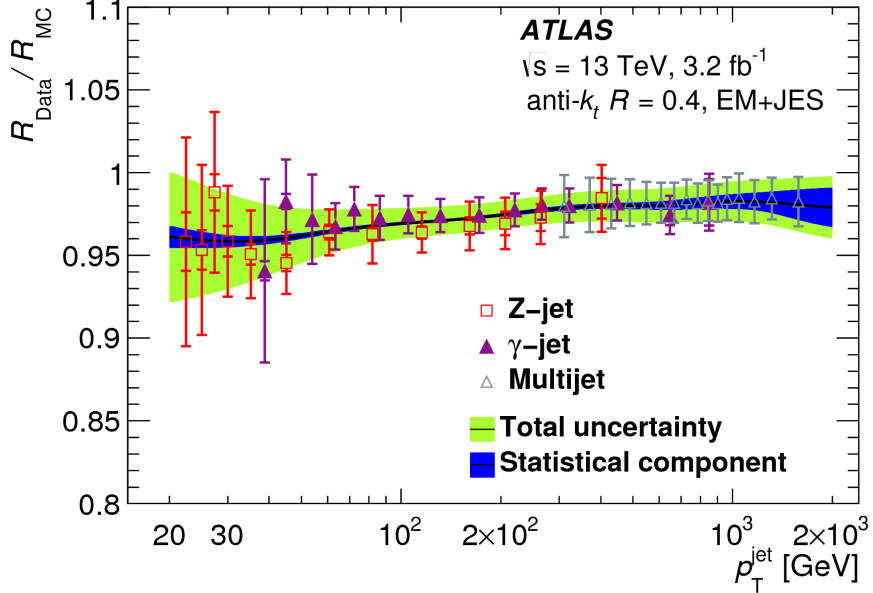


Figure 3.15: Ratio of the EM+JES jet response in data to that in MC simulation as a function of jet p_T . The different markers indicate the measurement contributions from the different reference-object used to derive the in-situ response corrections. The final response correction is given by the black line. The total uncertainty on the response is given by the green band and the blue band indicates only the statistical component of the uncertainty. Figure from Ref. [75].

3.3.3 Flavor Tagging of Jets

The ability to identify jets containing heavy-flavored hadrons, i.e. jets containing b - and c -flavored hadrons, is an important aspect to many of the most critical measurements and analyses being done at the large LHC experiments. The SM top-quark is the heaviest known elementary particle, the second-most recent elementary particle to be discovered, and, given its importance to electroweak and Higgs physics, is an object subjected to high levels of precise study at the LHC. The top-quark decays before hadronisation timescales and therefore its decay products, which are a W -boson and a b -quark nearly 100% of the time, carry away information characterising its properties. Being able to characterise the jets initiated by the hadronisation of these b -quarks, then, is of critical import if the physics of the top-quark wish to be understood. The recent discovery of an SM-like Higgs boson, with a mass of $m_h = 125$ GeV, decays to a pair of b -quarks nearly 60% of the time. Without question, then, the thorough study of the Higgs boson necessitates the ability to precisely identify the presence of the pair of b -initiated jets from its decays. Additionally, we will see in subsequent chapters that the presence of b -quark initiated jets is a characteristic signature of many BSM physics scenarios. The identification of these types of jets, a process referred to as

‘flavor tagging’, is of the utmost importance to analyses performed with the ATLAS detector as well as in the work to be presented in this thesis. Jets tagged as having likely arisen as a result of the hadronisation of an initiating b -(c)-quark are referred to as ‘ b -tagged jets’ (‘ c -tagged jets’), or simply as ‘ b -jets’ (‘ c -jets’). All other jets then are assumed to have arisen from the decay of light-flavor quarks and are referred to as ‘light-flavor jets’ (‘light-jets’).

Heavy-flavor tagging of jets relies on the relatively long lifetimes of the b - and c -hadrons which initiate them. The typical b -hadron lifetime is $\tau \approx 1.6$ ps ($c\tau \approx 450 \mu m$), which leads to b -hadrons traversing typically macroscopic distances away from the primary hard-scatter vertex before they decay. As seen in Figure 3.16, b -hadrons with transverse momenta on the order of 50 GeV will travel nearly half a centimeter before decaying. Also seen in Figure 3.16, those b -hadrons with p_T values nearing 250 GeV will actually decay outside of the beam-pipe within the region of the IBL. Given the high spatial resolution of the ID pixel and SCT detectors discussed in Section 2.2.2, the presence of these long-lived particles should be detectable via the presence of at least one secondary decay vertex corresponding to the point at which the heavy-flavored hadron decays. Figure 3.17 illustrates the standard topology of a heavy-flavor initiated jet with a secondary decay vertex that is displaced with respect to the primary hard-scatter vertex and is the source of displaced tracks.

The algorithms used to identify heavy-flavor initiated jets, then, rely on information characterising the long lifetimes of the initiating particles and on the presence of secondary decay vertices within the jet. These high-level algorithms used to identify these jets take as input information provided by taggers that rely on low-level information based on the presence of displaced tracks and secondary vertices. These low-level taggers will be introduced in Section 3.3.3 and the construction of the high-level tagger, used in the analyses to be presented in this thesis, will be presented in Section 3.3.3.

Low Level Taggers and Inputs

The final algorithm used to identify b -tagged jets take as input the outputs from several low-level b -tagging algorithms. There are two classes of low-level algorithms: those that rely on the impact parameter information of the tracks associated with the jets and those that rely on the explicit reconstruction of secondary decay vertices within the jet [76]:

- **IP2D and IP3D** The IP2D and IP3D algorithms make use of the signed transverse impact parameter significance of tracks to construct discriminating variables. The IP3D algorithm additionally makes use of the longitudinal impact parameter significance. The algorithms rely on constructing log-likelihood ratios (LLR) taking as inputs probability density functions (PDFs) for b -, c -, and light-flavor jet probabilities on a per-track basis. See Figure 3.17 for an illustration of the signed impact parameter. Tracks associated with secondary decay vertices in heavy-flavor jets tend to have positively signed impact parameters since they are produced *within* the jet cone. Signed impact parameter quantities tend to be symmetric for light-flavor jets. See Figure 3.18.

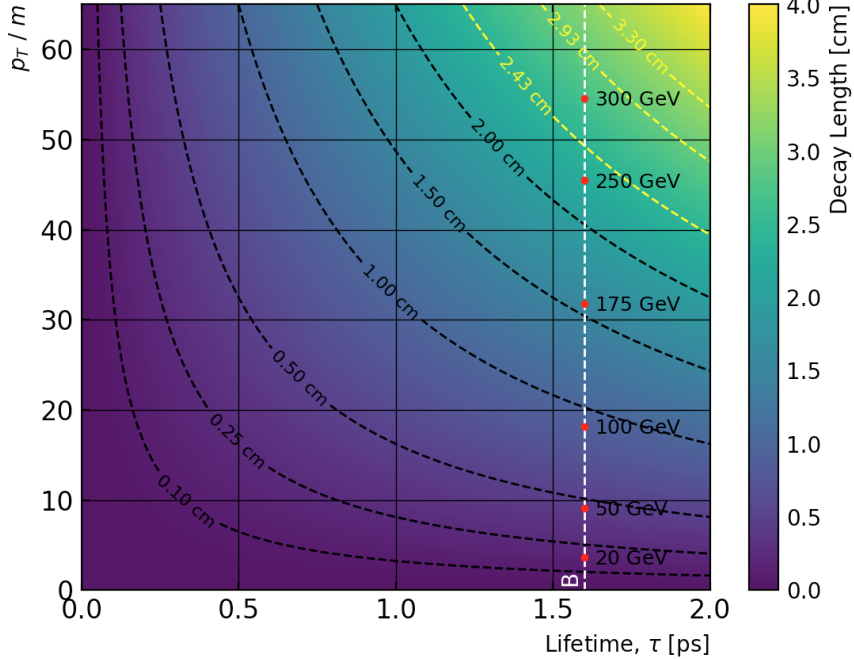


Figure 3.16: Particle decay length as a function of its lifetime and transverse momentum normalised to its rest mass. The white-dashed line indicates the average lifetime of B -hadron species, taken as 1.6 ps, with a mass taken to be 5.5 GeV. The red-dots along the B -hadron line indicate locations for specific transverse momenta for the decaying B -hadron. The yellow contours indicate the locations of the IBL (Figure 2.14), with 2.43 cm corresponding to the beam-pipe radius. Perhaps move this plot elsewhere? Add references to PDG

- **Secondary Vertex Finding Algorithm (SV1)** The SV1 algorithm [77] reconstructs a single displaced secondary vertex within a jet, starting from the set of all possible two-track vertices while rejecting tracks likely to be associated with non-heavy-flavored long-lived particles (K_s or Λ), photon conversions, or vertices due to detector material interactions. The inclusive secondary vertex and associated tracks are then used to construct discriminating observables sensitive to the differences between b -, c -, and light-flavor jets.
- **Multi-vertex Finding Algorithm (JetFitter, JF)** The JetFitter algorithm [78] attempts to reconstruct the full b -hadron decay chain using a modified Kalman filter [79] which assumes a common line on which the primary, b -hadron, and c -hadron decay vertices lie. As with SV1, the construction of many discriminating observables related to the reconstructed set of vertices are used to build templates for b -, c -, and light-flavor jets.

Figure 3.18 provides an example of a few observables provided by the low-level tagging algorithms.

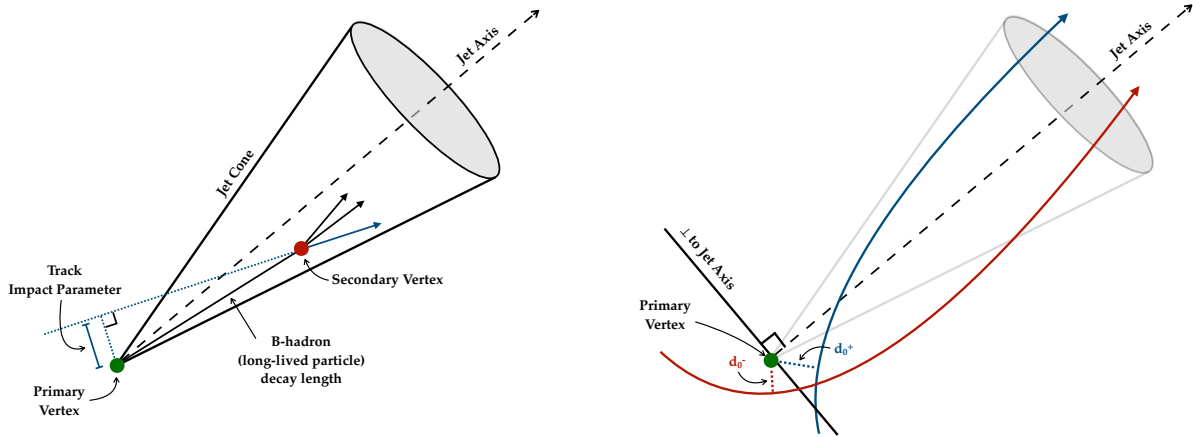


Figure 3.17: *Left*: Topology of a b -jet. The b -hadron produced near the primary hard-scatter vertex (green dot), initiating the b -jet, has a long lifetime and decays a macroscopic distance away from the primary hard-scatter vertex to produce a secondary vertex (red dot) from which additional tracks are produced and subsequently reconstructed. The tracks originating from the secondary vertex will have larger impact parameters relative to the primary hard-scatter vertex as compared to tracks originating from the primary hard-scatter vertex. *Right*: Illustration of signed impact parameter, specifically the signed transverse impact parameter d_0 . The blue track has a transverse impact parameter whose projection onto the jet axis is in the direction in which the jet momentum points and is given a positive d_0 . The red track's transverse impact parameter's projection onto the jet axis points opposite to the jet momentum and is given a negative d_0 .

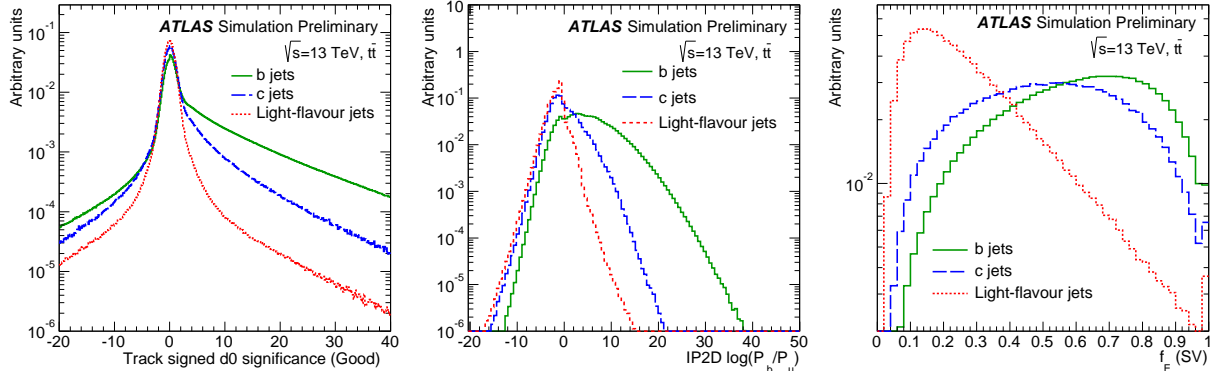


Figure 3.18: Examples of a few low-level quantities used in the ATLAS flavor tagging algorithms. The blue histograms are distributions associated with b -jets, green are those of c -jets, and red are those of light-flavor jets. *Left*: Two-dimensional (signed) d_0 significance for tracks matched to jets. *Middle*: IP2D b -jet log-likelihood ratio. *Right*: Energy fraction, defined as the energy of the tracks in the displaced vertex reconstructed by the SV1 algorithm relative to the energy of all tracks in the jet.

High Level Tagger: MV2

The low-level taggers discussed in the previous section provide a set of many useful and complementary observables. In an attempt to make the most efficient use of all the information provided by

this set of observables, a boosted decision tree (BDT) algorithm is used to combine the outputs of these low-level algorithms. This algorithm, referred to as the MV2 b -tagging algorithm, is trained using the ROOT Toolkit for Multivariate Data Analysis (TMVA) [80]. In the analyses based on data recorded by ATLAS between 2015–2016, the MV2 algorithm was trained using jets from a simulated sample of top-quark pair production events. For the analyses based on the full Run-II data recorded by ATLAS, up to and including the year 2018, the MV2 algorithm was retrained using a sample composed of jets both from top-quark pair production events as well as from simulated events of a BSM physics scenario of a heavy Z' decaying to $b\bar{b}$. The latter was included in the retraining so as to allow the algorithm to have in its training sample high- p_T jets that are not present in the SM top-quark pair production events, as illustrated in Figure 3.19.

Figure 3.19 shows a distribution of the MV2 algorithm’s output. The MV2 score is computed on a per-jet basis, using the set of low-level inputs listed in Table 3.3. Working points, defined with different target-efficiencies for accepting b -tagged jets, are defined by selection thresholds on the MV2 discriminant. The standard ATLAS b -tagging working points are defined for accepting b -jets with $p_T > 20$ GeV with average efficiencies of 60%, 70%, 77%, and 85%. The working points are based on selections made on the MV2 output score and are defined in Table 3.4, along with the rejection factors⁴ for c -jets, τ -jets⁵, and light-flavor jets.

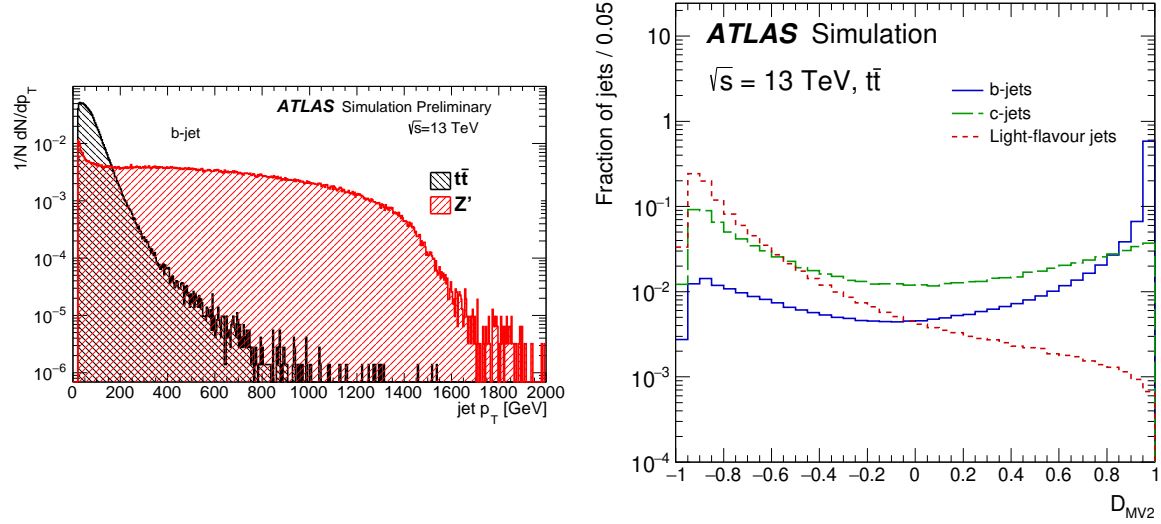


Figure 3.19: *Left:* Distribution of jet p_T for jets used in the training of the MV2 BDT algorithm. The Z' sample of jets is only included in the MV2 training relevant to the analyses based on the full Run-II dataset collected by ATLAS. *Right:* Distribution of the BDT-based MV2 b -tagging algorithm output score, shown for b -jets (blue), c -jets (green), and light-flavor jets (red).

⁴The rejection factor is defined as the inverse of the efficiency. A rejection factor of 100 means, therefore, that the associated object is accepted — on average — 1 out of every 100 times that it appears.

⁵Hadronically decaying τ leptons are accepted by the b -tagging algorithms at rates higher than light-flavor jets due to the non-negligible decay length of the τ lepton which give them b -like characteristics.

Table 3.3: Variables used as input to the high-level tagger MV2c10.

Input Source	Input Name	Description
Kinematics	$p_T(\text{jet})$	Jet transverse momentum
	$\eta(\text{jet})$	Jet pseudorapidity
IP2D, IP3D	$\log(p_b/p_{\text{light}})$	Likelihood ratio between the b - and light-jet hypotheses
	$\log(p_b/p_c)$	Likelihood ratio between the b - and c -jet hypotheses
	$\log(p_c/p_{\text{light}})$	Likelihood ratio between the c - and light-jet hypotheses
Secondary Vertex (SV1)	m_{SV}	Invariant mass of tracks at the secondary vertex assuming pion masses
	f_E	Fraction of the charged jet energy in the secondary vertex
	N_{TrkAtVtx}	Number of tracks used in the secondary vertex
	$N_{2\text{TrkVtx}}$	Number of two-track vertex candidates
	L_{xy}	Transverse distance between the primary and secondary vertices
	L_{xyz}	Distance between the primary and secondary vertices
	S_{xyz}	Distance between the primary and secondary vertices divided by its uncertainty
	$\Delta R(\text{jet}, \text{SV})$	ΔR between the jet axis and the direction of the secondary vertex relative to the primary vertex
JetFitter (JF)	$N_{2\text{TrkVtx}}$	Number of two-track vertex candidates (prior to JetFitter decay-chain fit)
	m_{JF}	Invariant mass of tracks from displaced vertices assuming pion masses
	S_{xyz}	Significance of the average distance between the primary and displaced vertices
	f_E	Fraction of the charged jet energy in the secondary vertices
	$N_{1\text{-trk vertices}}$	Number of displaced vertices with one track
	$N_{\geq 2\text{-trk vertices}}$	Number of displaced vertices with more than one track
	N_{TrkAtVtx}	Number of tracks from displaced vertices with at least two tracks
	$\Delta R(\vec{p}_{\text{jet}}, \vec{p}_{\text{vtx}})$	ΔR between the jet axis and the vectorial sum of the momentum of all tracks attached to displaced vertices

b -jet Identification Calibration

As the efficiencies for the MV2 algorithm detailed in Table 3.4 are based entirely on MC simulation, a calibration procedure is performed to correct the MC-based efficiencies to those observed in data. This is necessary to get an accurate prediction in simulation of the rate of b -tagged jets occurring in data. The efficiencies (and rejection factors) in Table 3.4 are therefore measured in data. The result of the calibration is a correction scale-factor, applied on a per-jet basis, that is defined as $\text{SF} = \varepsilon_{\text{Data}}/\varepsilon_{\text{MC}}$, where $\varepsilon_{\text{Data(MC)}}$ are the measured efficiencies in data (MC) for a jet to be tagged as a b -jet, measured as a function of the jet p_T and η . The b -tagging SF are derived using a sample enriched in b -tagged jets arising from SM top-quark pair production [76]. The b -tagging efficiencies in MC and data as well as the data-to-MC efficiency SF are shown in Figure 3.20. The rate of c -, τ -, and light-flavor jets to be identified as b -tagged jets corresponding to the rejection factors listed in Table 3.4, also have corresponding correction scale-factors using events in data enriched

Table 3.4: Working points defined for the MV2 b -jet identification algorithm. The cut thresholds on the MV2 discriminant associated with a given b -jet efficiency (working point) are given in the second column. The rejection factors for c -, τ -, and light-flavor jets are shown in the three right-most columns. The precise MV2 discriminant thresholds are dependent on the calibration, and differ between the analyses based only on the data collected in the years 2015-2016 and the full Run-II dataset including the years 2017 and 2018. The MV2 threshold values shown here are those corresponding to the full Run-II dataset.

b -jet efficiency	MV2 selection	Rejection Factor		
		c -jet	τ -jet	Light-flavor jet
60%	> 0.94	23	140	1200
70%	> 0.83	8.9	36	300
77%	> 0.64	4.9	15	110
85%	> 0.11	2.7	6.1	25

in c -jets and mis-tagged light-flavor jets [76, 81, 82]. These latter scale-factors correct the rate of mis-tagging (i.e. rate of identifying jets as b -jets when they are not initiated by b -hadrons).

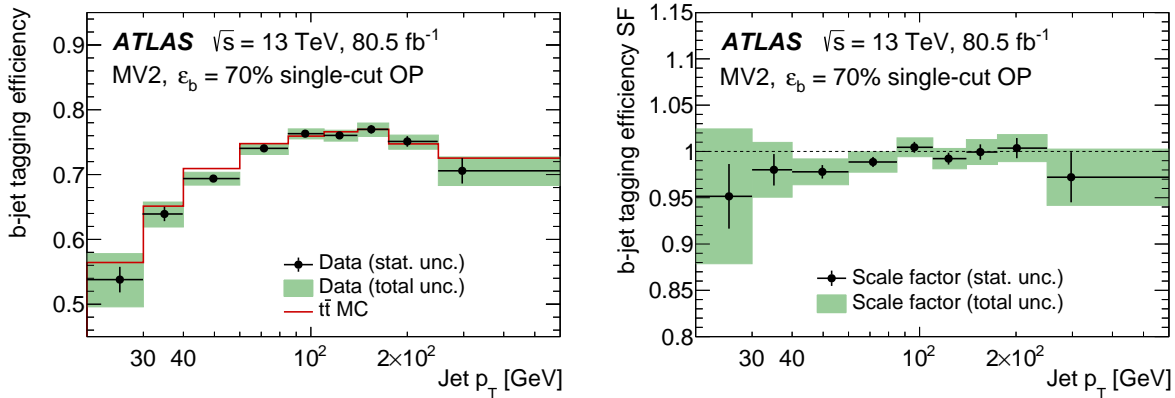


Figure 3.20: *Left:* b -jet tagging efficiency as a function of jet p_T for the 70% WP of the MV2 b -jet tagging algorithm in MC (top-quark pair production, in red) and data (black points). Efficiency values below and above 70% occur, but the efficiency averaged over the full range shown is roughly 70%. *Right:* b -jet tagging efficiency correction scale-factors for the 70% WP of the MV2 b -jet tagging algorithm as a function of jet p_T for the same samples as on the *left*.

3.4 The Missing Transverse Momentum

The colliding protons within each successful pp interaction are assumed to be colliding *head on*, with momentum only parallel to the beam-axis. Momentum conservation then implies that the vectorial sum of the transverse momenta of all objects originating from the primary hard-scatter vertex should be exactly zero. The missing transverse momentum, $\mathbf{p}_T^{\text{miss}}$, whose magnitude is denoted by

E_T^{miss} , is calculated each event and its components are defined as the negative vectorial sum of the reconstructed objects associated with the event [83],

$$E_{x(y)}^{\text{miss}} = E_{x(y)}^{\text{miss, electron}} + E_{x(y)}^{\text{miss, photon}} + E_{x(y)}^{\text{miss, } \tau} + E_{x(y)}^{\text{miss, jets}} + E_{x(y)}^{\text{miss, muon}} + E_{x(y)}^{\text{miss, soft}}, \quad (3.7)$$

where each of the $E_{x(y)}^{\text{miss}, i}$ terms ($i \in \{\text{electron, photon, } \tau, \text{jets, muon}\}$) are the negative sum of the momenta in the x - (y -) direction for the respective (calibrateD) objects discussed in previous sections. The $E_{x(y)}^{\text{miss, soft}}$ term is track-based and is reconstructed from the transverse momentum of reconstructed tracks originating from the primary hard-scatter vertex but not associated with any of the hard objects indicated in the other terms appearing in Equation 3.7. The total E_T^{miss} and its direction in azimuth is then given by,

$$E_T^{\text{miss}} = \sqrt{(E_x^{\text{miss}})^2 + (E_y^{\text{miss}})^2}, \quad (3.8)$$

$$\phi^{\text{miss}} = \arctan(E_y^{\text{miss}}/E_x^{\text{miss}}). \quad (3.9)$$

Any imbalance in the visible momenta in a given event will result in nonzero E_T^{miss} . Nonzero values of E_T^{miss} may indicate the presence of weakly interacting particles that do not leave detectable signatures in ATLAS, such as neutrinos from leptonically decaying W bosons in the case of the SM, or may indicate the presence of additionaly weakly interacting particles such as the weakly interacting dark matter candidates that many BSM physics scenarios predict. Precise measurement of the E_T^{miss} , then, is of the utmost importance to many searches for BSM physics. Searches for R -parity conserving Supersymmetry (Section XXX) are commonly characterised by large val- ues of E_T^{miss} due to a multiplicity of stable weakly interacting SUSY particle in the final state. Additionally, detector mismodelling, detecor noise, limited detector coverage, or miscalibration of the reconstructed objects used in the reconstruction of $\mathbf{p}_T^{\text{miss}}$ can also contribute nonzero values to E_T^{miss} . The measurement resolution of the E_T^{miss} is also susceptible to pileup effects, and generally degrades as the levels of pileup increase.

Bibliography

- [1] A. Einstein. “Über einen die Erzeugung und Verwandlung des Lichtes betreffenden heuristischen Gesichtspunkt (On a Heuristic Point of View about the Creation and Conversion of Light)”. In: *Annalen der Physik* 322 (1905), pp. 132–148. DOI: [10.1002/andp.19053220607](https://doi.org/10.1002/andp.19053220607) (cit. on p. 1).
- [2] A. Einstein. “Zur Elektrodynamik bewegter Körper (On the Electrodynamics of Moving Bodies)”. In: *Annalen der Physik* 322 (1905), pp. 891–921. DOI: [10.1002/andp.19053221004](https://doi.org/10.1002/andp.19053221004) (cit. on p. 1).
- [3] A. Einstein. “Ist die Trägheit eines Körpers von seinem Energieinhalt abhängig? (Does the Inertia of a Body Depend Upon Its Energy Content?)” In: *Annalen der Physik* 323 (1905), pp. 639–641. DOI: [10.1002/andp.19053231314](https://doi.org/10.1002/andp.19053231314) (cit. on p. 1).
- [4] M. Planck. “Ueber das Gesetz der Energieverteilung im Normalspectrum (On the law of the distribution of energy in the normal spectrum)”. In: *Annalen der Physik* 309 (1901), pp. 553–563. DOI: [10.1002/andp.19013090310](https://doi.org/10.1002/andp.19013090310) (cit. on p. 1).
- [5] P. A. M. Dirac. “The Quantum Theory of the Electron”. In: *Proceedings of the Royal Society of London Series A* 117 (Feb. 1928), pp. 610–624. DOI: [10.1098/rspa.1928.0023](https://doi.org/10.1098/rspa.1928.0023) (cit. on p. 2).
- [6] Paul A. M. Dirac. “Quantum theory of emission and absorption of radiation”. In: *Proc. Roy. Soc. Lond.* A114 (1927), p. 243. DOI: [10.1098/rspa.1927.0039](https://doi.org/10.1098/rspa.1927.0039) (cit. on p. 2).
- [7] Sigfrido Boffi. “The Rise of Quantum Mechanics”. In: *arXiv e-prints* (2008). arXiv: [0806.4515 \[physics.hist-ph\]](https://arxiv.org/abs/0806.4515) (cit. on p. 2).
- [8] Jagdish Mehra and Helmut Rechenberg. “The Historical Development of Quantum Theory”. In: (2001) (cit. on p. 2).
- [9] S. Tomonaga. “On a Relativistically Invariant Formulation of the Quantum Theory of Wave Fields”. In: *Progress of Theoretical Physics* 1 (Aug. 1946), pp. 27–42. DOI: [10.1143/PTP.1.27](https://doi.org/10.1143/PTP.1.27) (cit. on p. 2).
- [10] R. P. Feynman. “Space-Time Approach to Quantum Electrodynamics”. In: *Physical Review* 76 (Sept. 1949), pp. 769–789. DOI: [10.1103/PhysRev.76.769](https://doi.org/10.1103/PhysRev.76.769) (cit. on p. 2).

- [11] R. P. Feynman. “The Theory of Positrons”. In: *Physical Review* 76 (Sept. 1949), pp. 749–759. DOI: [10.1103/PhysRev.76.749](https://doi.org/10.1103/PhysRev.76.749) (cit. on p. 2).
- [12] R. P. Feynman. “Mathematical Formulation of the Quantum Theory of Electromagnetic Interaction”. In: *Physical Review* 80 (Nov. 1950), pp. 440–457. DOI: [10.1103/PhysRev.80.440](https://doi.org/10.1103/PhysRev.80.440) (cit. on p. 2).
- [13] J. Schwinger. “On Quantum-Electrodynamics and the Magnetic Moment of the Electron”. In: *Physical Review* 73 (Feb. 1948), pp. 416–417. DOI: [10.1103/PhysRev.73.416](https://doi.org/10.1103/PhysRev.73.416) (cit. on p. 2).
- [14] J. Schwinger. “Quantum Electrodynamics. I. A Covariant Formulation”. In: *Physical Review* 74 (Nov. 1948), pp. 1439–1461. DOI: [10.1103/PhysRev.74.1439](https://doi.org/10.1103/PhysRev.74.1439) (cit. on p. 2).
- [15] F. J. Dyson. “The Radiation Theories of Tomonaga, Schwinger, and Feynman”. In: *Physical Review* 75 (Feb. 1949), pp. 486–502. DOI: [10.1103/PhysRev.75.486](https://doi.org/10.1103/PhysRev.75.486) (cit. on p. 2).
- [16] F. J. Dyson. “The S Matrix in Quantum Electrodynamics”. In: *Physical Review* 75 (June 1949), pp. 1736–1755. DOI: [10.1103/PhysRev.75.1736](https://doi.org/10.1103/PhysRev.75.1736) (cit. on p. 2).
- [17] S. S. Schweber. *QED and the men who made it: Dyson, Feynman, Schwinger, and Tomonaga*. 1994 (cit. on p. 2).
- [18] S. L. Glashow. “Partial Symmetries of Weak Interactions”. In: *Nucl. Phys.* 22 (1961), pp. 579–588. DOI: [10.1016/0029-5582\(61\)90469-2](https://doi.org/10.1016/0029-5582(61)90469-2) (cit. on p. 6).
- [19] Steven Weinberg. “A Model of Leptons”. In: *Phys. Rev. Lett.* 19 (1967), pp. 1264–1266. DOI: [10.1103/PhysRevLett.19.1264](https://doi.org/10.1103/PhysRevLett.19.1264) (cit. on p. 6).
- [20] Abdus Salam. “Weak and Electromagnetic Interactions”. In: *Conf. Proc.* C680519 (1968), pp. 367–377 (cit. on p. 6).
- [21] Gerard ’t Hooft. “Renormalization of Massless Yang-Mills Fields”. In: *Nucl. Phys.* B33 (1971), pp. 173–199. DOI: [10.1016/0550-3213\(71\)90395-6](https://doi.org/10.1016/0550-3213(71)90395-6) (cit. on p. 6).
- [22] Gerard ’t Hooft. “Renormalizable Lagrangians for Massive Yang-Mills Fields”. In: *Nucl. Phys.* B35 (1971). [,201(1971)], pp. 167–188. DOI: [10.1016/0550-3213\(71\)90139-8](https://doi.org/10.1016/0550-3213(71)90139-8) (cit. on p. 6).
- [23] F. Englert and R. Brout. “Broken Symmetry and the Mass of Gauge Vector Mesons”. In: *Phys. Rev. Lett.* 13 (1964). [,157(1964)], pp. 321–323. DOI: [10.1103/PhysRevLett.13.321](https://doi.org/10.1103/PhysRevLett.13.321) (cit. on p. 9).
- [24] Peter W. Higgs. “Broken symmetries, massless particles and gauge fields”. In: *Phys. Lett.* 12 (1964), pp. 132–133. DOI: [10.1016/0031-9163\(64\)91136-9](https://doi.org/10.1016/0031-9163(64)91136-9) (cit. on p. 9).
- [25] Peter W. Higgs. “Broken Symmetries and the Masses of Gauge Bosons”. In: *Phys. Rev. Lett.* 13 (1964). [,160(1964)], pp. 508–509. DOI: [10.1103/PhysRevLett.13.508](https://doi.org/10.1103/PhysRevLett.13.508) (cit. on p. 9).
- [26] Jeffrey Goldstone, Abdus Salam, and Steven Weinberg. “Broken Symmetries”. In: *Phys. Rev.* 127 (1962), pp. 965–970. DOI: [10.1103/PhysRev.127.965](https://doi.org/10.1103/PhysRev.127.965) (cit. on p. 10).

- [27] Evgeny Kh. Akhmedov. “Do charged leptons oscillate?” In: *JHEP* 09 (2007), p. 116. DOI: 10.1088/1126-6708/2007/09/116. arXiv: 0706.1216 [hep-ph] (cit. on p. 12).
- [28] Makoto Kobayashi and Toshihide Maskawa. “CP Violation in the Renormalizable Theory of Weak Interaction”. In: *Prog. Theor. Phys.* 49 (1973), pp. 652–657. DOI: 10.1143/PTP.49.652 (cit. on p. 12).
- [29] “CERN Annual Personnel Statistics 2018”. In: (2018). URL: <https://cds.cern.ch/record/2677223> (cit. on p. 14).
- [30] The ALICE Collaboration. “The ALICE experiment at the CERN LHC”. In: *Journal of Instrumentation* 3.08 (Aug. 2008), S08002–S08002. DOI: 10.1088/1748-0221/3/08/s08002. URL: <https://doi.org/10.1088%2F1748-0221%2F3%2F08%2Fs08002> (cit. on p. 14).
- [31] The LHCb Collaboration. “The LHCb Detector at the LHC”. In: *Journal of Instrumentation* 3.08 (Aug. 2008), S08005–S08005. DOI: 10.1088/1748-0221/3/08/s08005. URL: <https://doi.org/10.1088%2F1748-0221%2F3%2F08%2Fs08005> (cit. on p. 14).
- [32] The CMS Collaboration. “The CMS experiment at the CERN LHC”. In: *Journal of Instrumentation* 3.08 (Aug. 2008), S08004–S08004. DOI: 10.1088/1748-0221/3/08/s08004. URL: <https://doi.org/10.1088%2F1748-0221%2F3%2F08%2Fs08004> (cit. on p. 14).
- [33] The ATLAS Collaboration. “The ATLAS Experiment at the CERN Large Hadron Collider”. In: *Journal of Instrumentation* 3.08 (Aug. 2008), S08003–S08003. DOI: 10.1088/1748-0221/3/08/s08003. URL: <https://doi.org/10.1088%2F1748-0221%2F3%2F08%2Fs08003> (cit. on pp. 14, 30).
- [34] Lyndon Evans and Philip Bryant. “LHC Machine”. In: *Journal of Instrumentation* 3.08 (Aug. 2008), S08001–S08001. DOI: 10.1088/1748-0221/3/08/s08001. URL: <https://doi.org/10.1088%2F1748-0221%2F3%2F08%2Fs08001> (cit. on pp. 15, 20).
- [35] *LEP Design Report: Vol. 1: The LEP Injector Chain*. CERN, 1983. URL: <https://cds.cern.ch/record/98881> (cit. on p. 16).
- [36] *LEP Design Report: Vol. 2: The LEP Main Ring*. CERN, 1984. URL: <https://cds.cern.ch/record/102083> (cit. on p. 16).
- [37] Stephen Holmes, Ronald S Moore, and Vladimir Shiltsev. “Overview of the Tevatron collider complex: goals, operations and performance”. In: *Journal of Instrumentation* 6.08 (Aug. 2011), T08001–T08001. DOI: 10.1088/1748-0221/6/08/t08001. URL: <https://doi.org/10.1088%2F1748-0221%2F6%2F08%2Ft08001> (cit. on p. 16).
- [38] Juan Casas et al. “Design concept and first experimental validation of the superfluid helium system for the large hadron collider (LHC) project at CERN”. In: *Cryogenics* 32 (1992), pp. 118–121. DOI: 10.1016/0011-2275(92)90122-Q (cit. on p. 17).
- [39] *ECFA-CERN Workshop on Large Hadron Collider in the LEP tunnel*. CERN. Geneva: CERN, 1984. DOI: 10.5170/CERN-1984-010-V-1. URL: <https://cds.cern.ch/record/154938> (cit. on p. 18).

- [40] Oliver Sim Brüning et al. *LHC Design Report: Vol. 1: The LHC Main Ring*. CERN Yellow Reports: Monographs. Geneva: CERN, 2004. DOI: 10.5170/CERN-2004-003-V-1. URL: <https://cds.cern.ch/record/782076> (cit. on p. 19).
- [41] Oliver Sim Brüning et al. *LHC Design Report: Vol. 2: The LHC Infrastructure and General Services*. CERN Yellow Reports: Monographs. Geneva: CERN, 2004. DOI: 10.5170/CERN-2004-003-V-2. URL: <https://cds.cern.ch/record/815187> (cit. on p. 21).
- [42] Michael Benedikt et al. *LHC Design Report: Vol. 3: The LHC Injector Chain*. CERN Yellow Reports: Monographs. Geneva: CERN, 2004. DOI: 10.5170/CERN-2004-003-V-3. URL: <https://cds.cern.ch/record/823808> (cit. on pp. 19, 23).
- [43] R Scrivens et al. “Overview of the status and developments on primary ion sources at CERN*”. In: CERN-ATS-2011-172 (Sept. 2011), 4 p. URL: <https://cds.cern.ch/record/1382102> (cit. on p. 20).
- [44] Daniel Boussard and Trevor Paul R Linnecar. *The LHC Superconducting RF System*. Tech. rep. LHC-Project-Report-316. CERN-LHC-Project-Report-316. Geneva: CERN, Dec. 1999. URL: <https://cds.cern.ch/record/410377> (cit. on p. 21).
- [45] Werner Herr and B Muratori. “Concept of luminosity”. In: (2006). DOI: 10.5170/CERN-2006-002.361. URL: <https://cds.cern.ch/record/941318> (cit. on p. 23).
- [46] S Haywood et al. “ATLAS inner detector: Technical Design Report, 2”. In: Technical Design Report ATLAS (1997). URL: <http://cds.cern.ch/record/331064> (cit. on p. 27).
- [47] M Capeans et al. *ATLAS Insertable B-Layer Technical Design Report*. Tech. rep. CERN-LHCC-2010-013. ATLAS-TDR-19. Sept. 2010. URL: <https://cds.cern.ch/record/1291633> (cit. on p. 28).
- [48] M. Backhaus. “The upgraded Pixel Detector of the ATLAS Experiment for Run 2 at the Large Hadron Collider”. In: *Nucl. Instrum. Meth.* A831 (2016), pp. 65–70. DOI: 10.1016/j.nima.2016.05.018 (cit. on p. 30).
- [49] *ATLAS liquid-argon calorimeter: Technical Design Report*. Technical Design Report ATLAS. Geneva: CERN, 1996. URL: <https://cds.cern.ch/record/331061> (cit. on p. 31).
- [50] *ATLAS tile calorimeter: Technical Design Report*. Technical Design Report ATLAS. Geneva: CERN, 1996. URL: <https://cds.cern.ch/record/331062> (cit. on p. 31).
- [51] Marija Marjanovic. “ATLAS Tile calorimeter calibration and monitoring systems”. In: *21st IEEE Real Time Conference (RT2018) Williamsburg, Virginia, June 11-15, 2018*. 2018. arXiv: 1806.09156 [physics.ins-det] (cit. on p. 34).
- [52] A Artamonov et al. “The ATLAS Forward Calorimeter”. In: *Journal of Instrumentation* 3.02 (Feb. 2008), P02010–P02010. DOI: 10.1088/1748-0221/3/02/p02010. URL: <https://doi.org/10.1088%2F1748-0221%2F3%2F02%2Fp02010> (cit. on p. 35).
- [53] *ATLAS muon spectrometer: Technical Design Report*. Technical Design Report ATLAS. Geneva: CERN, 1997. URL: <https://cds.cern.ch/record/331068> (cit. on p. 35).

- [54] F. Bauer et al. “Construction and Test of MDT Chambers for the ATLAS Muon Spectrometer”. In: *Nucl. Instrum. Meth.* A461 (2001), pp. 17–20. DOI: 10.1016/S0168-9002(00)01156-6. arXiv: 1604.02000 [physics.ins-det] (cit. on p. 36).
- [55] Theodoros Argyropoulos et al. “Cathode strip chambers in ATLAS: Installation, commissioning and in situ performance”. In: *IEEE Trans. Nucl. Sci.* 56 (2009), pp. 1568–1574. DOI: 10.1109/TNS.2009.2020861 (cit. on p. 36).
- [56] G. Aielli et al. “The RPC first level muon trigger in the barrel of the ATLAS experiment”. In: *Nucl. Phys. Proc. Suppl.* 158 (2006). [,11(2006)], pp. 11–15. DOI: 10.1016/j.nuclphysbps.2006.07.031 (cit. on p. 36).
- [57] S. Majewski et al. “A thin multiwire chamber operating in the high multiplication mode”. In: *Nucl. Instrum. Meth.* 217 (1983), pp. 265–271. DOI: 10.1016/0167-5087(83)90146-1 (cit. on p. 36).
- [58] P Branchini et al. “Global Time Fit for Tracking in an Array of Drift Cells: The Drift Tubes of the ATLAS Experiment”. In: *Nuclear Science, IEEE Transactions on* 55 (Mar. 2008), pp. 620–627. DOI: 10.1109/TNS.2007.914020 (cit. on p. 39).
- [59] Peter Jenni et al. *ATLAS high-level trigger, data-acquisition and controls: Technical Design Report*. Technical Design Report ATLAS. Geneva: CERN, 2003. URL: <https://cds.cern.ch/record/616089> (cit. on pp. 41, 42).
- [60] William Panduro Vazquez and ATLAS Collaboration. *The ATLAS Data Acquisition system in LHC Run 2*. Tech. rep. ATL-DAQ-PROC-2017-007. 3. Geneva: CERN, Feb. 2017. DOI: 10.1088/1742-6596/898/3/032017. URL: <https://cds.cern.ch/record/2244345> (cit. on pp. 41, 42).
- [61] *ATLAS Computing: technical design report*. Technical Design Report ATLAS. Geneva: CERN, 2005. URL: <https://cds.cern.ch/record/837738> (cit. on p. 41).
- [62] C P Bee et al. *The raw event format in the ATLAS Trigger and DAQ*. Tech. rep. ATL-DAQ-98-129. Revised version number 5 submitted on 2016-11-03 11:47. Geneva: CERN, Feb. 2016. URL: <https://cds.cern.ch/record/683741> (cit. on p. 42).
- [63] T Cornelissen et al. “Concepts, Design and Implementation of the ATLAS New Tracking (NEWT)”. In: ATL-SOFT-PUB-2007-007. ATL-COM-SOFT-2007-002 (Mar. 2007). URL: <https://cds.cern.ch/record/1020106> (cit. on p. 44).
- [64] “The Optimization of ATLAS Track Reconstruction in Dense Environments”. In: ATL-PHYS-PUB-2015-006 (Mar. 2015). URL: <https://cds.cern.ch/record/2002609> (cit. on p. 44).
- [65] ATLAS Collaboration. “Reconstruction of primary vertices at the ATLAS experiment in Run 1 proton–proton collisions at the LHC”. In: *Eur. Phys. J.* C77.5 (2017), p. 332. DOI: 10.1140/epjc/s10052-017-4887-5. arXiv: 1611.10235 [physics.ins-det] (cit. on p. 44).

- [66] “Performance of primary vertex reconstruction in proton-proton collisions at $\sqrt{s} = 7$ TeV in the ATLAS experiment”. In: ATLAS-CONF-2010-069 (July 2010). URL: <https://cds.cern.ch/record/1281344> (cit. on p. 44).
- [67] G Piacquadio, K Prokofiev, and A Wildauer. “Primary vertex reconstruction in the ATLAS experiment at LHC”. In: *Journal of Physics: Conference Series* 119.3 (July 2008), p. 032033. DOI: 10.1088/1742-6596/119/3/032033. URL: <https://doi.org/10.1088%2F1742-6596%2F119%2F3%2F032033> (cit. on p. 44).
- [68] ATLAS Collaboration. “Electron and photon performance measurements with the ATLAS detector using the 2015-2017 LHC proton-proton collision data”. In: (2019). arXiv: 1908.00005 [hep-ex] (cit. on pp. 46, 47, 48, 49, 50).
- [69] “Improved electron reconstruction in ATLAS using the Gaussian Sum Filter-based model for bremsstrahlung”. In: ATLAS-CONF-2012-047 (May 2012). URL: <https://cds.cern.ch/record/1449796> (cit. on p. 47).
- [70] Georges Aad et al. “Muon reconstruction performance of the ATLAS detector in proton–proton collision data at $\sqrt{s} = 13$ TeV”. In: *Eur. Phys. J.* C76.5 (2016), p. 292. DOI: 10.1140/epjc/s10052-016-4120-y. arXiv: 1603.05598 [hep-ex] (cit. on pp. 51, 54).
- [71] W. Lampl et al. “Calorimeter clustering algorithms: Description and performance”. In: (2008) (cit. on pp. 55, 56).
- [72] Georges Aad et al. “Topological cell clustering in the ATLAS calorimeters and its performance in LHC Run 1”. In: *Eur. Phys. J.* C77 (2017), p. 490. DOI: 10.1140/epjc/s10052-017-5004-5. arXiv: 1603.02934 [hep-ex] (cit. on p. 55).
- [73] Matteo Cacciari, Gavin P. Salam, and Gregory Soyez. “The anti- k_t jet clustering algorithm”. In: *JHEP* 04 (2008), p. 063. DOI: 10.1088/1126-6708/2008/04/063. arXiv: 0802.1189 [hep-ph] (cit. on pp. 57, 58).
- [74] Matteo Cacciari, Gavin P. Salam, and Gregory Soyez. “The Catchment Area of Jets”. In: *JHEP* 04 (2008), p. 005. DOI: 10.1088/1126-6708/2008/04/005. arXiv: 0802.1188 [hep-ph] (cit. on pp. 58, 59).
- [75] M. Aaboud et al. “Jet energy scale measurements and their systematic uncertainties in proton–proton collisions at $\sqrt{s} = 13$ TeV with the ATLAS detector”. In: *Phys. Rev.* D96.7 (2017), p. 072002. DOI: 10.1103/PhysRevD.96.072002. arXiv: 1703.09665 [hep-ex] (cit. on pp. 58, 60, 63).
- [76] ATLAS Collaboration. “ATLAS b -jet identification performance and efficiency measurement with $t\bar{t}$ events in pp collisions at $\sqrt{s} = 13$ TeV”. In: (2019). arXiv: 1907.05120 [hep-ex] (cit. on pp. 64, 68, 69).
- [77] “Secondary vertex finding for jet flavour identification with the ATLAS detector”. In: ATL-PHYS-PUB-2017-011 (June 2017). URL: <https://cds.cern.ch/record/2270366> (cit. on p. 65).

- [78] “Topological b -hadron decay reconstruction and identification of b -jets with the JetFitter package in the ATLAS experiment at the LHC”. In: ATL-PHYS-PUB-2018-025 (Oct. 2018). URL: <https://cds.cern.ch/record/2645405> (cit. on p. 65).
- [79] R. Frühwirth. “Application of Kalman filtering to track and vertex fitting”. In: *Nucl. Instrum. Meth.* A262 (1987), pp. 444–450. DOI: 10.1016/0168-9002(87)90887-4 (cit. on p. 65).
- [80] “TMVA – Toolkit for Multivariate Data Analysis”. In: (). arXiv: [physics/0703039 \[physics.data-an\]](https://arxiv.org/abs/physics/0703039) (cit. on p. 67).
- [81] “Calibration of the ATLAS b -tagging algorithm in $t\bar{t}$ semi-leptonic events”. In: ATLAS-CONF-2018-045 (Sept. 2018). URL: <https://cds.cern.ch/record/2638455> (cit. on p. 69).
- [82] “Calibration of light-flavour jet b -tagging rates on ATLAS proton-proton collision data at $\sqrt{s} = 13$ TeV”. In: ATLAS-CONF-2018-006 (Apr. 2018). URL: <https://cds.cern.ch/record/2314418> (cit. on p. 69).
- [83] “Expected performance of missing transverse momentum reconstruction for the ATLAS detector at $\sqrt{s} = 13$ TeV”. In: ATL-PHYS-PUB-2015-023 (July 2015). URL: <https://cds.cern.ch/record/2037700> (cit. on p. 70).